Velocity Variations of the Kaskawulsh Glacier, Yukon Territory, 2009-2011

Samantha Darling

Thesis submitted to
the Faculty of Graduate and Postdoctoral Studies
in partial fulfillment of the requirements
for the MSc Degree in Physical Geography

Department of Geography
Faculty of Arts
University of Ottawa

Supervisor:
Dr. Luke Copland (University of Ottawa)

Thesis Committee:
Dr. Laurence Gray (Canada Centre for Remote Sensing)
Dr. André Viau (University of Ottawa)

Abstract

Laser altimetry and satellite gravity surveys indicate that the St Elias Icefields are currently losing mass and are among the largest non-polar sea level contributors in the world. However, a poor understanding of glacier dynamics in the region is a major hurdle in evaluating regional variations in ice motion and the relationship between changing surface conditions and ice flux. This study combines in-situ dGPS measurements and advanced Radarsat-2 (RS-2) processing techniques to determine daily and seasonal ice velocities for the Kaskawulsh Glacier from summer 2009 to summer 2011. Three permanent dGPS stations were installed along the centreline of the glacier in 2009, with an additional permanent station on the South Arm in 2010. The Precise Point Positioning (PPP) method is used to process the dGPS data using high accuracy orbital reconstruction. RS-2 imagery was acquired on a 24-day cycle from January to March 2010, and from October to March 2010-2011 in a combination of ultra-fine and fine beam modes.

Seasonal velocity regimes are readily identifiable in the dGPS results, with distinct variations in both horizontal velocity and vertical motion. The Spring Regime consists of an annual peak in horizontal velocity that corresponds closely with the onset of the melt season and progresses up-glacier, following the onset of melt at each station. The Summer Regime sees variable horizontal velocity and vertical uplift, superimposed on a long-term decline in motion. The Fall Regime sees a gradual slowing at all stations with little variation in horizontal velocity or vertical position. Rapid but short accelerations lasting up to 10 days were seen in the Winter regimes in both 2010 and 2011, occurring at various times throughout each regime. These events initiated at the Upper Station and progress down-glacier at propagation speeds up to 16,380 m day^{-1} and were accompanied by vertical uplift lasting for similar periods. Three velocity maps, one from the winter of 2010 and two from the fall/winter of 2011, produced from speckle tracking were validated by comparison with dGPS velocity, surface flow direction, and bedrock areas of zero motion, with an average velocity error of 2.0% and average difference in orientation of 4.3º.

Acknowledgments

Funding and resources for this project were provided by:

- Natural Sciences and Engineering Research Council Canadian Graduate Scholarship
- Association of Canadian Universities for Northern Studies Garfield Weston Award
- The Yukon Territorial Government's Yukon Grant
- Natural Sciences and Engineering Research Council Northern Research Internship Program
- The Canadian Space Agency's SOAR-E program (project #5015)
- Parks Canada (especially C.Wong and the wardens of the Kluane National Park and Reserve and J. Poitevin for providing Radarsat-2 images)
- CryoEx
- Northern Scientific Training Program
- Polar Continental Shelf Program
- Canada Foundation for Innovation
- Natural Sciences and Engineering Research Council Discovery Grant
- Ontario Research Fund
- Kluane First Nation
- Kluane Lake Research Station

I would also like to thank all of those folks who helped me in the field, who are too numerous to count, as well as the staff of Kluane Helicopters and Trans North Helicopters. I would like to thank B. Danielson for providing the construction plans for the dGPS stations and C. Zdanowicz of the Geological Survey of Canada for providing additional weather data. I would like to thank my friends J. Cao, S. Chow and K. Fong for reminding me to take care of myself, and doing so for me when I forgot, along with J. Tondu and J.Neilson, for being my intercollegiate support system and being there during the hard times. Thanks must also go to S. Thériault at the Department of Geography for all of her support and enthusiasm.

I would like to thank Dr. A. Viau for taking the time to provide insightful criticism and Dr. L. Gray for his patience and brilliance for the duration of the project. I would like to greatly acknowledge and thank W.VanWychen for his mentorship and guidance from the very beginning, and A.White for her patience and kindness through to the end, as well as the other members of the Laboratory for Cryospheric Research for their support throughout.

I would especially like to thank my supervisor Dr. L.Copland for his patience and support, as well as the numerous opportunities he has provided and his willingness to let me return to the Yukon as much as possible.

This project would not have been completed without the constant encouragement, love, and support of my entire family.

Finally, I would like to thank the people of the Klehini Valley, for teaching me to believe in myself, humanity and the future.

Table of Contents

List of Figures

List of Tables

Chapter 1 Introduction

Public and academic attention has been focused on changes in climate patterns over the past several decades, with increasing attention paid to the cryosphere, mainly the Arctic and Antarctic regions, as an indicator of these changes (Lemke, 2007). With over 75% of the Earth's freshwater trapped in the cryosphere and 10% of the Earth's surface covered in permanent ice (Lemke, 2007), the availability of freshwater produced by these sources is directly linked to the climatic evolution of these regions. Changes in precipitation and temperature directly affect the health and stability of glaciers and ice sheets worldwide, with substantial decreases in mass balance seen in many major glaciated regions in the last 40 years (Meier and Dyurgerov, 2002).

A variety of natural features, such as sea ice, permafrost and lake ice have all shown similar responses to changes in both seasonal climate variability and long-term climate conditions. For example, Arctic sea ice has decreased to its lowest levels on record over the past decade, for both extent and thickness, and several Arctic ice shelves have been completely lost (Pope et al., 2012). In 2007, only 55% of the Arctic Ocean was covered by sea ice during the summer and a mean sea ice thickness of 1.89 m was measured in winter 2006-2007, compared to a mean thickness of 3.64 m in winter 1980 (Kwok and Rothrock, 2009). These values represent an accelerating decrease over the last decade, with the summer 2007 extent of 4.28×10^6 km^2 representing an area 23% smaller than the previous low of 5.56×10^6 km^2 in 2005, and 50% of the spatial coverage in the 1950s and 1970s (Stroeve et al., 2008). Studies of lake ice across Canada, based on a dataset of 757 lakes from the Canadian Ice Database, show a tendency towards earlier ice break-up dates at significance levels up to 90% (Duguay, 2006). 72% of lakes in the dataset experience break-ups 10-15 days earlier since 1971, especially in western Canada. Permafrost studies during the International Polar Year expanded the existing network of boreholes to 350 across the north, increasing the ability to monitor the discontinuous permafrost zone. Discontinuous permafrost characteristically has ground temperatures of -3ºC, and so is highly susceptible to changes in climate (Smith et al., 2010). This line of discontinuous permafrost appears to have migrated northward by ~75 km since 1964 and areas that have maintained permafrost are increasingly

unstable, often influenced by local thermal inversions which have increased over the past 50 years (James, 2010).

Sea level rise has been identified as one of the major issues in many climate-related reports, although future projections of both sea level and glacier mass balance changes by agencies such as the IPCC (Lemke, 2007) are now viewed as underestimates due to their failure to properly account for glacier dynamics in their calculations. For example, recent observations in Antarctica and Greenland show a link between short-term climatic changes and variations in ice dynamics, as well as an influence of glacier dynamics on mass balance (e.g. Bartholomew et al., 2010; Joughin et al., 2008; Sundal et al., 2011; Zwally et al., 2002). These observations have forced scientists to take these mechanisms into account in new models. Major ice sheets have seen a shift to negative mass balances, with losses from both Antarctic and Greenland ice sheets nearly doubling in the last decade. This information has been derived from independent measures such as gravity measurements, interferometry, and laser altimetry (Velicogna, 2009; Chen et al., 2009; Rignot et al, 2008a; Pritchard et al, 2009), coincident with a 5% acceleration of sea level rise in the last 7 years (Kerr, 2009). Acceleration and coincident thinning of outlet glaciers have taken on a major role in accounting for the rapidly changing conditions of both the Antarctic and Greenland ice sheets (Pritchard et al., 2009; Rignot et al., 2008a; Rignot et al., 2008b; Velicogna, 2009). With the potential contribution to global sea level from both ice sheets estimated at ~70 m, the impact of changes in melt and ice dynamics on these large ice masses will continue to be felt in the near future (Alley et al., 2005).

Meier et al. (2007) estimated that small glaciers and ice caps account for roughly 60% of present day global ice loss (Figure 1.1 and Figure 1.2). Kaser et al. (2006) estimated glacier contributions to global sea level rise between 1961 and 1990 of up to 0.33 ±0.17 mm a^{-1}, though this number excludes smaller peripheral glaciers of Antarctica and Greenland. The overall melt rate of these glaciers has been generally increasing, with an estimated 0.77 ±0.15 mm a^{-1} contributed between 2001 and 2004 (Kaser et al., 2006). Alaskan glaciers, which cover ~90,000 km^2, have also experienced recent accelerations in their negative mass balance and thinning rates, producing up to an estimated 0.04 mm a^{-1} w.e. of sea level rise, providing

a focus for many studies (Figure 1.3) (Arendt et al., 2002; Arendt et al., 2006; Berthier and Toutin, 2008; Berthier et al., 2010; Dyurgerov and McCabe, 2006; Larsen et al., 2007; Meier and Dyurgerov, 2002; Molnia, 2007; Sauber et al., 2005).

Mass losses from the Antarctic and Greenland ice sheets provide some of the main influences on sea level rise and appear to be primarily controlled by the outlet glaciers that transport interior ice towards the oceans. Particular attention is now being paid to the velocities of these glaciers, as increases in their ice discharge can lead to rapid reductions in their surface elevation (Pritchard et al., 2009). As outlet glaciers melt and accelerate, they draw out increased amounts of ice from the interior (Rignot and Kanagaratnam, 2006; Rignot et al., 2008b; Pritchard et al., 2009; Zwally et al., 2011; Sundal et al., 2011). This process is referred to as dynamic thinning and may also be present in ice fields such as the St Elias Range, which are dominated by similar small outlet glaciers, but have hitherto been little discussed in the literature. Better understanding of where these mechanisms are present is essential to the prediction of overall sea level change.

1.1 Glacier changes in Alaska-Yukon

With an increasing contribution to sea level rise from small, non-polar glaciers and ice caps, regional estimations of loss from these areas are being developed. However, many studies have been forced to focus on small datasets that include only a few representative glaciers of the 90,000 km^2 of ice in Alaska and the Yukon due to accessibility issues (Arendt et al., 2002). For example, Sapiano et al. (1998) re-examined eight glaciers in Alaska and one in Washington State that were first measured in the International Geophysical Year (IGY) (1957-1958) for changes in volume, areal extent and surface elevation. Lemon Creek Glacier, located ~250 km southeast of Kluane National Park and Reserve (KNPR), showed the greatest change with thinning in the ablation zone of up to 100 m between 1957 and 1995 and a 700 m recession of the terminus between 1957 and 1989.

Arendt et al. (2002) used a comparison of laser altimetry studies and topographic maps from the 1950s-1970s of 67 glaciers in Alaska, including the Kaskawulsh and Hubbard Glaciers of the St. Elias Range, to measure changes in thickness and estimate regional volume loss using

volume/area up-scaling techniques. The glaciers of the Chugach and St. Elias Ranges were seen to contribute greatest to the total volume losses of all regions studied, and accounted for nearly 75% of total measured volume change. Nearly all glaciers in the study thinned, which suggests response times to climate variations of about 40 years. However, it seems as though very few glaciers can be considered truly representative of the individual climatic situations, especially in regions that having varying proximities to the coast. The majority of the dataset revealed an average thinning rate of 0.52 m a^{-1} and a total average volume change estimated at -52±15 km^3 a^{-1}, representing nearly 0.14 ±0.04 mm a^{-1} of sea level rise in the past 50 years. Additional work focused on the western Chugach Mountains to confirm results from the use of laser altimetry, volume/area up-scaling and region-wide extrapolations (Arendt et al. 2006). In this later study the regional dataset was expanded to 23 glaciers, both inland and coastal. Estimates of average net balance rates for non-tidewater glaciers in the region were between -1.5 and -0.02 m a^{-1}, with individual glaciers showing a variety of responses to sub-regional climatic variations.

Larsen et al. (2007) used differences between digital elevation models (DEM) collected by the Shuttle Radar Topography Mission (SRTM) in 2000 and DEMs derived from stereo air photo composites from 1948-1987 to determine glacier volume changes in SE Alaska and north-west BC (including the Stikine and Juneau Icefields to the south of KNPR). A rate of volume loss of 16.7 ±4.4 km^3 a^{-1} and an overall thinning were observed, with this region contributing 0.04 ±0.01 mm a^{-1} to global sea level rise since 1948, a slightly smaller estimate than that of Arendt et al. (2002). Surface elevations lowered over 95% of the glaciated area, with a vertical lowering of up to 640 m on the lower Muir Glacier, again since 1948. While the most substantial changes in elevation occurred during the last half of the 20^{th} century, some thickening was observed, especially on the Taku Glacier, Alaska. Hence, while a regional thinning trend is observed, some anomalies remain.

Barrand and Sharp (2010) completed an inventory of 1396 Yukon glaciers, including the Canadian portion of the St Elias Range and the Mackenzie Range, and delineated their boundaries based on satellite imagery. These glaciers were then compared to a set of 802 glaciers digitized from air photos collected during the first International Geophysical Year

(1957-58) and later satellite imagery from the International Polar Year (2007-09) to determine area loss over the 50-year period. A 22% loss of total ice-covered area was seen, regardless of initial glacier size. Using the measured glacier area, volume/area up-scaling methods were used to calculate thickness and volume changes for all glaciers observed. An area-averaged thinning rate of 0.78 ±0.34 m a^{-1} was found for the entire dataset over the study period. Calculated volume losses were 8.12 ±3.5 Gt a^{-1}, which translates into a total contribution of 1.12 ±0.49 mm to global sea level rise over 50 years, or 0.02 ±0.009 mm a^{-1}.

Berthier et al (2010) examined regional changes in Alaskan glaciers, which included the St Elias Range, using differences in sequential DEMs produced from 1968 contour maps and 2006 SPOT5 and ASTER satellite imagery. The St. Elias and Wrangell Mountains region was found to have ice losses of 21.66 ±4.4 km^3 a^{-1} w.e. and an area average mass balance of -0.47 ±0.09 m a^{-1} w.e. Overall, general thinning at lower elevations and sporadic thickening at higher elevations were identified, with ice losses of 41.9 ±8.6 km^3 a^{-1} w.e. and an area average mass balance of -0.48 ±0.10 m a^{-1} w.e. over the 38 year study period. These figures indicate a contribution to sea level rise of 0.12 ± 0.02 mm a^{-1} for the entire dataset, or 7.5% of recent estimates of total sea level rise.

There is a large discrepancy amongst recent estimates for the glaciers of Alaska and Yukon for sea level contribution, ranging between 0.02 ±0.009 mm a^{-1} and 0.14 ±0.04 mm a^{-1}, and rate of glacier thickness change, ranging between -0.52 m a^{-1} and 0.78 m a^{-1} (Arendt et al., 2002; Barrand and Sharp, 2010; Larsen et al., 2007). In general, however, the above authors agree on the regional trend towards thinning at increasing rates and general volume losses. The role of dynamic thinning and ice discharge has remained largely un-addressed to date, but may aid in refining these estimates and future predictions. The St Elias Range is often represented in these region-wide studies by a select few glaciers, one of which is the Kaskawulsh Glacier.

1.2 Study objectives

From the above review it is clear that small non-polar glaciers attached to larger icefields, such as those found in Alaska, are emerging as vital contributors to sea level rise, and the St

Elias Icefield in particular is a front-runner in these contributions. However, the effects of meltwater availability on the dynamics of land-terminating glaciers in this region are poorly understood. The main research question for this study is therefore: What are the inter-annual variations in velocity of the Kaskawulsh Glacier, and what are the potential causes of these fluctuations? To this end, this study has two main objectives:

1) To establish the spatial, seasonal, and inter-annual variations of the surface velocity along the Kaskawulsh Glacier on a daily timescale using differential GPS techniques, and assess the causes of notable events using meteorological measurements (e.g. air temperature);

2) To establish monthly patterns of winter surface velocity, both longitudinally and laterally, over the Kaskawulsh Glacier and its tributaries using speckle-tracking methods. These measurements will be validated using the dGPS results from Objective 1, in preparation for future regional velocity studies.

1.3 Thesis structure

This thesis is presented in the traditional format, in four main parts:

Chapter 2 Background outlines past research in the areas of ice dynamics and the St Elias Range, with a particular focus on work completed on and near the Kaskawulsh Glacier and its historical and regional significance.

Chapter 3 Methods presents a detailed description of the methods and techniques employed for this study.

Chapter 4 Results describes the results of the study, including an evaluation of errors.

Chapter 5 Discussion and Conclusions presents an in-depth discussion of the results presented in relation to one another and conclusions that may be drawn from this evidence.

Figure 1.1 Graph illustrating the relative contributions made by small glaciers and ice caps, and the large ice sheets, to sea level between 1995 and 2005. Glaciers and ice caps were estimated to contribute ~60% over this period, compared to a total of ~40% from the Greenland and Antarctic Ice Sheets (Meier et al., 2007)

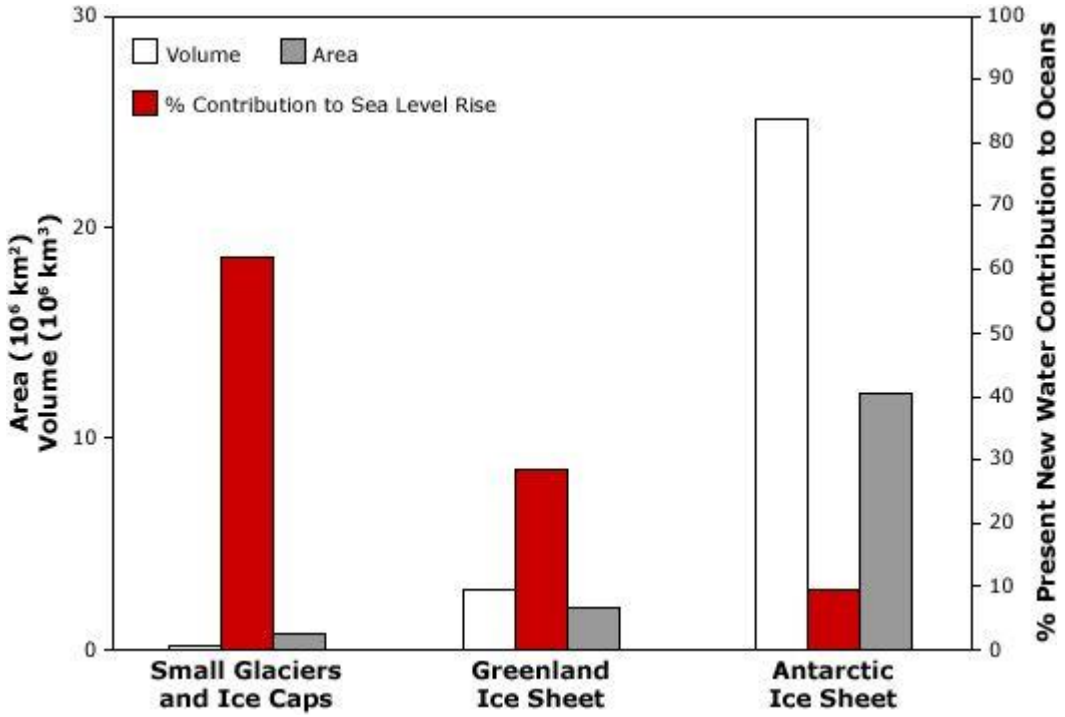

Figure 1.2 Estimated contribution to global mean sea level budget from various sources (upper four entries), showing that the glaciers and ice caps of the world contribute more to global sea level rise in recent years than Greenland Ice Sheet and Antarctic Ice Sheet from 1961 to 2003 (blue) and 1993 to 2003 (brown) (Lemke et al., 2007)

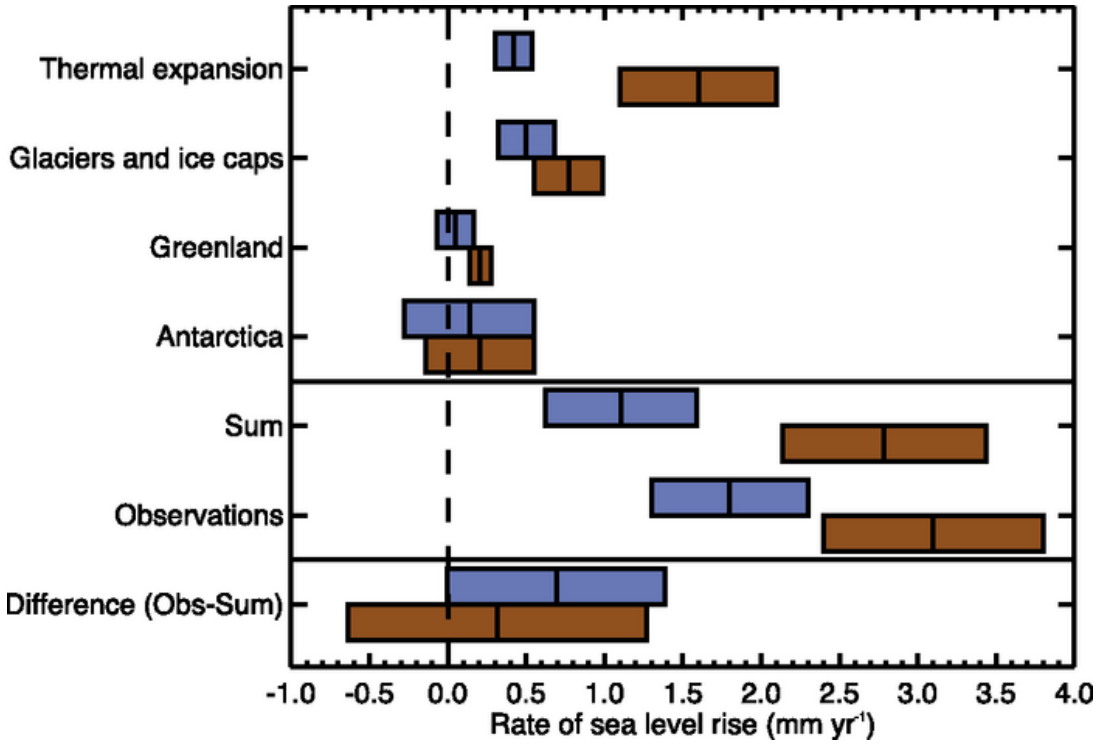

Figure 1.3 Cumulative total mass balance of glaciers and ice caps between 1960 and 2004 for various locations around the world (Dyurgerov and Meier, 2005).

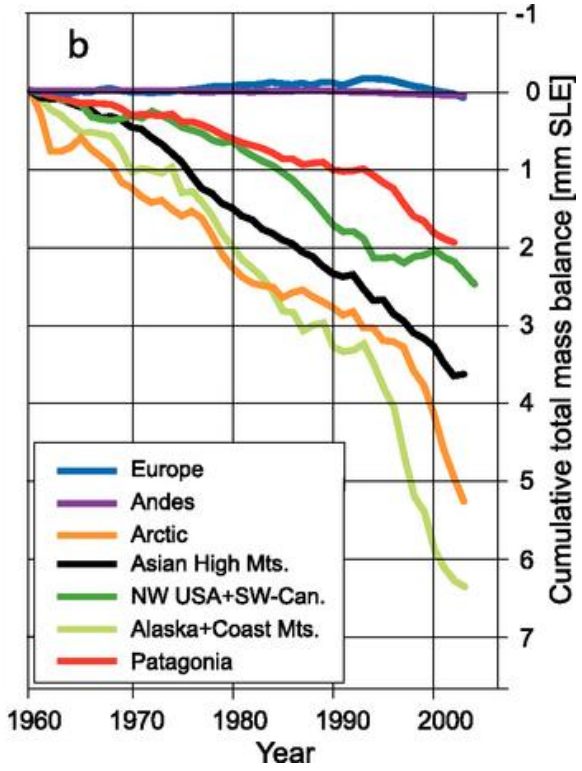

Figure 1.4 Map of the Kaskawulsh Glacier and study area in national context and in relation to other representative glaciers used in Arendt et al (2002) and other regional studies.

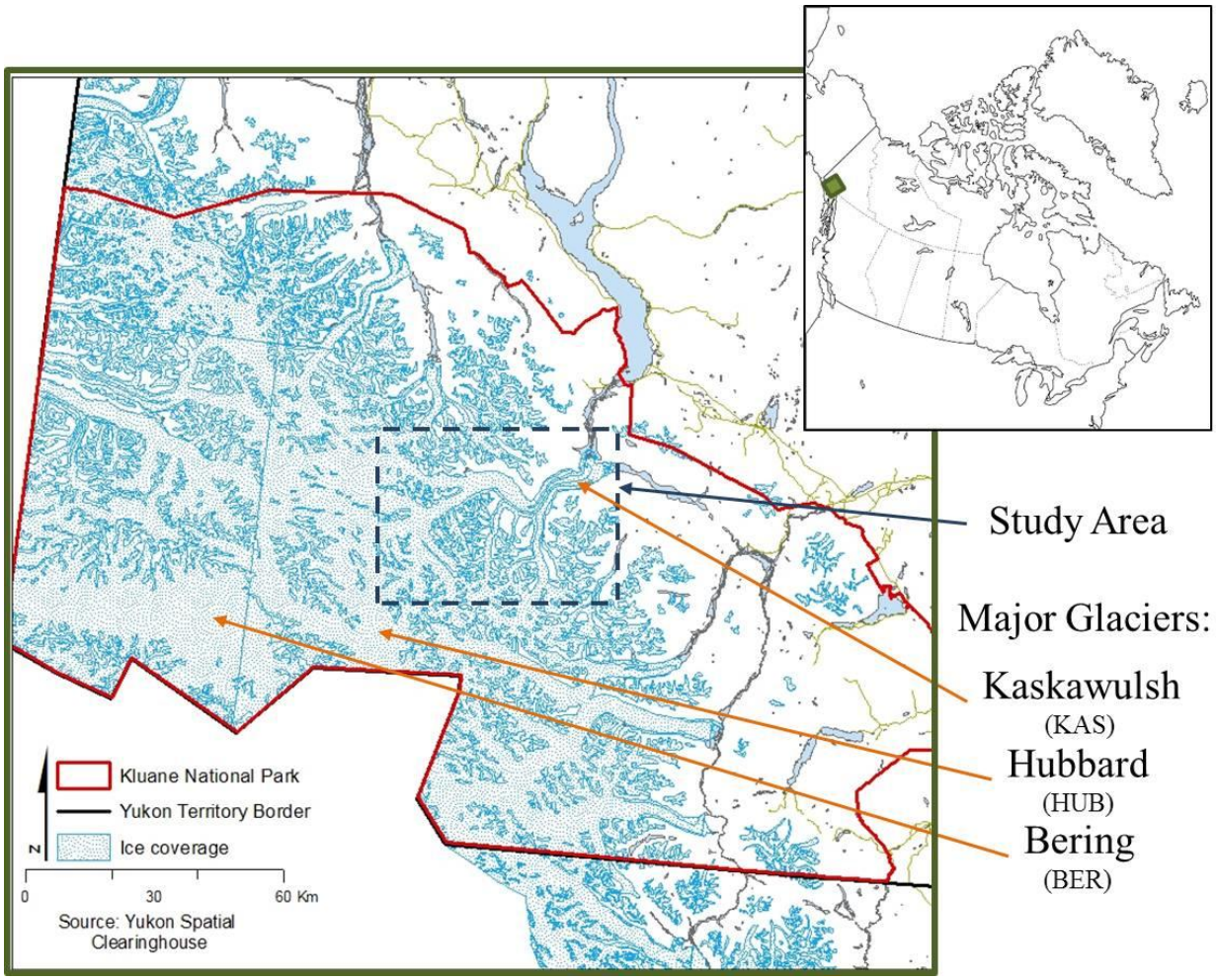

Chapter 2 Background

To place the current study in context, there are three fundamental glaciological concepts which need to be described: 1) the general processes by which glaciers move, 2) surface and subglacial hydrology, and 3) basal and surface glacier motion specifically. This section outlines these concepts in detail, puts the current study area into a regional geographic context, and then provides an overview of past work completed on and around the Kaskawulsh Glacier and the role of the glacier in the development of regional drainage systems.

2.1 Glacier motion and glacier thermal regimes

In general, glacier motion can be attributed to varying combinations of three different processes: *ice deformation, bed deformation,* and *basal sliding* (Figure 2.1). *Ice deformation* occurs in the fabric of the ice, mainly through *ice creep*, as individual ice crystals interact with one another as they are compressed and move downhill due to the force of gravity. This process depends primarily on ice thickness as the main control. *Bed deformation* occurs when a glacier is underlain by poorly consolidated sediments, which can be weakened and transported by the presence of water. *Basal sliding* occurs at the contact between ice and the bed, and is largely controlled by friction. The amount of friction is primarily determined by the bed type (e.g., bedrock or sediment) and the presence of water, which acts as a lubricant.

The internal and basal thermal structure of a glacier typically plays a dominant role in the type and rate of motion that it undergoes, particularly in relation to the properties of the ice at the bed. Glaciers have been traditionally split into three major thermal categories, as outlined by Benn and Evans (1998):

a) *Cold glaciers* contain ice that remains well below the pressure melting point (PMP) throughout their thickness, and generally occur as thin ice masses in areas of low snow accumulation and where heat sources (e.g., from surface meltwater) are limited. Their cold temperatures and lack of insulation (thinner ice means less insulation from cold atmospheric temperatures) mean that they are generally frozen to their bed and ice motion is limited to slow rates of internal *ice deformation* alone. This type of

glacier is typically found in very cold parts of the Antarctic and Arctic, as well as at very high altitudes.

b) A glacier is considered *temperate* when all ice is at the PMP, and the effects of cold winters are offset by a thick insulating snow pack. Latent heat release from the refreezing of meltwater acts to raise snow pack temperatures to 0°C in the accumulation zone during the summer, and cold surface ice in the ablation zone is completely removed during the summer melt season. Ice motion in temperate glaciers is dominated by *sliding* and *bed deformation* in varying degrees, due to the presence of water at the glacier bed throughout the year. Basal water pressure and basal drainage conditions (discussed in more detail in section 2.3) determine the rate of basal motion via the regulation of friction at the bed. *Temperate glaciers* are generally found in relatively warm climates in areas of relatively high snow accumulation and high melt rates, such as the coastal ranges of North and South America and western Norway. These conditions effectively describe those found for large glaciers in the St. Elias Icefields, such as the Kaskawulsh Glacier.

c) *Polythermal glaciers* contain a mixture of warm and cold ice in various combinations. Areas of the ice-bed interface can be frozen, much like in a *cold glacier*, where cold ice is well below the PMP and *ice deformation* dominates. On the same glacier, other areas can act much like a *temperate glacier*, with warm ice at the PMP at the ice-bed contact, allowing for *sliding* and *bed deformation* processes to dominate. Ice motion for this type of thermal regime therefore depends on the proportion and placement of the subglacial areas frozen to the bed (Fischer et al., 1999). Polythermal glaciers are often found in polar maritime climates, including Storglaciären in Sweden, Trapridge Glacier in the Yukon and on Ellesmere Island, as well as the center of the Antarctic Ice Sheet, where thick ice provides sufficient insulation to produce a warm bed.

2.2 Glacier hydrology

Glacier motion in temperate glaciers, such as the Kaskawulsh Glacier, is strongly controlled by the production of meltwater at the glacier surface and subglacial hydrology. Much work has been completed on this relationship in polythermal glaciers, such as John Evans Glacier, Ellesmere Island, and some temperate glaciers, such as Haut d'Arolla Glacier, Switzerland (e.g. Bingham, et al. 2003; Bingham et al., 2005; Bingham et al., 2006; Copland et al., 2003b; Copland et al., 2003c; Nienow et al., 1998).

2.2.1 Surface meltwater migration

All types of glaciers share the main mechanisms controlling the transportation of meltwater through supra- and englacial drainage, summarized by Fountain and Walder (1998). In firn- and snow-covered regions (i.e., mainly the accumulation area), transport of surface meltwater is dominated by slow percolation, via small crevasses and intergranular flow. Firn essentially dampens out diurnal variations in runoff, delays the onset of spring runoff, and extends the runoff season by storing water near the glacier surface. Water is stored in the inter-granular spaces between ice crystals as firn is compressed into glacier ice, in volumes up to 44% of the total seasonally stored water volume. In regions where ice is exposed (i.e. the ablation area), the rapid movement of surface meltwater occurs via runoff through supraglacial streams, moulins and englacial conduits (Figure 2.2). Stenborg (1973) observed these processes in Mikkaglaciären and Storglaciären, Sweden, citing two mechanisms by which surface drainage can connect to internal systems: 1) connections through relic or pre-existing vents (e.g., shallow crevasses, moulins), and 2) connections created by the presence of standing water. Alley et al. (2005) were able to identify similar conditions on the cold ice of the GrIS, where modeling suggests that water-filled fractures can extend to the bed, even in thick ice (>1 km), and later collapse to form moulins. Surface lakes and areas of supraglacial water accumulation were also identified as prime areas for the development of moulins. In temperate and polythermal glaciers the movement of meltwater towards the glacier bed through these supraglacial and englacial drainage systems becomes important for ice motion, as they provide means for meltwater to travel to the bed and influence subglacial hydrology.

2.2.2 Subglacial hydrology

Surface meltwater is mostly produced by changes in positive air temperature, and tends to pool on the glacier surface in crevasses and low-lying areas to form supraglacial lakes (Stenborg, 1973; Fountain and Walder, 1998). Migration of this meltwater to a temperate bed through the features outlined above can happen over hours, days or weeks (Hock and Hooke, 1993; Nienow et al., 1998; Mair et al. 2003; Lappegard and Kohler, 2006), after which it can either be stored or drained depending on the stage of development of the subglacial drainage system. Benn and Evans (1998) summarize two types of subglacial drainage systems:

1) *Distributed (inefficient)* systems are categorized into water films, linked cavity networks, braided canal networks, and groundwater flow. These systems remain at the interface between the glacier bed and temperate ice, and are generally believed to be inefficient at transporting water.

2) *Channelized or arborescent (efficient)* systems are typically incised either upwards into the basal ice (Röthlisberger channels), down into a hard bed (Nye channels) or deeper down into a sediment bed (tunnel valleys). These systems are highly efficient in the transportation of surface meltwater through a branched channel network.

A seasonal progression between these drainage systems is well documented on various temperate glaciers (e.g. Hock and Hooke, 1993; Nienow et al. 1998; Mair et al. 2002; Lappegard and Kohler 2006). For example, Hock and Hooke (1993) used 10 fluorescein and rhodamine dye-tracing experiments in July and August 1989 to examine the development of drainage systems on Storglaciären in Sweden. Nienow et al. (1998) used similar rhodamine dye tracing techniques in the summers of 1990 and 1991 on the Haut Glacier d'Arolla, a temperate glacier in Switzerland. In these experiments, a known quantity of rhodamine dye was introduced into the internal drainage system of the glacier through a series of moulins, and then measured at the primary outlet stream at the front of the glacier (Figure 2.3). Five parameters of the resulting dye-return curves (dye concentration vs. time) were then used to understand variations in the structure of the subglacial drainage system through the melt season:

1) time between initial injection into the moulin and peak dye concentration at the outlet (Hock and Hooke, 1993; Nienow et al., 1998)

2) minimum estimated mean flow velocity (Hock and Hooke, 1993; Nienow et al., 1998)

3) rate of dispersion during travel (Hock and Hooke, 1993; Nienow et al., 1998)

4) rate of dispersion relative to the rate of advection of the dye cloud (Nienow et al., 1998)

5) apparent mean cross-sectional area (Nienow et al., 1998).

A distributed (inefficient) subglacial drainage system will produce a dye return curve that gradually increases in concentration, peaking well below the actual concentration injected, followed by a gradual decline lasting multiple hours. In contrast, a channelized (efficient) system will produce a curve that peaks a relatively short time after injection, with the period of high concentration lasting for a very short time. In the case of highly braided channelized systems, such as those observed by Hock and Hooke (1993), multiple peaks in concentration are possible. The transition from one system to the other is visible when dye-return curves from multiple experiments are plotted together, paying particular attention to the dates of the experiments in relation to typical seasonal melt conditions. Nienow et al. (1998) clearly show a temporal progression in the characteristics of recorded dye return curves, with dates earlier in the melt season exhibiting distributed behavior and those later on exhibiting channelized characteristics. Nienow et al. (1998) also observed that the melt season migration of the snowline up-glacier appeared to drive the switch from distributed to channelized subglacial drainage systems.

2.3 Basal glacier motion

Basal motion can be due to *bed deformation* or *sliding*, as described in Section 2.1, both of which are dependent on the presence of water at the bed. *Sliding*, in particular, requires the presence of water, however minimal, for the reduction of friction. Basal sliding theories arose from a need to account for the amount of surface velocity that could be attributed to the movement of a glacier over its bed, as opposed to that due to internal deformation. Weertman

(1954) initially focused on two theoretical processes: *regelation* and *enhanced creep*. *Regelation* is when basal ice meets an obstacle and the ice in contact with the obstacle is brought up to the pressure melting point, producing meltwater that flows downglacier of the obstacle and refreezes. The freezing process releases latent heat, which is transferred through the obstacle, aiding the melting process on the upglacier side of it (Figure 2.4). *Enhanced creep* involves the increase of stress concentration upglacier of large obstacles, which allows enhanced ice deformation rates and allows ice to move rapidly past the obstacle. In short, Weertman's simple theory is based on regelation and creep processes and fails to account for basal cavitation and fracture or the presence of water at the bed (Fowler, 2010). Lliboutry (1959) identified this weakness and proposed an alternative that included strong cavitation at the bed and basal water. Further work supports the presence of water at the bed and later the role of water pressure and then effective pressure in basal sliding (Paterson, 1994; Benn and Evans, 1998). This led to the general acceptance of an empirically based basal sliding "law":

$$U_b = k_s \tau_d^p N^{-q} \qquad (\mathbf{1})$$

where U_b is basal velocity, τ_d is driving stress, N is effective pressure, and k_s, p, and q are constants that are derived empirically. The driving stress term τ_d is defined in Equation 2 by the combination of ice thickness H, ice density r_i, and ice surface slope a:

$$\tau_d = \rho_i g H \tan\alpha \qquad (\mathbf{2})$$

Surface slope and ice thickness, therefore, affect the sliding law in different ways, so that thinner ice is more influenced by the bed slope. The focus of the current work is on the term N, which deals with effective pressure.

Effective pressure (N) is defined as the difference between normal pressure at the bed (P_i; also referred to as ice overburden pressure) and water pressure at the bed (P_w) (Benn and Evans, 1998):

$$N = P_i - P_w \quad \textbf{(3)}$$

where $P_i = \rho_i g (h_i - z)$ in which ρ_i the density of ice, g is gravity, h_i is the height above the base and z is the total ice thickness, which approximates the weight of overlying ice. As seen in Equation 1, effective pressure is inversely proportional to basal velocity (U_b) since high basal water pressures reduce basal friction and can effectively float a glacier off its bed. Paterson (1994) outlines how variations in basal water pressure interact with the ice overburden pressure, where P_s is the point at which the basal ice decouples from the bed or "separation pressure" and P_c is a demonstrated critical threshold between P_s and P_i:

1) $P_w < P_s$ results in a constant sliding velocity, indicating the dominance of regelation and ice deformation;
2) $P_w = P_s$ results in the presence of water-filled cavities and increased sliding;
3) $P_w = P_c$ results in increased, unstable sliding.

Subglacial water pressure is therefore an important variable when discussing variations in both basal and surface motion. The generalization of Equation 1 allows for variation in bed slope, bed roughness, ice thickness and water pressure, which leads to the conclusion that water pressure, not water volume, is the dominant control on basal sliding, at least on a short-term basis (Paterson, 1994; Benn and Evans, 1998). Surface motion can be used to infer conditions at the bed, as increased horizontal motion and vertical uplift typically indicate high basal water pressures (e.g., Iken and Truffer, 1997; Harper et al., 1998; Clarke, 2005).

After measuring periods of high horizontal motion with peak periods of vertical uplift on Unteraargletscher, Switzerland during the summer of 1975, Iken et al. (1983) postulated that the storage of water under the glacier and changes in subglacial water pressure, not water volume, were responsible for these velocity changes. On the Findelengletscher in Switzerland, Iken and Truffer (1997) more closely observed changes in vertical and horizontal velocities that corresponded well with changes in borehole water pressure and led to speculation around a process called *hydraulic jacking*. The term *hydraulic jacking* refers to the temporal increase in basal water pressure within a cavity system when the volume of

water entering the system surpasses the capacity for the system to drain efficiently, which results in a noticeable vertical uplift. This mechanism was inferred for early melt season conditions by Iken and Truffer (1997), while the spatial distribution and connectivity of subglacial cavities were seen to play a larger role later in the melt season. High water pressure would initially encourage increased connectivity, and then subside as major channels develop and water pressure decreases.

Harbor et al. (1997) examined boreholes in a cross-section of the Haut Glacier d'Arolla in Switzerland, and found that the dominant motion processes varied across the glacier. For example, the margins were found to experience more basal motion through changes in water pressure than the centerline, where ice deformation was dominant. Harper et al. (1998) measured the three dimensional deformation of the Worthington Glacier in Alaska, and theorized that basal sliding accounts for 60 to 70% of all surface motion, with decreased resistance at the bed with the presence of water, resulting in increasing sliding and increased total surface motion. Boulton et al. (2001) identified the basal hydraulic regime and changes in water pressure therein on Breiðamerkurjökull in Iceland as a control on basal till deformation and therefore ice motion, and agreed that this process was most prominent at the glacier margins. Clarke (2005) identified a generalized diurnal and seasonal cycle of water pressure at the bed where the influence of basal friction and the cohesiveness of subglacial sediment decreased with increased water pressure, resulting in increased surface velocities. He further described velocity events caused by sudden changes in basal water volume and pressure, which are manifested and referred to by others as 'speedups', 'spring events' or 'high velocity events' (e.g. Copland et al., 2003a; Bingham et al., 2006)

From the above review, it is clear that short-lived changes in water pressure have been documented on both temperate and polythermal glaciers. Mair et al. (2003) measured surface motion, basal motion, and subglacial hydrology, especially subglacial water pressure, on Haut Glacier d'Arolla in the ablation seasons of 1998 and 1999. These observations identified how spring meltwater inputs to a distributed subglacial drainage system provided some mechanisms for brief speed up events lasting between 3 and 10 days, through an increase in basal hydraulic pressure (i.e., decrease in effective pressure), and the decoupling

of the ice from the bed. Three “spring events” were identified with similar characteristics of increased surface motion, high subglacial water pressures, and increased outlet stream discharge driven by high melt rates. Surface velocities in particular rose to between two and ten times background velocities for up to ten days during the longest event. Once the subglacial drainage system adjusted to the water volume, velocities returned to a relatively stable summer regime.

Similar speed up events coinciding with increased water volume have been observed by Boon et al. (2003) and Bingham et al. (2006) on John Evans Glacier, a polythermal glacier in the Canadian High Arctic, and Anderson et al. (2004) on the Bench Glacier, a temperate glacier in Alaska. Boon et al. (2003) detected an extreme melt event by monitoring supraglacial lakes and streams on the glacier surface, until they drained through the development of moulins within days of a warm weather event in mid-July that caused enhanced surface melt rates. Bingham et al. (2006) tied these extreme melt events to periods of increased velocity. Peak melt did not affect the development of the subglacial drainage system, which is generally established by the beginning of July through the connection of supraglacial runoff systems and the bed, and then the subglacial drainage system. This led to the speculation that early season events may have greater impact on subglacial water pressures, as the subglacial drainage system at that time would be under-developed, and surface snowpack would play a greater role in meltwater storage by increasing the lag between meltwater production and meltwater entering the englacial drainage system. Late season events would serve to enlarge existing subglacial drainage systems, but may not overwhelm them. Anderson et al. (2004) used dGPS measurements on the Bench Glacier in Alaska to document two such “spring” events in a temperate setting, each lasting around one week and separated by a period of slower sliding. This documentation was then used to create a conceptual model of the events, which coincides well with general theories about sliding. The progression of the first event was attributed to changes in basal effective pressure and the complex development of a subglacial cavity or arborescent drainage network. Changes in vertical displacement during the end of the second event were indicative of the establishment of an efficient subglacial drainage system. The transition from a

distributed subglacial drainage system to a channelized one causes a drop in basal water pressure, which, in turn, decreases horizontal velocity.

The Greenland Ice Sheet (GrIS) has seen overall increases in mass losses due to melt and dynamic thinning of outlet glaciers over the past decade or two (Thomas et al., 2006; Pritchard et al., 2009; Velicogna, 2009; Rignot and Kanagaratnam, 2006). Mass balance estimates for the Greenland Ice Sheet for the late 20th century range from 4 Gt a^{-1} in the early 1990s (Thomas et al., 2006) to 97±47 Gt a^{-1} in 1996 (Rignot et al., 2008b), while Zwally et al. (2011) estimated 7±3 Gt a^{-1} for 1992-2002. The early 21st century saw increases in the ranges of mass loss, with estimates of 137 Gt a^{-1} in 2003 and 286 Gt a^{-1} in 2007-2009 (Velicogna, 2009) and 171±4 Gt a^{-1} for 2003-2007 (Zwally et al., 2011). This corroborates a mass loss estimate by Rignot et al. (2008b) of 267±38 Gt a^{-1} in 2007.

Retreat of glaciers in many areas of the southeast coast of Greenland was seen to peak in 2003, with some outlet glaciers doubling their mass losses in 2004. After a period of slower retreat, these glaciers have more recently started to retreat further and at an increasing rate (Howat et al., 2007; Howat et al., 2008). This pattern of acceleration and thinning has since migrated northward, so that the majority of GrIS outlets are now experiencing negative surface mass balance, which appears to be dominated by ice discharge. This especially affects low elevations, specifically areas below 2000 m (Luthcke et al., 2006).

Changes in ice discharge and the related dynamic thinning of outlet glaciers has been the dominant control on mass budget for the GrIS (Rignot and Kanagaratnam, 2006; Rignot et al., 2008b; Pritchard et al., 2009). Rignot and Kanagaratnam (2006) reported glacier accelerations in the southern regions of Greenland between 1996 and 2000, followed by similar accelerations to the north of 70ºN by 2005. This led to the doubling of the mass deficit for the GrIS over a 9 year period. This coincides with recent increases in surface melt, such as the fact that 2007 melt extent was 60% larger than in 1998. The changes in melt patterns have been identified through various satellite sensors such as the Electrically Scanning Microwave Radiometer, Scanning Multichannel Microwave Radiometer and the Special Sensor Microwave/Imager (Mote, 2007; Rignot et al., 2008a; Chen et al., 2009;

Velicogna, 2009). Some southern regions experienced as much as 50 more melt days than average in 2007, with the onset of melt up to 30 days earlier than average (Mote, 2007). Increases in surface melt rates at low elevations accentuate the process of dynamic thinning, corresponding to short dramatic increases in velocity due to the production of meltwater (Zwally et al, 2002; Van de Wal et al., 2008). This encourages the further transport of ice to lower elevations via basal lubrication (Rignot et al., 2008b). Pritchard et al. (2009) observed faster glaciers with increased thinning rates in both Antarctica and Greenland, and speculated that ice sheet changes are directly dependent on the dynamics of outlet glaciers.

While seasonal and long-term variations in the velocity of outlet glaciers have been well documented, recent studies also indicate that short-term summer accelerations occur (Rignot et al., 2008b; Howat et al., 2008). In particular, glaciers on the western coast of the GrIS seem to demonstrate this behaviour, with two main hypotheses for their cause: changes in calving front activity and changes in surface meltwater availability. Since this study focuses on a land-terminating glacier, the review here will focus on the role of surface meltwater availability, since calving fronts are only characteristic of marine-terminating glaciers.

Sundal et al. (2011) propose a slightly contrary relationship between melt and surface velocity for land terminating glaciers on the GrIS. Observation of six land-terminating glaciers in the southwestern part of the GrIS showed that years with higher melt rates produced more meltwater, lubricating the bed as described above, and producing peak velocities 50%-100% of respective background (winter) velocities. At the time of this peak, a critical monthly surface run-off rate of 1.4 cm day^{-1} of water is reached, producing a more efficient system of subglacial channels (Sundal et al., 2011). Once this system is in place, basal water pressure drops, and the glacier slows to background levels. Theoretical work by Schoof (2010) argues that increases in mean meltwater volume entering a subglacial drainage system would lead to deceleration of surface velocities through the switch from a linked-cavity drainage system (which is inefficient and produces high basal water pressure with only slight increases in water input) to a channelized system (which is highly efficient and stable). These concepts were addressed in depth in Section 2.2. Schoof (2010) also theorized that occasional spikes in water volume would increase basal water pressure for short periods.

Zwally et al. (2002) correlated periods of high melt in the ablation area of outlet glaciers of the GrIS during the summers of 1996-1999 with increases in horizontal velocity. Increased basal water pressure and a decoupling of the glacier from its bed were driven by the drainage of meltwater to the bed through networks of moulins and crevasses. In particular, periods of intense summer melt matched well with accelerations in surface ice velocity for up to a month (Van de Wal et al., 2008). These studies point towards a coupling between surface melt and ice motion, where increased meltwater available to the base of a glacier increases lubrication and therefore motion. Velocity has been measured at up to 4 times background values within days of increased melt (Van de Wal et al., 2008), and, throughout a summer, increases up to 220% above winter values (Bartholomew et al., 2010). On longer time-scales, however, it appears that subglacial drainage adjusts to variations in meltwater input, so that these accelerations only occur when subglacial drainage systems are inefficient and under-developed and are quickly overwhelmed by the increases in meltwater volume, causing higher water pressures (Van de Wal et al., 2008). With recent increases in surface melt across the majority of the GrIS (Mote, 2007), the water available for migration to the ice bed is also likely increasing over time.

A collection of studies completed in the Canadian High Arctic on John Evans Glacier (JEG), a polythermal glacier with temperate basal ice present at the lower ablation zone, has revealed similar velocity responses to meltwater production (Bingham et al., 2003; Bingham et al, 2005; Bingham et al., 2006; Boon et al., 2003; Copland and Sharp, 2001; Copland et al., 2003a; Copland et al., 2003b; Copland et al., 2003c). Short term (typically 2-4 day) high velocity events occurring in June 2000 and 2001 were identified and examined using theodolite, rhodamine dye injection and residual vertical motion techniques. These events were seen to correspond well with periods of high melt and the rhodamine dye injection study documented the progression between inefficient and efficient drainage system during the summer melt season, a process that was clearly outlined in Section 2.2 (Bingham et al., 2003; Boon et al., 2003).

2.4 Study area

The St. Elias Range is located on the border between southwest Yukon and Alaska (Figure 1.4), and experiences coastal climate conditions to the south and a semiarid continental climate to the northeast (Marcus, 1974). About 22,060 km^2 of the mountain range is located in Kluane National Park and Reserve (KNPR), harbouring 12,056 km^2 of ice (Yukon Territorial Government, 1997). This ice takes the form of medium and large land- and lake-terminating glaciers, such as the Kaskawulsh Glacier, on the northern and eastern edges and very large glaciers that drain into Alaska to the south and west, including the Malaspina, Hubbard, and Seward glaciers. In many studies the St. Elias Range has been grouped with Alaska glaciers because of its proximity to the nearby Wrangell and Chugach Ranges.

2.4.1 Regional weather patterns

The St Elias Range experiences both maritime and continental climatic conditions, due to its proximity to the Gulf of Alaska and the Yukon interior. During the Icefield Ranges Research Project (IRRP) in the 1960s, Marcus (1974) conducted a full analysis of seasonal variations in the climatological activity in the St Elias Range. Using weather stations operating in conjunction with environmental studies during the IRRP, nine years of weather data were collected. One station was situated on the Kaskawulsh Glacier on the medial moraine of the North and Central Arms (Figure 2.5). Here, a mean value of 3.7°C for the summers of 1964, 1965, and 1966 was found. Wind measurements showed a predominantly downglacier wind, classic of glacierized valleys, with speeds up to 12 m s^{-1} (Figure 2.6). This localized wind was apparent between 50-500 m above the glacier surface, corresponding closely to the surrounding local peaks. When upglacier winds did appear, it was due to strong air-mass movements from the continental interior. Air-mass movements were described based on season, with winter patterns dominated by the wet Aleutian Low to the south and the cold, dry Mackenzie High to the north (Figure 2.7). In the summer, the northward migration of the Pacific High abuts the St Elias and Chugach Ranges and the orographic effect takes over, creating cloudy conditions and precipitation events. In addition, summer-time easterly flow along the continental front increases stormy weather on the eastern side of the range and is

identified as the primary source of summer time continental slope moisture in the summer season.

2.4.2 The Kaskawulsh Glacier

The Kaskawulsh Glacier is a land-terminating glacier approximately 70 km long located on the northern edge of KNPR (Figure 1.4), made up of four major branches: North Arm, Central Arm, Stairway Glacier, and South Arm (Figure 2.5) (Anderton, 1973; Foy et al., 2011). In previous studies it has been classified as a temperate non-surge type glacier (Macpherson and Krouse, 1969; Foy et al., 2011), based on an absence of classic indicators for surging, such as looped moraines. A maximum ice thickness of 778 m was found at the confluence of the Central and North arms, determined by seismic, gravity and geophysical surveys (Dewart, 1969; Clarke, 1969). Dewart (1969) went on to map parts of the subglacial topography, determining that the Central Arm is much thicker and a central subglacial ridge extends from the nunatak down-glacier to where the ice of the Central and North arms meet (Figure 2.8). Foy (2011) measured an average terminus retreat of 655 m for the period 1956-2007 and a decrease in area of 1.53%, with thinning in the ablation zone accompanying slight thickening in the accumulation area. The same study determined changes in volume, with an increase of $<+0.01$ km^3 a^{-1} w.e. for 1977-1995 and subsequent decrease of -0.50 km^3 a^{-1} w.e. for 2000-2007.

In terms of previous velocity measurements on the Kaskawulsh, several studies were completed as part of the IRRP. Brecher (1969) calculated surface velocities on the North Arm for four different periods in July-August 1964 using theodolite, finding a range in mean surface velocities between 120 m a^{-1} and 150 m a^{-1} over the glacier surface. He also measured velocities that fluctuated ±30 m a^{-1} above and below the seasonal mean. Often, however, the error in this study was larger than these differences in velocity, with little apparent spatial variation. Clarke (1969) confirmed these calculations with his own peak velocities of 150 m a^{-1} determined by theodolite for the summer of 1962 along the glacier centerline just above the ELA, and cross profiles that identified ice thicknesses between 362 m and 481 m. Bedrock topography was seen here to influence surface velocities through slopes oriented up-glacier. Anderton (1973) completed an in-depth theodolite study with 132 stakes at the

confluence of the North and Central arms, finding annual velocities of up to 152 m a^{-1} and 215 m a^{-1}, respectively, and summer velocities of over 200m a^{-1} and 150 m a^{-1}, also respectively. These values were consistent between 1964 and 1965.

2.4.3 The Kaskawulsh Glacier in the Holocene

Borns and Goldthwait (1966) used radiocarbon dating of vegetation to describe a retreat of the Kaskawulsh Glacier that occurred 12,000-9,000 years ago, followed by the widespread advancement of glaciers of the St Elias Range 2,600 years ago, which included the Kaskawulsh. This regional advancement reached its maximum about 300 years ago, where it remained until ~145 years ago, according to dendrochronology in the area (Borns and Goldthwait, 1966). The two lobes of the glacier were seen to act semi-independently; the north lobe reached its greatest extent in the 1750's, while the east lobe maximum was reached earlier, around 1717. A retreat up-valley followed, finding a stable terminus position around 1870. Denton and Stuiver (1969) developed a neoglacial (Little Ice Age) chronology of the Kaskawulsh Glacier advances, with the most recent advance dated to 1865, bringing the terminus to its 1965 position. Reyes et al. (2006) used white spruce trees affected by glacier movement through tilting, shearing, or dislodgement, cross-dated with glacier moraines, to establish the change in position of the Kaskawulsh Glacier terminus.

2.4.4 The Slims River and the Kaskawulsh River

The Kaskawulsh Glacier has played a significant role in the development of regional drainage systems on the eastern side of the St. Elias Mountains, and continues to influence current hydrological pathways. The Kaskawulsh Glacier provides the main source for both the Slims River (a major contributor to Kluane Lake and the Yukon River, which ultimately drains into the Bering Sea), and the Kaskawulsh River (which drains east into the Alsek River and eventually Dry Bay, Alaska). Previous terminus advances have determined the drainage patterns of Kluane Lake and the Yukon River (Bostok, 1969; Clague et al., 2006). The Slims River discharges up to 400 m^3 s^{-1}, and is the dominant source of water for Kluane Lake's 1.26 x 10^3 km^2 drainage basin (Johnson, 1986; Clague et al., 2006; Brahney et al., 2008). The amount and turbidity of water in both systems varies according to the meltwater produced by the Kaskawulsh Glacier, although it has been observed that a significant

proportion of the Slims River drainage is seasonally pirated by the Kaskawulsh River to the east (Figure 2.9) (Fahnestock, 1969; Barnett, 1974; Johnson, 1986). The seasonal shift adjusts the concentration of suspended sediment load in both rivers, increasing the dissolved sediment load in the Slims, the effects of which are felt far downstream (Bryan, 1972). This suspended component often travels further and can affect salmon stocks along the Yukon River (Johnson, 1986; Fleming, 2005). Eventually, the headward erosion of the much-steeper Kaskawulsh River system and the retreat of the Kaskawulsh Glacier could make this piracy permanent (Bryan, 1972). The seasonal change in water source for the Slims River is a subject for continued study, and the proportion and timing of water diverted to the Kaskawulsh River has not been quantified (Crookshanks and Gilbert, 2008). A larger diversion of both sediment and water to the Kaskawulsh River system was directly related to the advance of the Kaskawulsh Glacier during the Little Ice Age, so that for some periods, Kluane Lake drained to the south through the Kaskawulsh and Alsek Rivers (Bostock, 1969; Clague et al., 2006; Brahney et al., 2008). Changes in the terminus position of the Kaskawulsh Glacier could therefore have a significant effect on regional hydrology.

Figure 2.1 Glacier motion processes and the subsequent vertical velocity profiles: a) ice deformation only, b) ice deformation and basal sliding, and c) ice deformation, basal sliding and bed deformation (Benn and Evans, 1998).

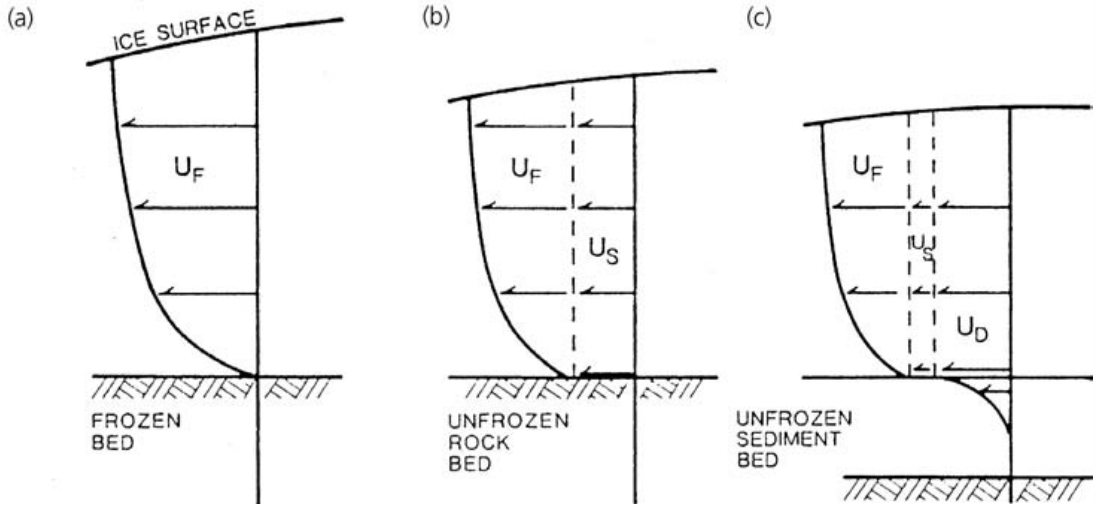

Figure 2.2 Routes for surface water migration to the glacier bed for an idealized temperate glacier (Fountain and Walder, 1998).

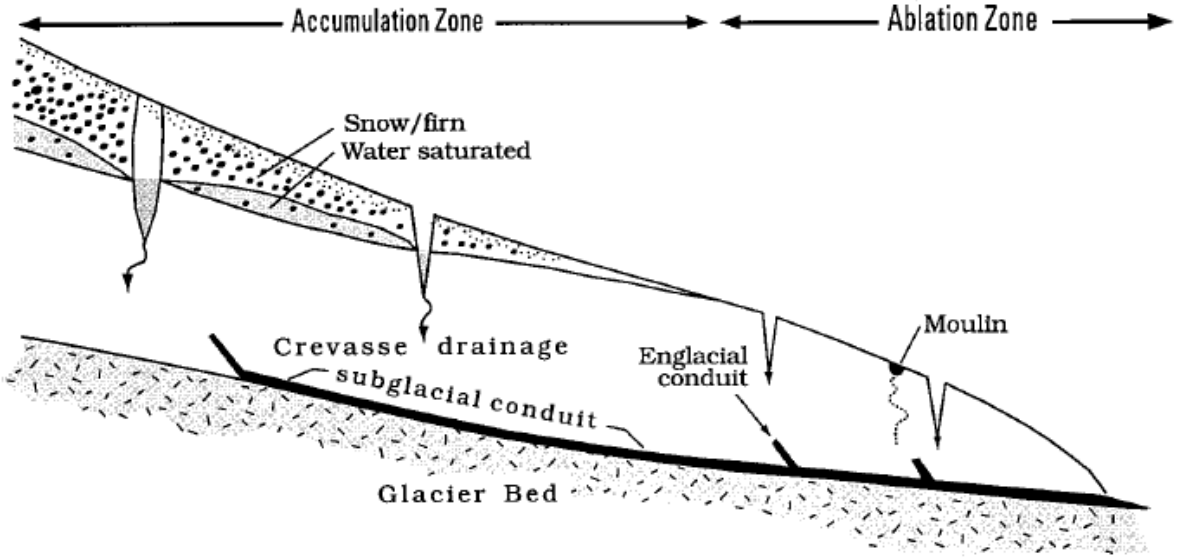

Figure 2.3 Rhodamine dye-return curves from a) Storglaciaren (Hock and Hooke, 1993) and b) Haut Glacier d'Arolla (Nienow et al., 1998). Single, extreme spikes are indicative of an efficiently draining channelized system, while more gradual peaks are indicative of a distributed system.

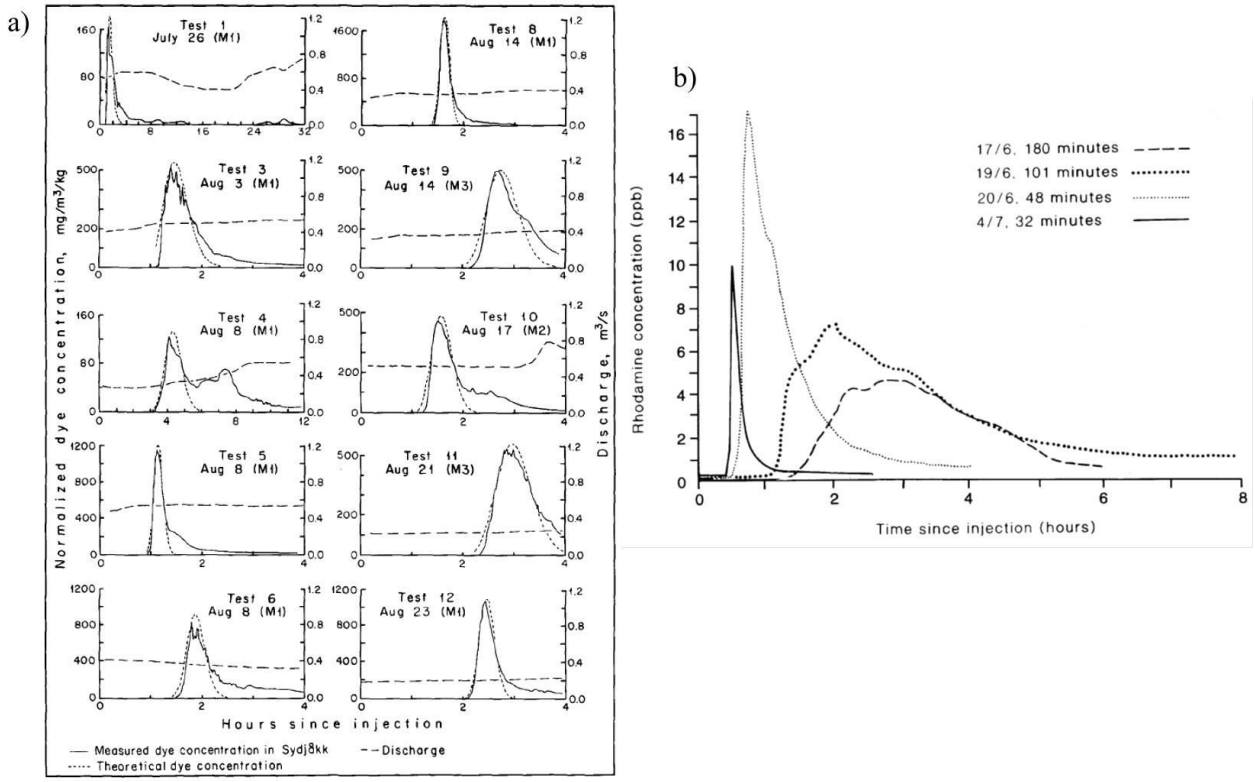

Figure 2.4 Schematic of the regelation process, with energy and mass fluxes, and water and heat flow (Benn and Evans, 1998).

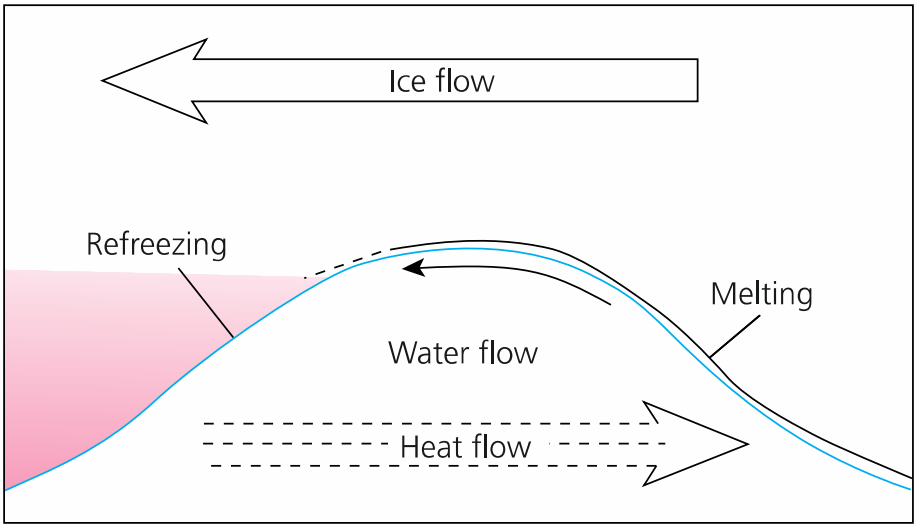

Figure 2.5 Location map with dGPS stations along the Kaskawulsh Glacier.

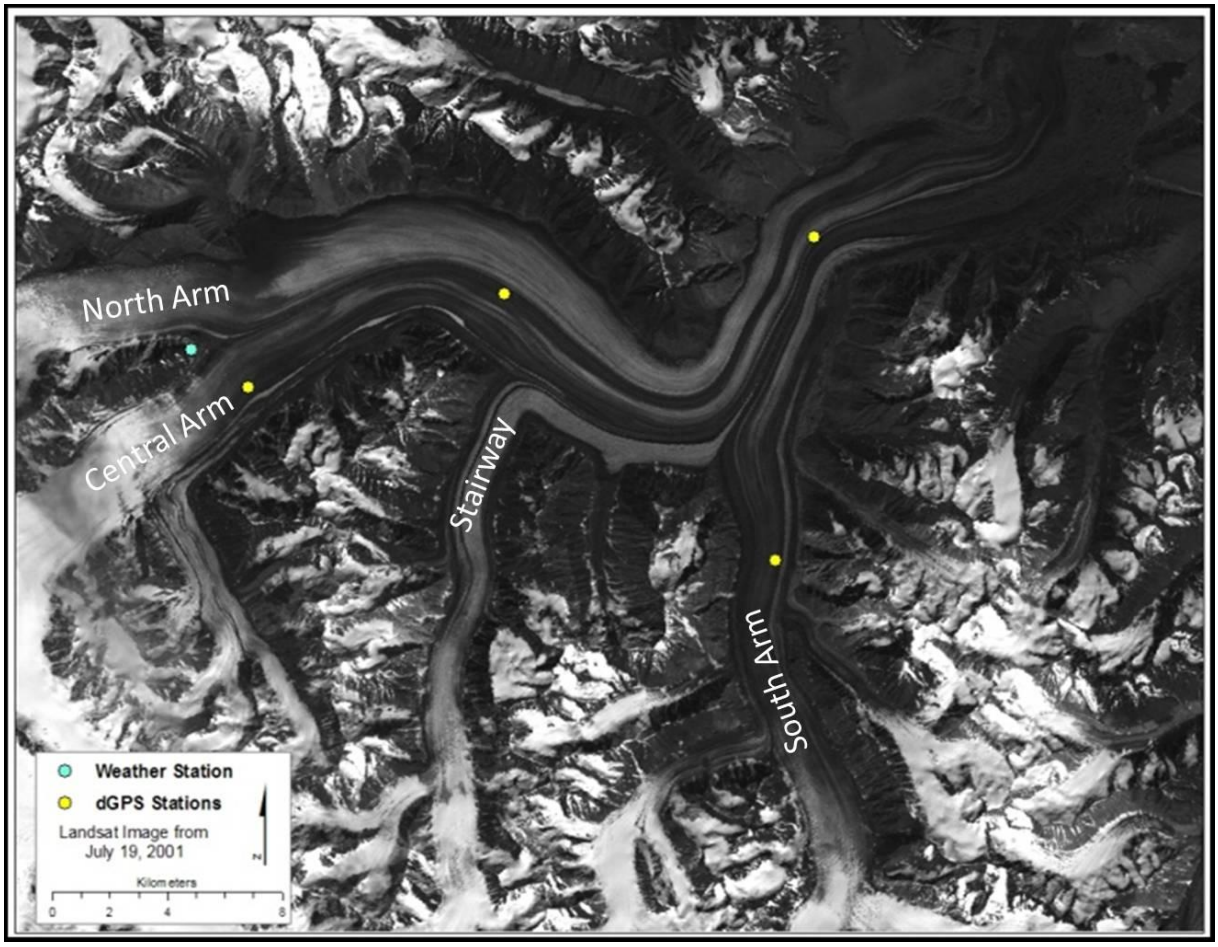

Figure 2.6 Wind rose diagrams for the Kaskawulsh Glacier for the summer of 1964 from Marcus (1974) showing the predominantly downglacier wind direction. Data was collected from near the confluence of the Central and North arms.

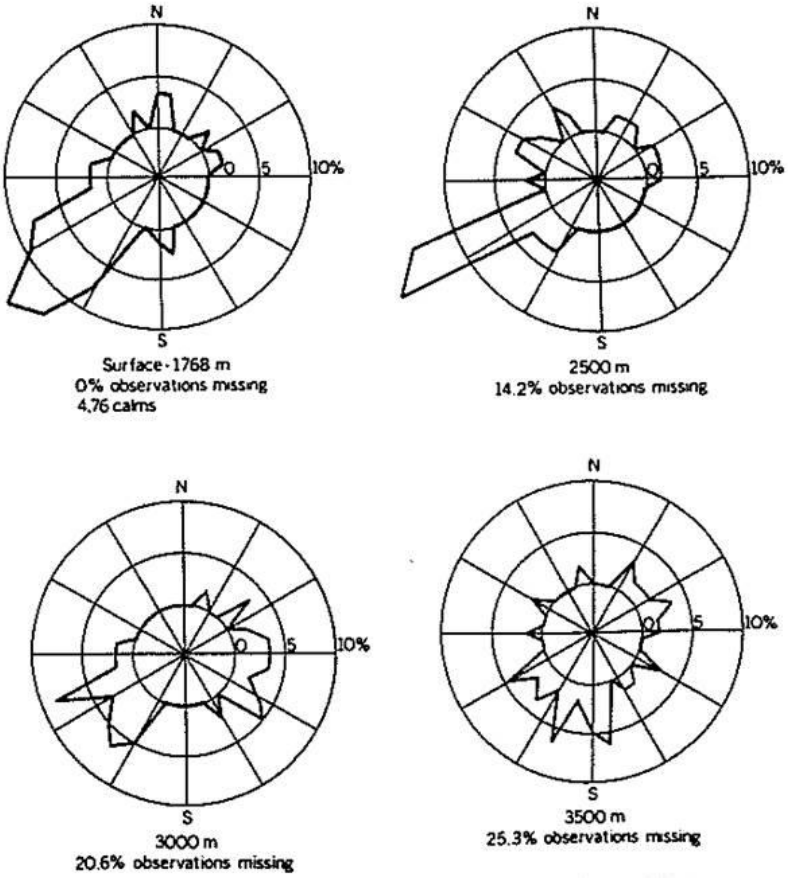

Figure 2.7 Generalized weather patterns in the Gulf of Alaska and over the St Elias Range (Marcus, 1974). A progression of the Aleutian Low poleward a) in a classical summer position, b) the disruption of the this classical position by the Pacific High that forces lows north, increasing stormy weather on the continental side of the St Elias, and c) the classic position of the Pacific High later in the summer season.

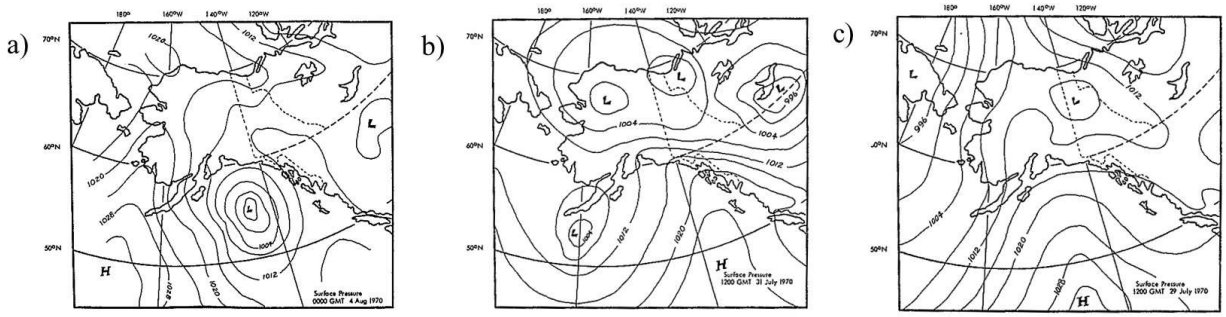

Figure 2.8 A map from Dewart (1969) showing subglacial topography at the confluence of the North and Central arms of the Kaskawulsh Glacier, using a contour interval of 200 m and the edge of the glacier at the time of surveying as the zero contour.

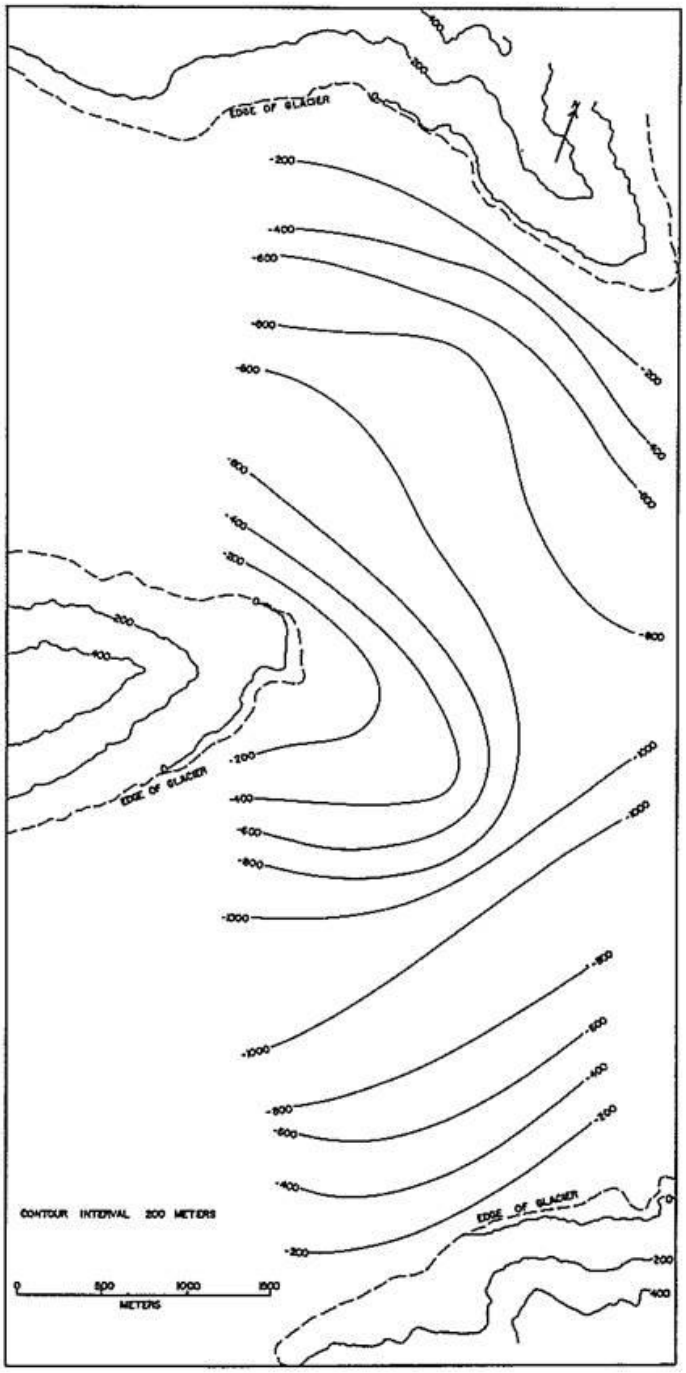

Figure 2.9 Drainage basins of the Slims and Kaskawulsh rivers in relation to the Kaskawulsh Glacier (Fahnestock, 1969).

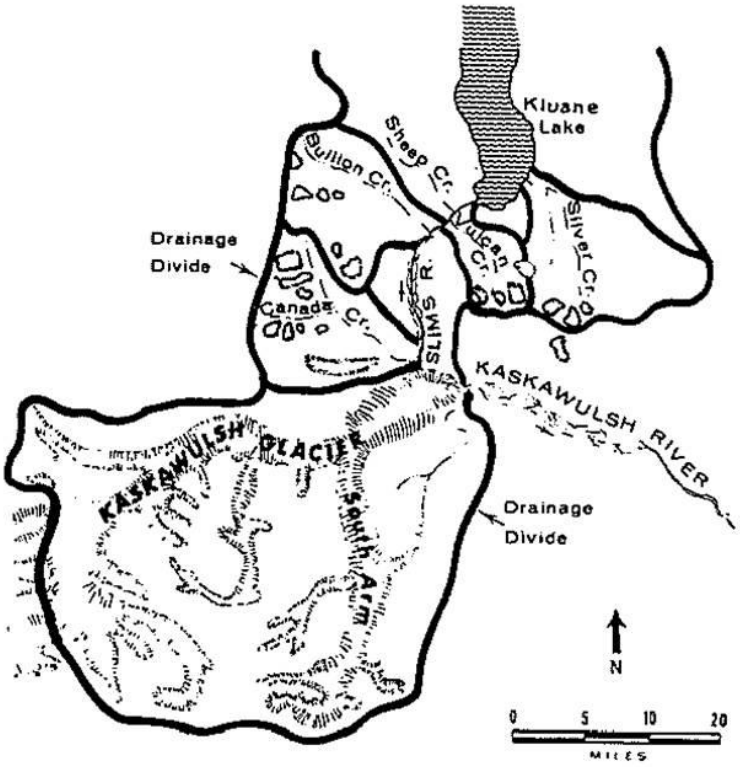

Fig. 3. Drainage basin map.

Chapter 3 Methods

This study utilizes recent advances in field measurements and remote sensing techniques to examine spatial and temporal variations in ice motion across the Kaskawulsh Glacier. The field measurements serve to document short-term (hourly to daily) and seasonal velocity patterns at a network of differential global positioning system (dGPS) units placed along the Kaskawulsh Glacier near the center flow line. The dGPS results are then used to calibrate and validate the ice motion patterns determined from remote sensing techniques, specifically from Radarsat-2 image pairs. These provide a view of velocity patterns across the entire glacier surface on a medium-term (24-day) timescale.

3.1 Differential GPS

In this study, dGPS units were installed on the surface of the Kaskawulsh Glacier to track ice motion at a very high temporal (hourly to daily) and spatial (approximately cm) resolution. This method has previously produced reliable ice motion results in isolated mountainous regions such as the Baltoro Glacier in the Karakoram, and the Amery Ice Shelf in Antarctica (Copland et al., 2009; Zhang and Andersen, 2006). New dGPS base stations were specially built for this project with extreme weather conditions and remote situations in mind, based on designs used in the High Arctic by the University of Alberta IPY *Glaciodyn* project (Figure 3.1b). Each base station contains:

- A dual-frequency Trimble R7 differential GPS receiver connected to a Zephyr Geodetic antenna
- A 2GB Sandisk Extreme III Compact Flash memory card
- A 20W BP Solar panel with solar regulator
- Two 100Ah deep cycle absorbed glass mat (AGM) sealed 12 volt batteries
- Custom-made antenna to receiver cables and connectors from MRO electronics, Edmonton, Alberta.
- A waterproof Underwater Kinetics box to hold the batteries, solar regulator and GPS receiver.
- Aviation-grade Amphenol plugs to provide waterproof quick disconnect ports on the outside of the box for easy removal of power and antenna cables when the unit is repositioned due to surface melt.

At each station the dGPS antenna was securely mounted to the top of a 3 m long, 1" diameter threaded steel pole. This pole was connected to a second 3 m pole, for a total of 6 m, and drilled at least 4.5 m into the ice at the start of the data collection period (Figure 3.1a). The mounting poles emerged from the glacier due to melt during each summer, so were redrilled approximately twice per summer season to maintain stability.

On July 29, 2009, three of these specialized dGPS base stations were installed just below the equilibrium line, 39.0 km from the terminus of the glacier ('Upper Station'), 28.6 km from the terminus in the ablation area ('Middle Station'), and 12.5 km from the terminus ('Lower Station'), so that longitudinal variations in velocity could be documented (Figure 3.2, Table 3.1). In May 2010 an additional dGPS unit of the same design was added to the South Arm, a tributary of the Kaskawulsh Glacier.

The units were programmed with different winter and summer programs to optimize the power available from the battery bank. During the winter months the units were programmed to power up at noon each day and take measurements for three hours at 15 second intervals and to store data in a single daily file. In summer the measurements were taken continuously (24 hours per day) at 15 second intervals and also stored in daily files. The winter program was switched to the summer one each spring (typically May), and the summer program was switched back to a winter program towards the end of each melt season (typically August). An elevation mask of 5° and PDOP (Positional Dilution of Precision) mask of 20 was used for all measurements.

3.2 The Precise Point Positioning method

In the past, dGPS networks installed on glaciers have typically made use of relative positioning techniques, which require at least two receivers to be in close proximity to each other: usually a base station on an area of non-motion (e.g. bedrock), and the rest of the network on the feature being tracked (e.g. glacier). According to King et al. (2002), at least three types of errors are associated with this method:

1) *Satellite errors* - issues with satellite coordinates and clocks;
2) *Receiver errors* – issues with receiver clocks;

3) *Atmospheric errors* - issues with signal delays in the ionosphere and troposphere;

These are typically dealt with through the application of various mathematical models, multiple satellite configurations and double differencing techniques. Unfortunately, these techniques require that at least two receivers are able to 'see' at least the same four satellites (and preferably many more). This limitation can be difficult in mountainous areas as high topography can prevent the viewing of the same satellite network between different receivers, and the receivers need to be relatively close to each other to observe the same satellites (ideally less than ~10 km). The relative positioning method also assumes that the base station is not moving, which can be a difficult assumption to make on large glaciers where there are few available flat bedrock exposures and moraines may have to be used instead.

The Precise Point Positioning (PPP) technique, used in this study, removes *satellite errors* by using highly precise satellite clock estimates based on a global network of receivers. PPP Direct software developed by Natural Resources Canada (NRCan) (http://www.geod.nrcan.gc.ca/products-produits/ppp_e.php) is used to process the data collected on the Kaskawulsh. NRCan provides the most accurate values for satellite orbits (~2 cm) and clocks (0.1 ns) some 14 to 21 days after data collection (NRCan, 2004). This means that results are not available for real-time processing. *Receiver errors* are minimized by calculating a least-squares solution for the coordinates of a single unit from multiple satellites. *Atmospheric errors* are addressed by applying a mathematical model based on meteorological data to model tropospheric delay (King et al, 2002; Zumberge et al. 1997; NRCan, 2004).

Error is minimized internally in the processing of the data through the NRCan PPP software, where corrections are applied for the majority of possible error sources, including ionospheric and tropospheric effects, ocean loading and multipath effects (changes in satellite geometry) (Craymer, 1998; NRCan, 2004). Each unit records coordinates independently, so they can be considered as 'absolute' positions. Motion calculated from these positions can then be attributed to ice motion alone. By removing the need for a base station and

calculating absolute positions of each unit independently, the PPP method becomes a more versatile option for remote regions (Copland et al., 2009; Zhang and Andersen, 2006). This technique is well suited for this project, as no base station currently exists within 30 km of the study area, and the PPP method has previously produced results comparable to relative processing (King et al., 2002; King, 2004; Orgiazzi et al., 2005; Zhang and Andersen, 2006).

In this study Trimble Configuration Toolbox (version 6.7) and Trimble GPS Configurator (version 3.52) were used to program the Trimble R7 dGPS stations. Downloading was undertaken with Trimble GPS configurator (version 3.52) or directly from the built-in Compact Flash card. The winter acquisition period of 3 hours per day was chosen as a balance between preserving battery life and maximizing the period of data collection to gain the most accurate results possible (positional accuracy of ±4 cm is estimated with 2 hours of collection time; NRCan, 2007). Raw data was collected in the Trimble t01 file format, and then converted to RINEX file format using Trimble 'Convert to Rinex' software (version 2.0.0.5). It was then uploaded to the PPP Direct software online. The PPP Direct software produces a suite of outputs, including a PDF summary of error calculations, a visualization of all measurements relative to the average position, a set of average coordinates in the North American Datum (NAD) 1983 coordinate system, and vertical height. Included is a .csv file of the coordinates and ellipsoidal height for each measurement (every 15 seconds), which was then imported into Matlab 7.10 (2010) for further calculation and manipulation. Once in the Matlab environment, scripts developed by members of the Laboratory for Cryospheric Research at the University of Ottawa here used to calculate the Universal Transverse Mercator (UTM) coordinates for each data point. This coordinate system uses meters as the base unit and was therefore be used to calculate total horizontal displacement (*c*) using the Pythagorean Theorem:

$$c = \sqrt{(a^2 + b^2)} \qquad \textbf{(4)}$$

where *a* is the easting coordinate and *b* is the northing coordinate. The direction of motion was calculated from the UTM coordinates in MS Excel. Total displacement was converted to rates by simply dividing the value by the period for which it was calculated. For standardization purposes, all values have been corrected to m a^{-1}.

3.3 Secondary ground measurements

Weather stations, air temperature loggers and snow depth sounders were used to provide information about climatic conditions, surface melt rates and snow accumulation. Four Hobo U23-001 automated air temperature and relative humidity loggers housed in temperature shields were mounted on the dGPS stations, and programmed with HOBOware software to take measurements every ½ hour. A Judd automated depth sounder was mounted on a cross-arm attached to the Upper and South Arm stations in May 2010 (prior to the onset of summer melt), and connected to an Onset Energy Logger Pro data logger housed in the dGPS case. These loggers were powered by the same battery bank as the dGPS receiver, and also contained 8 AA lithium backup batteries. The sounders use a sonic pulse to measure the distance between the sensor and the glacier and/or snow surface, with reductions in distance over time attributed to snow accumulation and increases attributed to surface snow or ice melt. In addition, the Geological Survey of Canada (GSC) has had an automated weather station in operation on the nunatak at the confluence of the North and Central Arms since 2006 (~2.3 km north of the Upper dGPS station at 139º 09.97' W, 60º 44.47'N) (Figure 3.2). This station recorded temperature, wind speed and solar radiation for the entire duration of the 2009-2011 dGPS measurement period.

3.4 Remote sensing

Remote sensing image analysis is used in this study to determine glacier velocities on the Kaskawulsh Glacier in areas surrounding the dGPS stations. Early studies, such as Scambos (1992), employed *feature tracking* techniques to determine the motion of Ice Stream E of the Siple Coast, Antarctica. This technique relies on identification of the same surface features in a pair of images to determine displacement, and thus relies on optical satellite imagery from sensors such as Landsat and Advanced Spaceborne Thermal Emission and Reflection Radiometer (ASTER) due to their extensive coverage and accessibility. For example, Berthier and Toutin (2008) measured surface ice motion using SPOT 5 images and cross-correlation techniques in Northwest Canada and Southeast Alaska. The usefulness of optical imagery is overshadowed by its limitations, however, which relate primarily to the inability to image the surface when there is a lack of light, cloudiness, or snow cover. Light is necessary for these passive sensors to view the surface response to sunlight, which means

that their imagery is limited or completely unavailable during winter months north of ~60°N. In regions close to oceanic moisture sources, such as the St Elias Range, clouds often block large portions of visible satellite imagery. In addition, these areas receive large amounts of snow in the winter, which reduces the contrast between features and makes optical feature-tracking problematic.

To address these issues, active satellite sensors have been developed that can image the Earth's surface regardless of darkness, cloud, and snow cover. Active satellite sensors emit their own electromagnetic energy and record how much of that energy is reflected by the surface. In particular, synthetic aperture radar (SAR) imagery has been used extensively in glaciology since the early 1990s (e.g. Gray et al., 2000), with sensors including the European Remote-Sensing (ERS) satellites 1 and 2 and the Canadian satellites Radarsat-1 and -2. SAR emits coherent microwave energy, and records the returned energy, including its amplitude, wavelength and phase properties, all of which can change depending on the properties of the surface materials. Coherence is dependent on the phase of the signal, which can be said to be 'in-phase' when the returned signal has the same wave properties (i.e., wavelength and origin) as the emitted or reference energy, or 'out-of-phase' when the returned signal does not match the same signal properties.

Different SAR processing techniques use different aspects of this information; for example, *interferometry* is based on the phase differences, or the number of partial wavelengths 'out-of-phase', of energy returned from two different satellite passes. Interferometry has been used to determine ice velocities widely across locations such as Antarctica, Greenland and Svalbard (Joughin et al., 2002; Murray et al., 2003; Kääb, 2005; Pritchard et al., 2009). A variation on interferometry, called *speckle tracking*, uses the constructive or destructive interference of surface materials to coherent microwave energy to establish a unique pattern at the sub-pixel scale that can be identified in repeat satellite image pairs over time. This study focuses on the use of SAR speckle tracking as a primary method to determine surface velocities across the Kaskawulsh Glacier, with feature tracking as a secondary method when speckle tracking is not possible (Gray et al., 2000; Quincey et al., 2009).

3.4.1 Speckle tracking theory

The speckle tracking technique requires a pair of single look complex (SLC) images from repeat orbits, such as Radarsat-2 imagery, which repeats its orbital pass every 24 days. One image is designated as a reference image and the other as a slave image. The slave image is searched for a matching area of spectral signal, or image chip, from a subset of the reference or master image via a two dimensional cross correlation method (Short and Gray, 2004; Joughin, 2002; Strozzi et al., 2008). To make significant matches the two SAR images must maintain coherence, which requires that they have similar satellite geometries, including baselines (distance between the two satellites), orbital periods, and surface properties. Winter images tend to produce better results, as surface properties remain unchanged for longer periods. Before displacements can be converted from slant range (distance between the sensor and target measured on a straight line) to ground range (distance from the actual satellite path to the target), a digital elevation model is used to remove the topographic component (Figure 3.3). The topographic component describes the influence of changes in elevation on the radar response, which can lead to false measurements if not removed (Figure 3.4). Displacements are then calibrated using stable, stationary reference points, such as rock outcrops where velocities are known to be zero (Short and Gray, 2005; VanWychen et al., 2012). Validation for ice motion vectors determined from speckle tracking is provided by comparisons with:

1) Surface flow features (e.g. moraines) visible in optical imagery,
2) Velocities calculated from data collected by dGPS stations installed on the glacier surface,
3) Orientations derived from the same dGPS data,
4) Areas of known zero motion (i.e. exposed bedrock).

Speckle tracking is the most applicable of SAR techniques to this study, overcoming many limitations of interferometry. For example, interferometry can only determine ice velocities in the satellite look direction, whereas speckle tracking is not constrained by look direction.

3.4.2 Potential sources of error

In previous studies some issues have been identified when the speckle tracking technique has been applied to small, polar glaciers. In particular, the likelihood of false matching of

identifiable signal returns, or ”image chips,” increases with reduced image chip size, which is required for smaller scale glaciers and especially on homogenous areas where there are multiple potential matches (Short and Gray, 2004). Similarly, strong features, such as crevasses, can overwhelm the speckle tracking technique, increasing velocity errors by as much as 10 – 20 m a^{-1} (Short and Gray, 2004). Finally, DEM accuracy plays a major role in the reliability of the final results, as the DEM determines reference velocities and corrects the range displacement (Figure 3.4). Giles et al. (2009) also identified image co-registration, the lack of tie points, and incorrect displacements due to slant range, which can interact with mountains and other obstacles, as issues when dealing with SAR imagery over the Mertz Glacier Tongue in East Antarctica. However, the speckle tracking technique remains applicable here as these errors can be minimized via the use of fine resolution imagery and the application to a large, relatively fast-flowing glacier such as the Kaskawulsh.

Rignot and Kanagaratnam (2006) used speckle tracking techniques applied to Radarsat-1 imagery collected in the fall of 2000 and spring of 2005 to determine ice velocities on the GrIS averaged over 24-day periods (1 orbital cycle). Seasonal velocity patterns were recorded, with little change over the fall period. Howat et al. (2007) and Howat et al. (2008) successfully used speckle tracking techniques on two of Greenland’s main outlet glaciers, Kangerdlugssuaq and Helheim Glaciers, to determine discharge and mass losses between 2000 and 2006 with uncertainties of ±3%. Similarly, Joughin et al. (2008) used speckle tracking to measure ice velocities on the western coast of the GrIS between 2004 and 2007, including Jakobshavn Isbrae, the largest outlet of the GrIS. The work done by VanWychen et al. (2012) on Devon Ice Cap in the Canadian High Arctic used the same techniques, imagery, and software as this study, producing reliable results for Belcher Glacier, the main outlet of the ice cap, with errors of 4.29 ±4.22 m a^{-1}. Speckle tracking is thus proving to provide robust data for remote glaciers and their surroundings.

The software used here utilizes Matlab scripts developed by Dr. Laurence Gray, formerly of the Canada Center for Remote Sensing. The Radarsat-2 satellite imagery was provided by the Canadian Space Agency (CSA) Science and Operational Applications Research – Education (SOAR-E) initiative (January 18 and February 26, 2010), and through a partnership with

Parks Canada (October 2010 through March 2011). A total of 37 acquisitions were made, including a set of 10 ultra-fine beam images from the spring of 2010 and 17 fine beam images from the fall and winter of 2011 (Table 3.2). Imagery acquired in the ultra-fine (20 km swath and 3 m resolution) and fine beam (50 km swath and 8 m resolution) modes provide optimal resolutions and spatial coverage (Figure 3.5; Table 3.3). Ultra-fine beam imagery was chosen for the higher resolution, while the fine beam imagery was chosen to compliment this with a larger footprint, so that the entire study area was captured in a single image.

Figure 3.1 a) Lower dGPS Station on September 19, 2010 (60°45.127'N 138°57.938'W), b) Interior view of a dGPS station, and c) Close-up view of the Upper dGPS Station (60° 43.619 'N 138°07.986' W) complete with Hobo temperature sensor and Judd snow depth sounder.

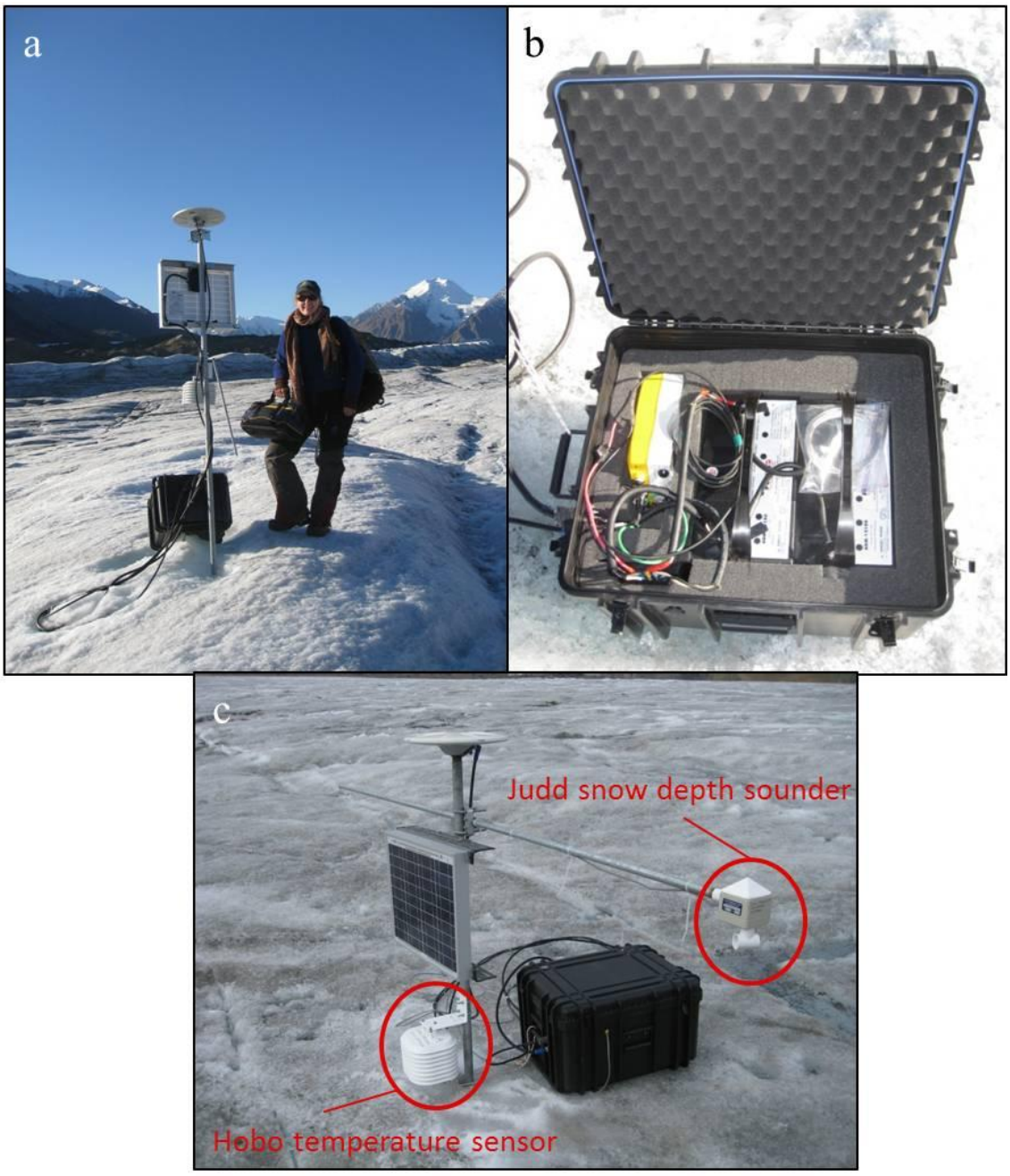

Figure 3.2 Map identifying the different flow units of the Kaskawulsh Glacier, dGPS stations and location of the Geological Survey of Canada weather station.

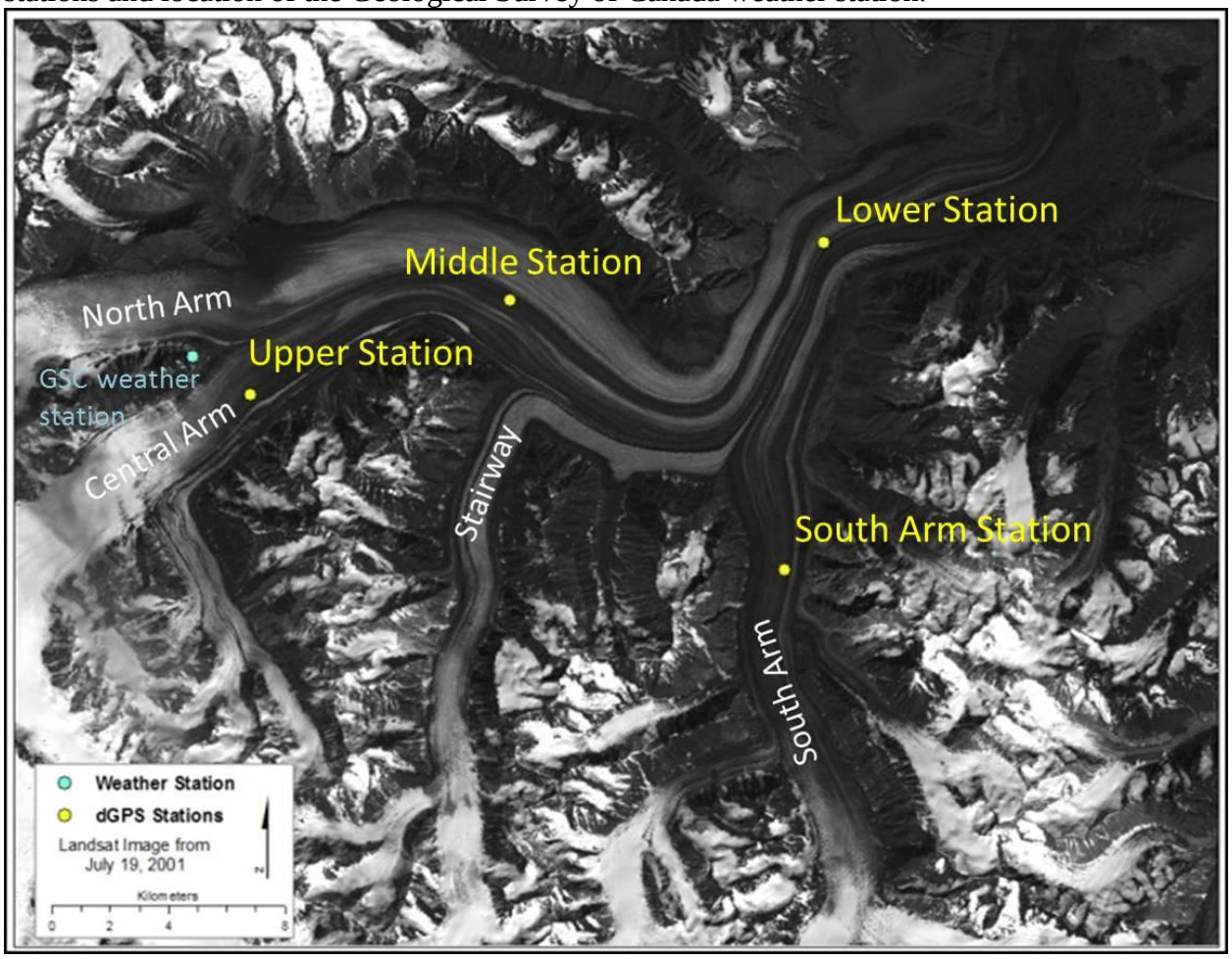

Figure 3.3 Schematic defining ground and slant ranges in relation to satellite flight path and target on the ground (ESA, 2012)

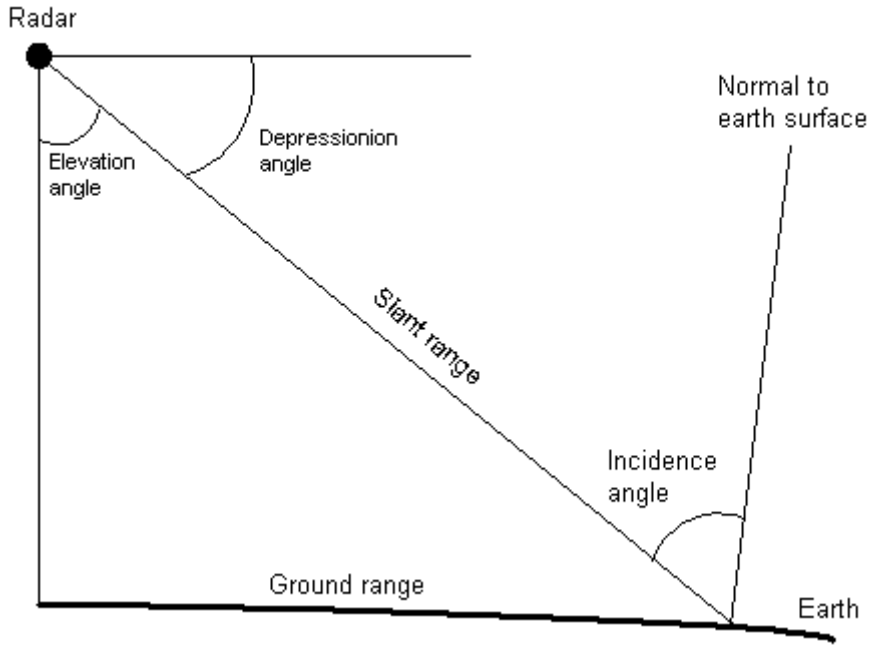

Figure 3.4 Illustration of a potential source of DEM inaccuracy when using off-nadir satellite imagery (Kääb, 2005)

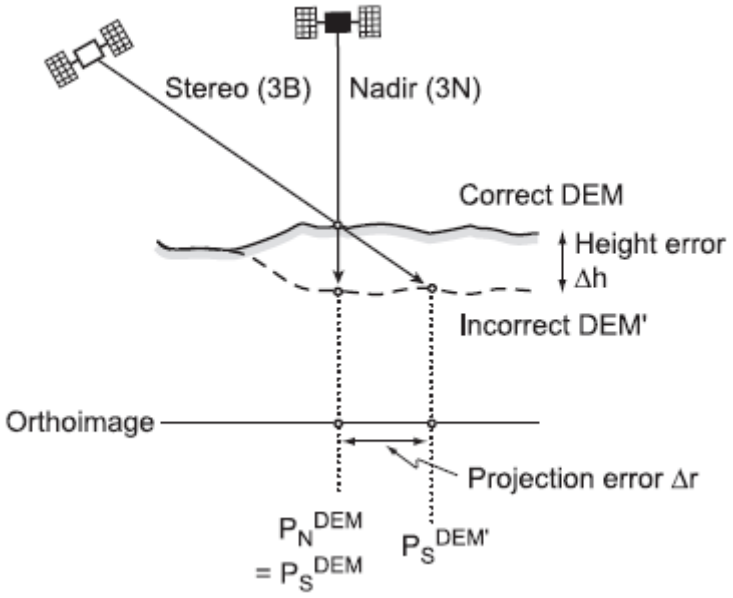

Figure 3.5 For this study, satellite image footprints for a) ultra-fine and b) fine beam Radarsat-2 imagery acquired as they appear on a Landsat optical image from July 2001 and June 2004, respectively.

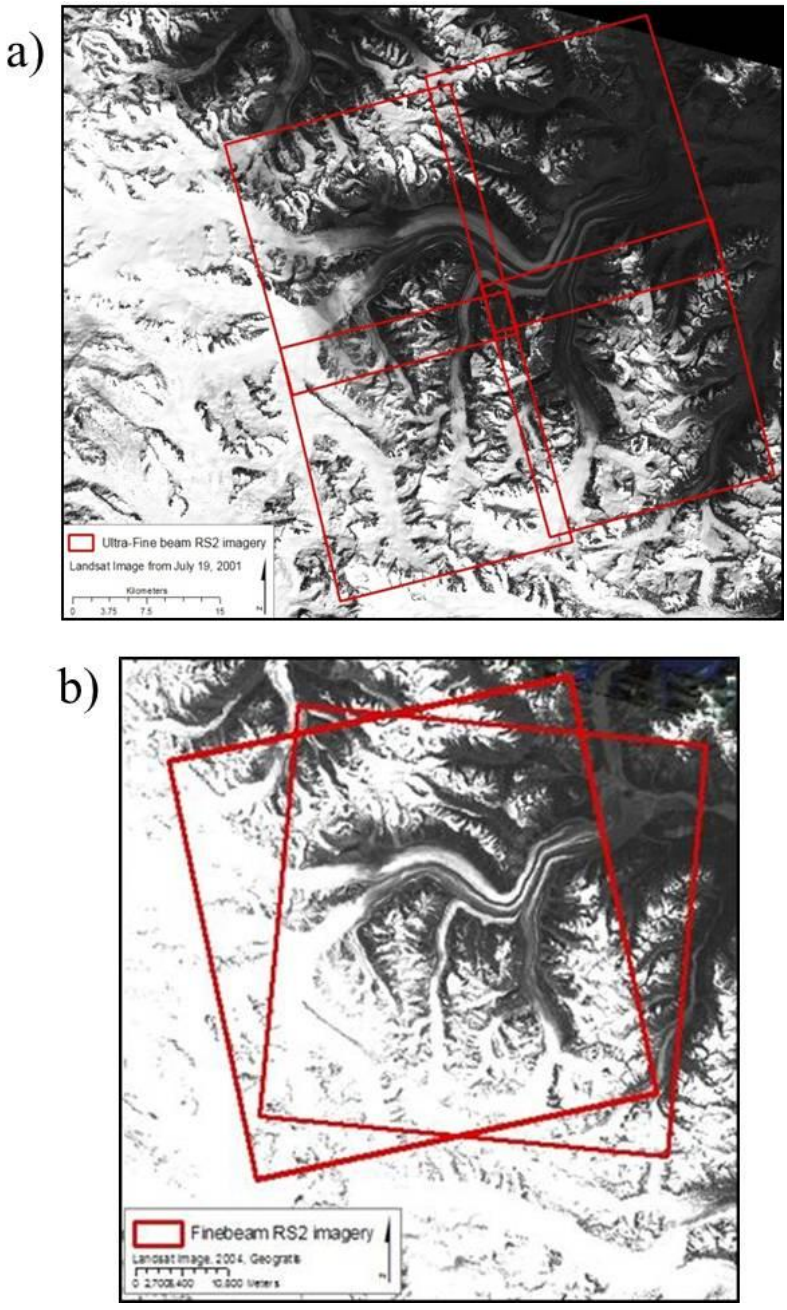

Table 3.1 Locations of dGPS stations installed in 2009, including supplemental instrumentation

Station name	Date of installation	Type of installation	Coordinates (2009)	Coordinates (2011)	Elevation (m a.s.l.)
Lower	July 26, 2009 May 5, 2009	dGPS receiver Temp sensor	60°46.046'N 138°46.190'W	60°46.140'N 138°45.957'W	1185.0
Middle	July 26, 2009 May 5, 2009	dGPS receiver Temp sensor	60°45.194'N 138°58.162'W	60°45.127'N 138°57.938'W	1547.0
Upper	July 26, 2009 May 5, 2010 May 5, 2010	dGPS receiver Temp sensor Snow depth sensor	60°43.549'N 138°08.115'W	60°43.619'N 138°07.986'W	1730.0
South Arm	May 5, 2010 May 5, 2010 May 5, 2010	dGPS receiver Temp sensor Snow depth sensor	-	60°30.031'N 138°48.029'W	1504.5

Table 3.2 Radarsat-2 imagery acquired over the winters of 2009-2010 and 2010-2011 for speckle tracking.

Date	Mode	Partner(s)
Jan 18, 2010	Fine Beam	Feb 11, 2010
Jan 27, 2010 (x2)	Ultra Fine Quad Pol	Feb 20, 2010 (x2)
Jan 26, 2010 (x2)	Ultra Fine Quad Pol	Feb 19, 2010 (x2)
Rotation 1		
Oct 20, 2010	Fine Beam	Nov 13, 2010
Nov 13, 2010	Fine Beam	Oct 20, 2010 and Dec 7, 2010
Dec 7, 2010	Fine Beam	Nov 13, 2010 and Dec 31, 2010
Dec 31, 2010	Fine Beam	Dec 31, 2010 and Jan 24, 2011
Jan 24, 2011	Fine Beam	Dec 31, 2010 and Feb 17, 2011
Feb 17, 2011	Fine Beam	Jan 24, 2011
Rotation 2		
Nov 2, 2010	Fine Beam	Nov 26, 2010
Nov 26, 2010	Fine Beam	Nov 2, 2010 and Dec 20, 2010
Dec 20, 2010	Fine Beam	Nov 26, 2010 and Jan 13, 2011
Jan 13, 2011	Fine Beam	Dec 20, 2010 and Feb 6, 2011
Feb 6, 2011	Fine Beam	Jan 13, 2011 and Mar 2, 2011

Table 3.3 Radarsat-2 beam modes and characteristics (http://www.radarsat2.info/about/r2_brochure.pdf).

Beam Mode	Nominal Swath Width	Approximate Resolution (Range)	(Azimuth)	Approximate Incidence Angle	Polarization
Ultra-Fine	20 km	3 m	3 m	30° - 49°	Single Polarization
Multi-Look Fine	50 km	8 m	8 m	30° - 50°	
Fine	50 km	8 m	8 m	30° - 50°	Single Polarization OR Dual Polarization
Standard	100 km	25 m	26 m	20° - 49°	
Wide	150 km	30 m	26 m	20° - 45°	
ScanSAR Narrow	300 km	50 m	50 m	20° - 46°	
ScanSAR Wide	500 km	100 m	100 m	20° - 49°	
Extended High	75 km	18 m	26 m	49° - 60°	Single Polarization
Fine Quad-Pol	25 km	12 m	8 m	20° - 41°	Quad Polarization
Standard Quad-Pol	25 km	25 m	8 m	20° - 41°	

Chapter 4 Results

In this chapter a comprehensive description of the velocity structure of the Kaskawulsh Glacier is presented. First, the dGPS measurements are addressed, with a focus on seasonal regimes. This is followed by a short evaluation of the error associated with these measurements. A section on the validation of the speckle tracking measurements follows, with the dGPS measurements playing a key role in this. Once validated, a summary of the glacier-wide velocity patterns derived from the remote sensing measurements is presented in chronological order. Finally, a short summary of air temperature patterns and surface melt and snowfall events over the two year period is presented. Note that all horizontal velocities presented here have been standardized to values of m a^{-1} for ease of comparison.

4.1 dGPS measurements

Nearly two years of continuous data were successfully collected from the three dGPS stations installed along the main branch of the Kaskawulsh Glacier starting in July 2009 (Julian Day (JD) 205), and ending in June 2011 (JD 157 at the Middle Station, JD 178 at the Upper Station and JD 194 at the Lower Station) (Figures 3.2 and 4.1). On the South Arm tributary, data was collected from JD 241 (2010) to JD 105 (2011) and JD 119 (2011) to JD 196 (2011). For seasonal velocity plots, dGPS velocities are shown as a 3 day running mean to remove high frequency noise, with Julian Days as the time scale. For figures which focus on individual high velocity events, both the original daily dGPS data and the 3 day running mean are shown.

4.1.1 dGPS validation

During processing of the dGPS data, short periods showing anomalously high velocities were examined and filtered on an individual basis. For example, positions calculated for a single 15 sec period sometimes showed large discrepancies (up to km) from all other positions calculated from that day, suggesting that the GPS solution for that 15 sec period was in error. Similarly, on days when anomalously large daily velocities were calculated, the individual 15 sec periods were examined for outliers. Errors of this type were verified against changes in horizontal direction and height and removed from the daily position calculations if there were extreme departures from surrounding values (±10 days). This increased the overall accuracy

of the daily position. In cases where horizontal direction was different by >10º and horizontal velocity was >5 times greater than the 10 surrounding days, the daily value was removed from the overall dataset.

In total, 1.8% of the 2009-2010 dataset was discarded, while 5.2% of the 2010-2011 dataset was rejected. The Middle Station in both years exhibited the greatest number of days with extreme values, with 2.7% in 2009-2010 and 6.3% in 2010-2011. The least error was found at the Upper Station in 2009-2010, with only 0.8% of the dataset discarded. Errors can be at least in part attributed to periods of high winds and large snowfall events, as these are two factors which would affect the ability of the dGPS to accurately record positions. High winds result in the movement of the mounting mast and dGPS antenna itself, which decreases the accuracy of the positions. Large snowfall events can potentially cover parts of the dGPS antenna, reducing the number of satellites available for positioning and reducing the strength of incoming signals.

4.1.2 Seasonal Summary

A noticeable difference in average seasonal velocities is evident, with velocities also varying slightly between stations and years (Table 4.1). There is also marked variability on a daily basis, particularly in the summer, but overall trends can be separated into Summer, Fall, Winter, and Spring regimes, as seen in Figure 4.1. Vertical motion also shows seasonal variability (Figure 4.1). The Summer regime is defined by a decline in horizontal velocity after the last major peak in the Spring regime, and lasted for a period of 64 days in 2010 and 71 days in 2011. During this regime, there is downward vertical motion at the Upper and Lower stations, while the Middle station shows little change. Next, the Fall regime is characterized by a period where velocities vary little and reach their annual minimum (Figure 4.1), with average speeds in Fall 2009/2010 being higher than Fall 2010/2011 at all stations (Table 4.1). Vertical motion during this period varies little, but follows the trend set by the Summer regime. The Winter regime sees the variability in both horizontal and vertical motion increase from the Fall, both on a daily basis and overall. Extended periods of horizontal acceleration and vertical uplift can be identified at all three main stations during this time (Figure 4.2). There is a distinct progression down-glacier of these events, first

registering at the Upper Station, followed a few days later at the Middle Station and finally the Lower Station. These events are accompanied by an overall slightly increasing trend in horizontal velocity leading up to the initiation of the Spring regime. The Spring regime begins with an approximate doubling to tripling of velocities over a period of ~3-10 days, with a progression up-glacier of the velocity increases from the Lower to the Upper station and an accompanying increase in vertical motion. Overall during this period the velocities are both high and highly variable (between 150 and 350 m a^{-1}), reaching their annual maximum (Table 4.1).

The transitions between Summer to Fall and Winter to Spring regimes occur relatively quickly, over a matter of days to weeks. The transition between Fall and Winter is indistinct and gradual. Similarly, Summer and Fall regimes appear to be the shortest, with the Winter regime dominating for the greatest portion of the annual cycle. Regime duration varies from year to year and between stations, with the Winter regime accounting for 41% of the 2009-2010 cycle and 39% of the 2010-2011 cycle. The Fall regime accounts for the shortest duration in 2009-2010 at 17% of the annual cycle, while the Spring regime is shortest in 2010-2011 at 11% of the annual cycle.

4.1.3 2009-2010 (Year 1)

The dataset begins with the Summer regime, where velocities at all stations have peaked. The Lower Station has the highest and earliest peak at 265 m a^{-1} on JD 211, then subsequently on JD 209 velocities peak at both the Middle and Upper stations with velocities of 358 m a^{-1} and 295 m a^{-1}, respectively (Figure 4.1). A peak in horizontal velocity indicates the initiation of the Summer regime at all stations. Another, smaller spike in velocity during this Summer period is seen first at the Lower Station on JD 224 with a peak of 261 m a^{-1}, then on JD 228 at the Middle and Upper stations, peaking at 282 m a^{-1} and 268 m a^{-1} respectively. This last peak is followed by a steady decline in velocity until the Fall regime is established and velocities level out at 135 m a^{-1} on JD 269 at the Upper Station, and 111 m a^{-1} and 134 m a^{-1} at the Middle and Lower Stations, respectively, on JD 271. The Fall regime sees only small variation around these averages until the Winter regime begins around JD 331. The Winter regime is characterized by multiple mid-regime speed-up events, where velocities suddenly

increase by 20-30% in a matter of days. Two main events can be identified in 2009/10 at all three stations, the longest of which is 21 days at the Lower Station with a peak velocity of 178.7 m a^{-1} (Figure 4.2a). This event peaks at the Upper Station on JD 85 and moves downglacier at a propagation speed of 5345 m day^{-1} between the Middle and Upper stations and 2340 m day^{-1} between the Middle and Lower stations, peaking at the Lower Station on JD 94, nearly ten days later (Table 4.2). The other event shows nearly simultaneous initiation of the speed-up events on JD 52. The Spring regime peak occurs at the Lower Station on JD 149 at 336.2 m a^{-1} and at the Middle Station also on JD 149 at 263.8 m a^{-1}. Finally, the spring peak at the Upper Station occurs on JD 150 at 250.5 m a^{-1}. The initiation of this increase, when velocities begin to rise above average winter velocities, similarly occurs at the Lower Station first and subsequently at the Middle and Upper stations.

4.1.4 2010-2011 (Year 2)

The 2010-2011 velocity cycle follows a similar overall pattern to that in 2009-2010 (Figure 4.1). The Summer Regime of decreasing velocity is initiated at all stations on JD 205, with occasional short-lived velocity spikes. The decline in velocity lasts until the Fall Regime is reached on JD 265, where average velocities of 128.3 m a^{-1} (Lower), 105.3 m a^{-1} (Middle), and 127.7 m a^{-1} (Upper) are reached (Table 4.1). These velocities are maintained with little variation until the first Winter speed-up event which peaks at the Upper Station on JD 6 at 162.1 m a^{-1}, moving down-glacier at a propagation speed of 2138 m day^{-1} to the Middle Station, which peaks on JD 11 at 160.7 m a^{-1}, and then continues down-glacier at a speed of 2730 m day^{-1} to the Lower Station, peaking on JD 17 at 188.0 m a^{-1} (Figure 4.2b). Some vertical motion is seen during this speed-up period, with ~0.25 m of uplift occurring at the Lower Station and ~0.10 m at the Middle Station. The Winter 2010-2011 Regime sees one other major event that is readily distinguishable at all stations, which peaks at the Upper Station on JD 77 at 180.4 m a^{-1}, where very little vertical uplift is seen. The Middle Station sees this peak on JD 79 at 185.2 m a^{-1}, a down-glacier propagation speed of 5345 m day^{-1}. This continues down-glacier at a speed of 2340 m day^{-1} to the Lower Station, which peaks on JD 86 at 242.2 m a^{-1}. The Lower Station also sees the most substantial change in vertical position, with over 0.5 m of uplift over the period of increased horizontal velocity. A general upward trend in average Winter velocities is observed at all stations until the initiation of the

Spring regime, which starts at the Lower Station on JD 134, at the Middle Station on JD 144 and at the Upper Station on JD 147. The Spring peak occurs at the Lower Station on JD 151 at 310.8 m a^{-1} and at the Middle Station at 281.8 m a^{-1}, followed by the Upper Station on JD 152 at 211.7 m a^{-1}. The dGPS data collection period terminated in the middle of the Spring regime, between JD 157 and JD 196, due to technical issues with some of the stations.

The South Arm dataset was collected between JD 241 (2010) and JD 196 (2011), with a gap between JD 106 and JD 118 (2011) (Figure 4.1). JD 241 is mid-way through the Fall Regime, with the glacier displaying little variation in motion during this period. Once the winter regime initiates there are two main horizontal velocity peaks that can be identified. JD 30 sees a velocity of 195 m a^{-1} and JD 41 sees a velocity of 186 m a^{-1}. After these peaks, the velocity levels out at between 150 m a^{-1} and 170 m a^{-1} for about 70 days before the Spring regime is established on JD 142. The spring peak comes on JD 154 with a velocity of 349.3 m a^{-1}, which is both higher than the Lower Station's peak of 310.8 m a^{-1} and later than any of the stations on the Kaskawulsh, occurring 2 days after the Upper Station's peak on JD 152. By JD 182, the velocity has dropped back down to around 170 m a^{-1}.

4.2 Speckle Tracking

A total of 15 Radarsat-2 image pairs were acquired over 24 day intervals in the winters of 2009-2010 and 2010-2011. Ultra-fine beam imagery was acquired through the Canadian Space Agency's SOAR-E (Science and Operational Applications Research for Education) program, totaling 8 images (4 image pairs) on January 26, February 2, February 19 and February 26, 2010. Four separate images were required to gain full coverage of the study area. Two fine beam images were also acquired that winter, on January 18 and February 11, 2010. A total of 13 fine beam images (11 pairs – each image participating in two pairs) were acquired between October 2010 and March 2011 through an agreement with Parks Canada. For these images, a second rotation was scheduled to provide a two week offset from Rotation 1 using the following schedule:

Rotation 1: October 20 – November 13, 2010 (2011a, JD 293 - 317)
November 13 - December 7, 2010 (2011c, JD 317 - 341)

December 7 – December 31, 2010 (2011e, JD 341 - 365)
December 31, 2010 – January 24, 2011 (2011g, JD 365 - 24)
January 24 – February 17, 2011 (2011i, JD 24 - 48)

Rotation 2: November 2 – November 26, 2010 (2011b, JD 306 - 330)
November 26 – December 20, 2010 (2011d, JD 330 - 354)
December 20, 2010 – January 13, 2011 (2011f, JD 354 - 13)
January 13 – February 6, 2011 (2011h, JD 13 - 37)
February 6 – March 2, 2011 (2011j, JD 37 - 61)

This dataset allows full coverage of the Fall and Winter velocity regimes through the production of two velocity maps for Winter 2010 and 10 velocity maps for Fall/Winter 2010-2011(Figure 4.3).

4.2.1 Validation of Remote Sensing Results

Validation of the speckle tracking results was achieved through four independent measures:

1. *Comparison of speckle-tracking derived velocity vectors with surface flow features visible in optical satellite imagery*

Physical features on the surface of the Kaskawulsh Glacier were used to validate the glacier-wide velocity patterns. In particular, medial moraines and flow stripes are directly caused by glacier motion, which in turn closely follows the alignment of valley walls (Benn and Evans, 1998). It would be expected that ice motion vectors derived from speckle tracking would be parallel to these features and that ice closer to valley walls will move more slowly than that in the centre of the glacier due to lateral drag at the glacier margins. In the instances where speckle tracking vectors did not align closely (within 5º) with the orientation of surface features, and did not follow the assumption of faster motion near the glacier centre, the values were removed from the dataset, as in VanWychen et al. (2012). Figure 4.4 illustrates the steps taken to minimize the number of incorrectly calculated vectors in the final velocity maps.

2. *Comparison of speckle-tracking derived velocities with dGPS measured velocities* (Table 4.3)

The dGPS data was subset to calculate horizontal velocities at each station for periods that exactly matched the acquisition dates of the Radarsat-2 image pairs used for the speckle tracking. Horizontal velocities calculated from speckle-tracking were taken from the four values within one pixel (~100 m) of the dGPS stations and averaged. The horizontal velocities derived by the two methods were generally close, although there were marked outliers with some image pairs. An average velocity difference between dGPS and speckle tracking of 8.2% was found for the entire dataset (Table 4.3). The ultra-fine beam dataset had better overall accuracy, with an average velocity difference of 6.3%, while the fine beam dataset had an average difference of 10.1%. The lowest error in the fine beam dataset was found for the December 7 – December 31, 2011 pair (2011e) with an average underestimation of -1.6%, with Lower Station values of 124.9 m a^{-1} (speckle tracking) compared to 123.0 m a^{-1} (dGPS), Middle Station values of 107.1 m a^{-1} vs 107.2 m a^{-1}, and Upper Station values of 125.2 m a^{-1} vs. 119.1 m a^{-1}. Even the South Arm, which generally had the greatest differences between the speckle tracking and dGPS results, has close values: 134.4 m a^{-1} vs. 135.0 m a^{-1}. The greatest overall error was found with the November 13 – December 7 pair (2011c), where the average difference between speckle tracking and dGPS values was 223.6% if the South Arm was included; excluding the South Arm resulted in a difference of -12.6% for the three main stations (Table 4.3).

3. *Comparison of speckle-tracking derived orientations with dGPS measured orientations* (Table 4.4)

To compare the direction of displacement recorded by the two methods, the four values of flow direction calculated from speckle-tracking within one pixel (~100 m) of the dGPS stations were averaged on a daily basis. Overall, orientations matched well with those calculated from the dGPS stations. The lowest difference was found with the November 26 – December 20, 2010 pair (2011d), with only a 0.7º difference between the dGPS and speckle tracking values. The greatest error was found in the January 13 – February 6, 2011 pair (2011h), with a difference of 7.5º.

4. *Comparison of speckle-tracking derived velocities with areas of known zero motion* (Table 4.5, Figure 4.4d)

The validation of image pairs is also based on speckle tracking measurements over areas known to have zero or near zero motion, such as bedrock exposures and flat off-glacier expanses (e.g. meadow lands, lateral moraine remnants). The apparent motion in these locations provides an estimate of error in the velocity calculations due to co-registration and cross-correlation errors (mismatches). There are limited locations to perform this validation within the study region, so four sites were chosen based on proximity to the Kaskawulsh Glacier, flatness, and presence of bedrock. None of the sites were ideal, as they were either flat but not bedrock, or sloped if they were bedrock; some motion, albeit slight, could therefore be expected at any of the sites. Four adjacent points were chosen and averaged to calculate the shown value. The largest average error was found at site 3, located on a steep bedrock slope, while the smallest average error was at site 2, a flat grassy meadow (Figure 4.4d). Average error for all image pairs was 15.3 m a^{-1}, with 2010e and 2011e having the least overall error of 8.9 and 8.4 m a^{-1}, respectively, in the fine beam dataset, while 2011c had the greatest error of 48.1 m a^{-1}.

When the above validation methods were applied to the speckle tracking results, it is clear that the velocities across the ablation area of the Kaskawulsh Glacier and its major tributaries show generally good coherence. Areas where there is a loss of coherence correspond to the upper ablation and accumulation areas of each tributary, in areas where slopes are especially steep, where there is particularly fast movement and/or shear, and where there is likely high winds and snowfall. An example of one of these regions is identified in Figure 4.4b as area i, compared to area ii where coherence is maintained. In these areas, present in all image pairs in varying amounts, velocity measurements were unable to fulfill one or more of the validation requirements. The ablation areas of the North Arm, Central Arm, and South Arm, as well as the Stairway Glacier, are the areas with the best results based on these requirements. Discussion will therefore concentrate on these regions in image pairs where validation techniques were most successful and areas of poor coherence were relatively small.

4.2.2 Velocity Results from Ultra-Fine Beam Imagery

Speckle tracking of the ultra-fine imagery indicates areas of elevated velocities located on the North and Central arms of the Kaskawulsh Glacier in the Jan 26 - Feb 19 pairs (2010a and 2010b), with peak velocities of 510 m a^{-1} and 558 m a^{-1} respectively (Figure 4.5). In the Feb 2 - Feb 26 pairs (2010c and 2010d), peak velocity is seen to reach 510 m a^{-1} on the South Arm. These peak velocities are located in "hotspots", or areas of elevated velocity, located at various locations along each branch. The North Arm appears to be nearly fully encompassed by this high velocity region in this map, with elevated velocities appearing at the junction with the Central Arm and extending past the western edge of the image, a distance of >18.5 km. The Central Arm has a hotspot that is first seen ~2.5 km up-glacier from the junction with the North Arm and extends ~7.5 km up-glacier into the accumulation area. The South Arm also has an area of elevated velocities appearing ~2.5 km south of the junction with the main Kaskawulsh Glacier that extends ~19 km upglacier into its accumulation area. As expected, velocities tend to be higher towards the centerlines of the individual branches and center of the main Kaskawulsh Glacier.

4.2.3 Fine Beam Imagery

Two fine beam images were acquired in winter 2010 (2010e), which were processed to produce one velocity map (Figure 4.6). The North Arm exhibits a region of high velocity that begins at the junction with the Central Arm and extends into the accumulation area and past the western edge of the image, ~11 km up-glacier. The Central Arm has a hotspot that also appears at the junction with the North Arm. Some locally higher velocities also appear on the north side of the glacier, ~5.5 km down-glacier of the junction between the North and Central Arms, apparently relegated to the part of the ice flow originating from the North Arm.

Fall Regime 2010: Sep 22 (JD 265), 2010 – Jan 3 (JD 3), 2011

The majority of the Radarsat-2 imagery (six out of 14 images) fall within this velocity regime, as previously determined by dGPS. Areas of high velocity tend to be located near junctions between branches or in areas with extreme elevation changes, and can be seen in all image pairs (Figure 4.7). Image pair 2011b appears to exhibit the most homogenous velocity distribution, with values lower than all other image pairs (Figure 4.7b). The only earlier pair

(2011a) appears to be capturing the end of the Fall regime, with a maximum velocity of 556 m a^{-1}, while pair 2011b captures the main portion of the Winter regime. The high velocity areas are concentrated near the nunatak where the North and Central Arms meet, with areas of elevated velocity consistently extending up- and down-glacier from this location.

Winter Regime 2011: January 3 (JD 3) – May 26 (JD 146)

Four Radarsat-2 image pairs occur in the Winter regime (Figure 4.8). The highest maximum velocity reached is 357 m a^{-1} in pair 2011g, while pair 2011i peaks at only 276 m a^{-1}. The most remarkable changes in velocity occur on the South Arm. The high velocity regions mentioned in the Fall regime generally maintain their location and size, with exceptions on the Central Arm in pairs 2011h and 2011j, when the high velocity area extends to nearly the entire glacier both laterally and longitudinally.

4.3 Meteorological data

4.3.1 Temperature

Temperature data was collected at the Lower, Middle and South Arm stations between JD 157 2010 and JD 133 2011 (Figure 4.9b). The Upper Station temperature sensor failed on JD 263 2010 due to battery issues after collecting only 23 days of data, and so is left out of the results. The remaining dataset provides a view of the seasonal temperature cycle along the glacier centerline. The Lower Station (elevation 1192.5 m a.s.l.) records temperatures which are generally ~3º - 4ºC higher than those at the Middle (1551.0 m a.s.l) and South Arm (1503 m a.s.l.) stations for the Fall and Winter regimes. This variation results in lapse rates of 7.5ºC km^{-1}. The Summer peak occurred on JD 228 (August 16, 2010) at the Lower Station with a temperature of 11.8ºC, after which both the daily minimum and maximum temperatures generally declined. Spikes in temperature occurred around JD 273 (2010), JD 328 (2010), and JD 1 (2011), before the lowest temperature at all stations occurred on JD 15 2011 (-40.0ºC at the Middle Station, -36.1 ºC at the South Arm Station, -34.7ºC at the Lower Station).

Additional temperature data was provided by the GSC, from the permanent weather station located on the nunatak near the Upper Station site (Figure 3.2). The air temperatures at this

location closely follow the patterns found on the glacier surface for the period where the datasets overlap, sharing the lowest temperature date and value, on JD 15 2011 (-32.8ºC) (Figure 4.9b).

During most of the year, the temperature patterns at all three glacier stations followed very similar trends. However, after JD 21 2011 the Lower station is substantially colder than the others, maintaining temperatures between -3.7ºC and -29.1ºC. The Middle and South Arm stations mimic the variability present at the Lower station, but temperatures are warmer on average and stay above -18.6ºC. This is likely caused by winter temperature inversions, which trap cold air in the valley bottom at the lowest elevations of the glacier. After JD 72, the agreement between stations resumes, again with the Lower Station maintaining slightly higher temperatures, between 4ºC and 6ºC greater than both the Middle and South Arm stations.

4.3.2 Surface changes

Snow depth sounder data was collected at the Upper Station between JD 156 and JD 263 2010 and between JD 151 and JD 223 2011, with a period between JD 263 2010 and JD 151 2011 where the sensor did not operate (Figure 4.9a). Data at the South Arm Station was collected between JD 187 and JD 241 2010 and between JD 263 2010 and JD 197 2011, with ~20 days of missing data due to stormy weather. A large, rapid increase in surface height on JD 241 2010 corresponds to a date when the sensor mounting poles were redrilled (to prevent them falling out due to surface melt). There is good agreement between the melt patterns where the datasets from the South Arm and the Upper Station overlap. During the Summer regime, melt occurs at a near-constant rate of 5.6 cm day^{-1} at the Upper station and 5.7 cm day^{-1} at the South Arm Station. Melt slows at the Upper Station around JD 230 2010, which corresponds well to decreases in temperature to near freezing around the same time. The sensor stopped operation on JD 263 (2010), resuming with the relocation that occurred on JD 151 (2011), when melt appears to peak. The Upper Station dataset resumes on JD 151 2011 and a melt rate of 5.24 cm day^{-1} is established by JD 161.

Five snow fall events can be identified at the South Arm Station in 2010/2011: JD 270 (23.6 cm), JD 282 (19.8 cm), JD 306 (30.4 cm), JD 30 (36.7cm) and JD 42 (21.1 cm). At the South Arm Station, there is also variation in surface height throughout fall 2010 and early winter 2011 (likely due to snow pack settling and wind redistribution), until JD 41 2011 when the snow pack appears to stabilize. Surface melt begins again around JD 135 2011, with an overall rate of 5.27 cm day^{-1}. These patterns indicate that the main annual snow accumulation period is the Fall, while snow pack is maintained with little change during the Winter.

Figure 4.1 dGPS derived horizontal velocity (solid line) and vertical motion (dashed line) for the Lower, Middle and Upper stations for a) 2009-2010 and b) 2010-2011.

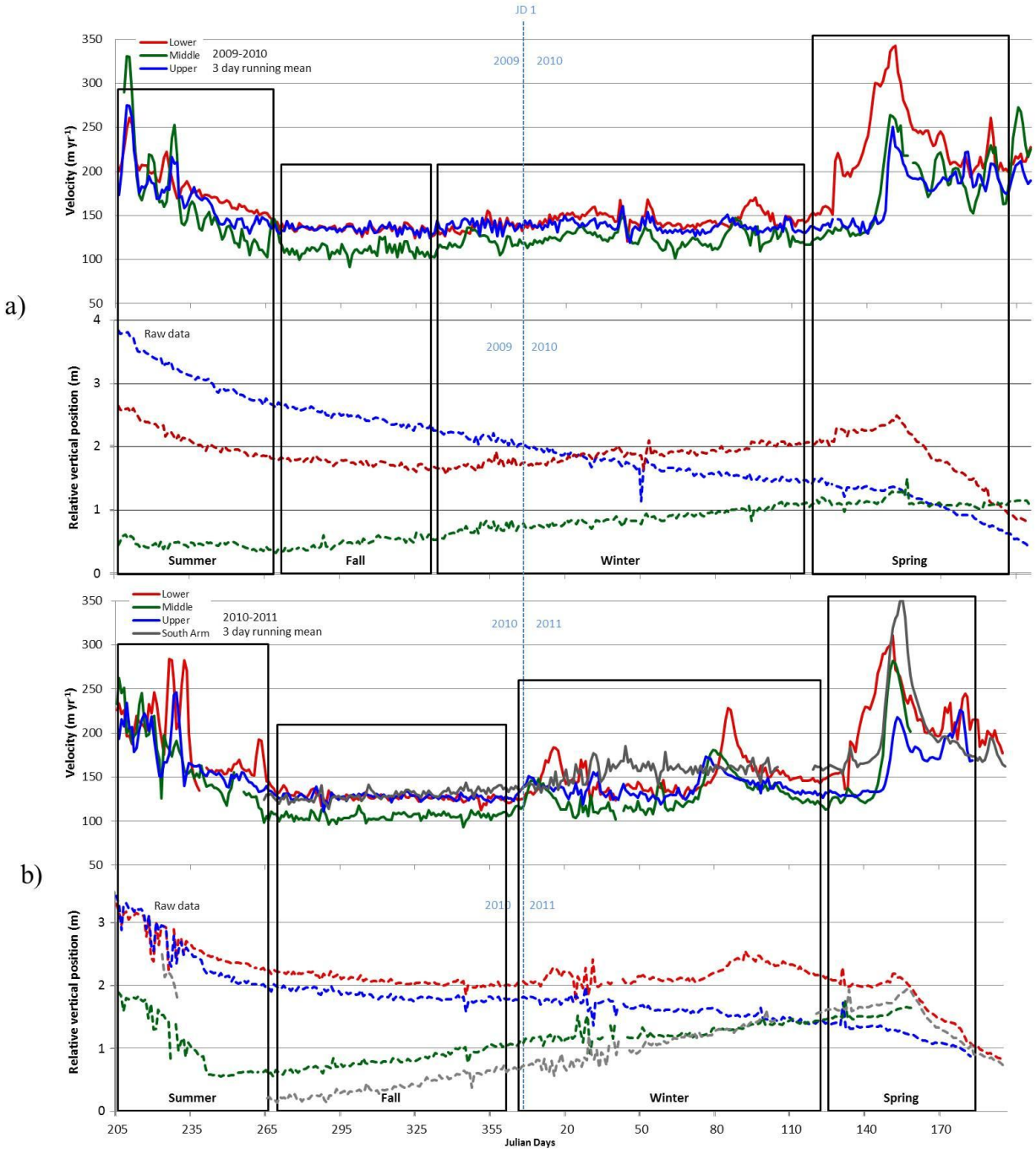

Figure 4.2 Detailed velocity patterns during the a) 2009-2010 and b) 2010-2011 Winter Regimes (as identified in Figure 4.1 and Table 4.1). Horizontal velocities marked by solid lines (3 day running mean) and light-coloured lines (daily mean). Surface heights marked by dashed lines. Individual velocity events are identified by boxes, with peaks for each event connected by dotted lines.

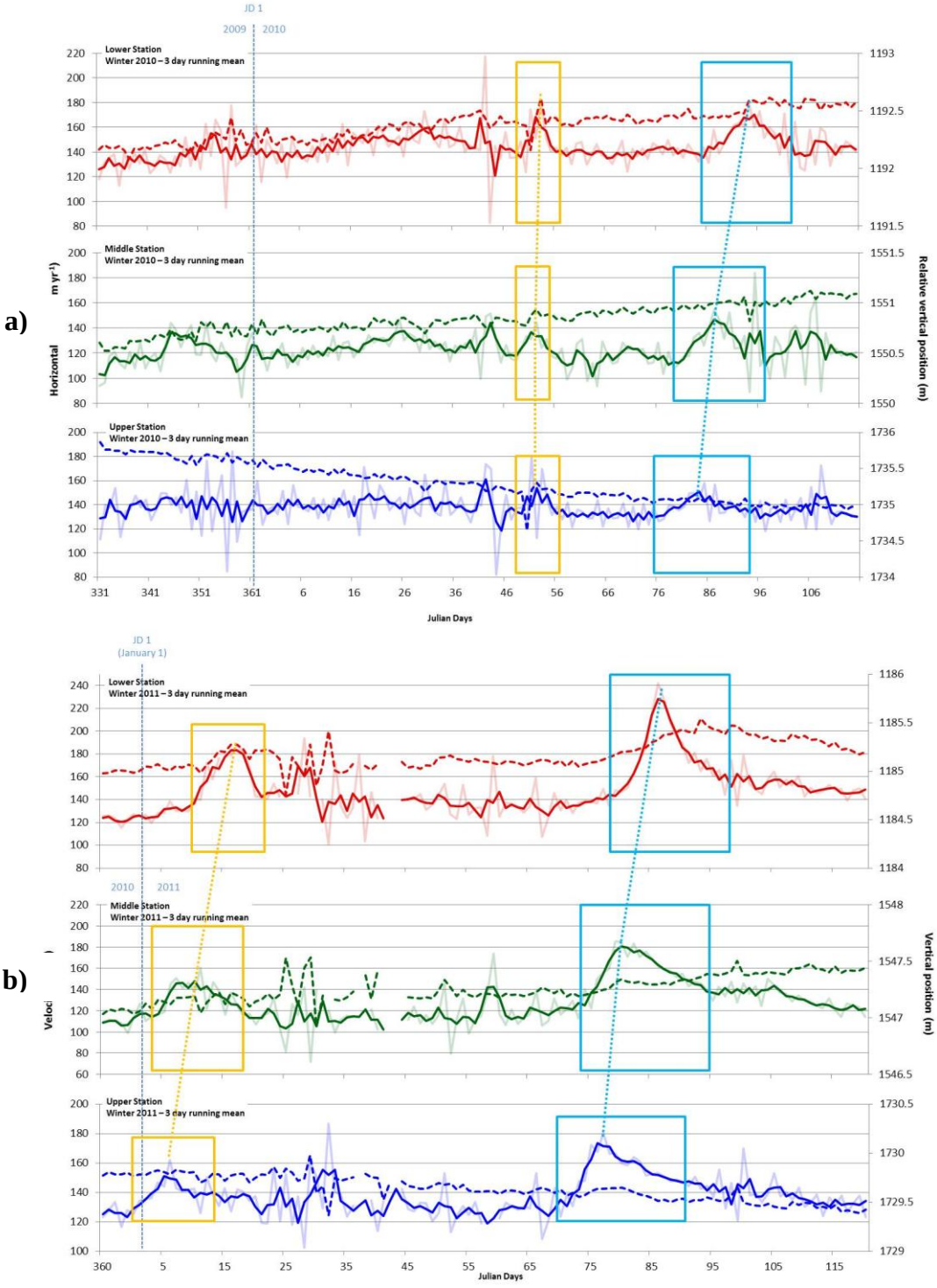

Figure 4.3 Periods of dGPS-derived horizontal velocity data (3 day running mean) that overlap with the Radarsat-2 image pairs used for speckle tracking, ultra-fine (red) and fine (blue) beam modes.

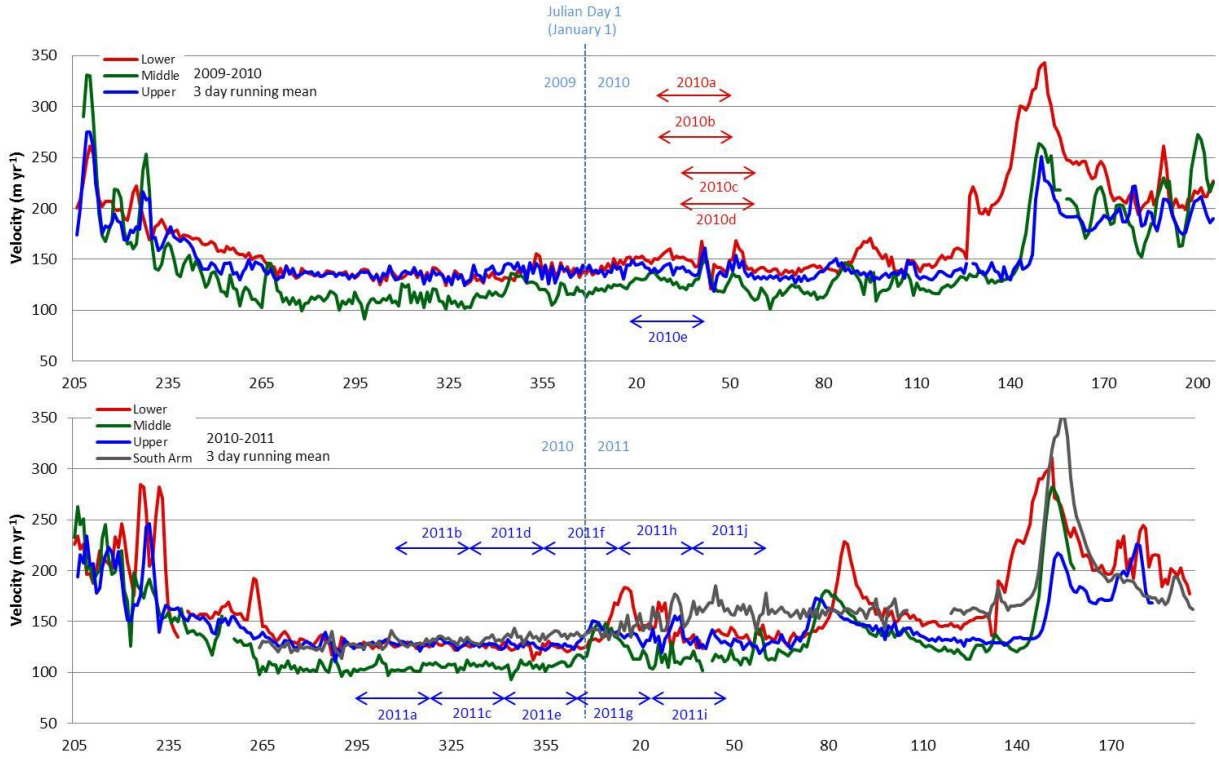

Figure 4.4 The steps used to validate and filter speckle tracking results derived from an example fine beam image pair from Dec. 7 and Dec. 31, 2010: a) raw vector results; b) results limited to the Kaskawulsh Glacier and surrounding tributaries based on rock outlines from Barrand and Sharp (2010); c) remaining vectors after erroneous matches have been removed based on validation criteria; d) Inverse Distance Weighted (IDW) interpolation of filtered results. A comparison of areas with different coherence is made in b): i) area where coherence is lost; ii) an area where coherence is maintained. The locations of validation sites 1-4 (areas of zero motion) are identified in d) by red triangles.

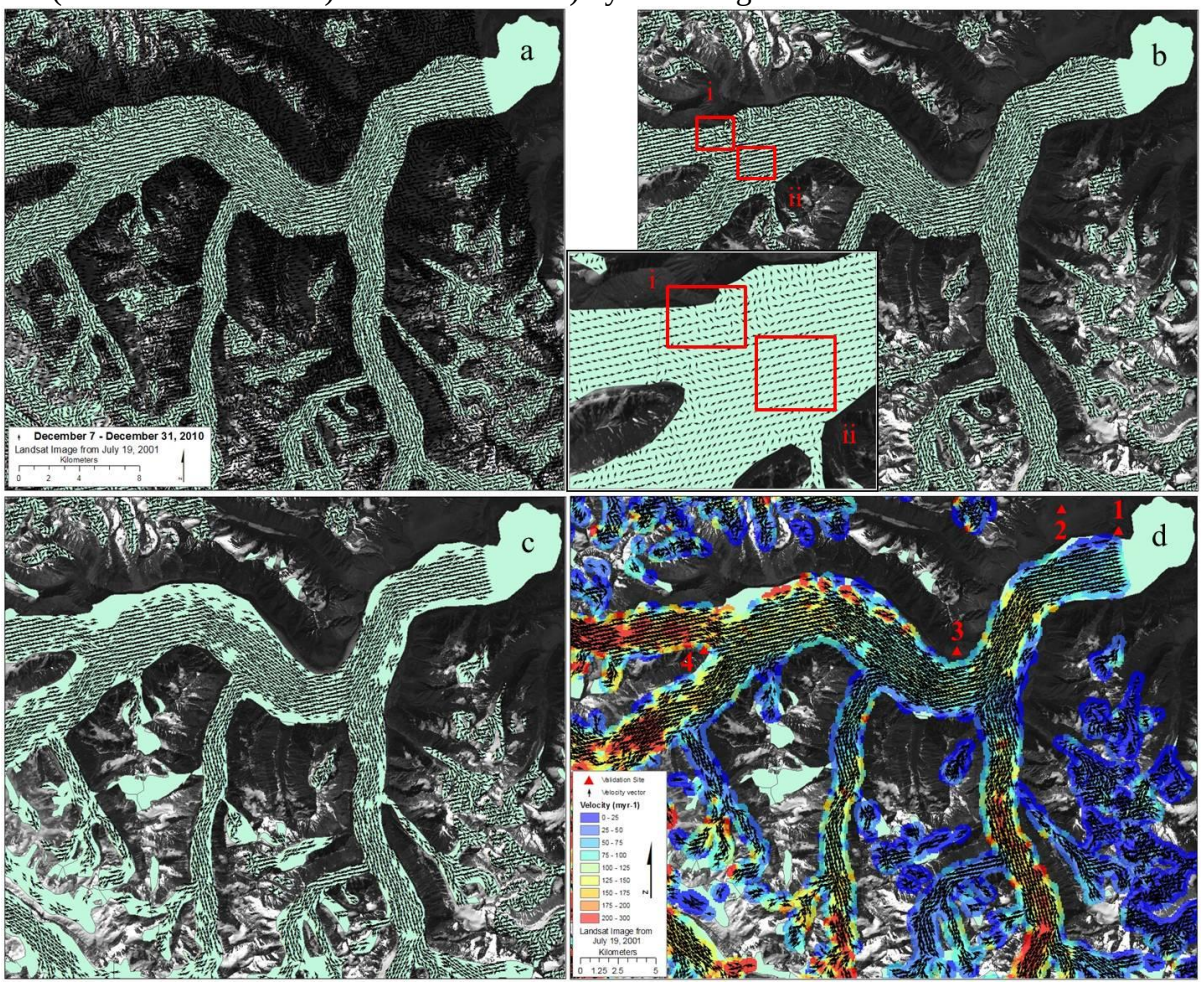

Figure 4.5 Velocity maps produced by speckle tracking using ultra-fine imagery from pairs 2010a (Jan 26 – Feb 19), 2010b (Jan 26 – Feb 19), 2010c (Feb 2 – Feb 26), and 2010d (Feb 2 – Feb 26).

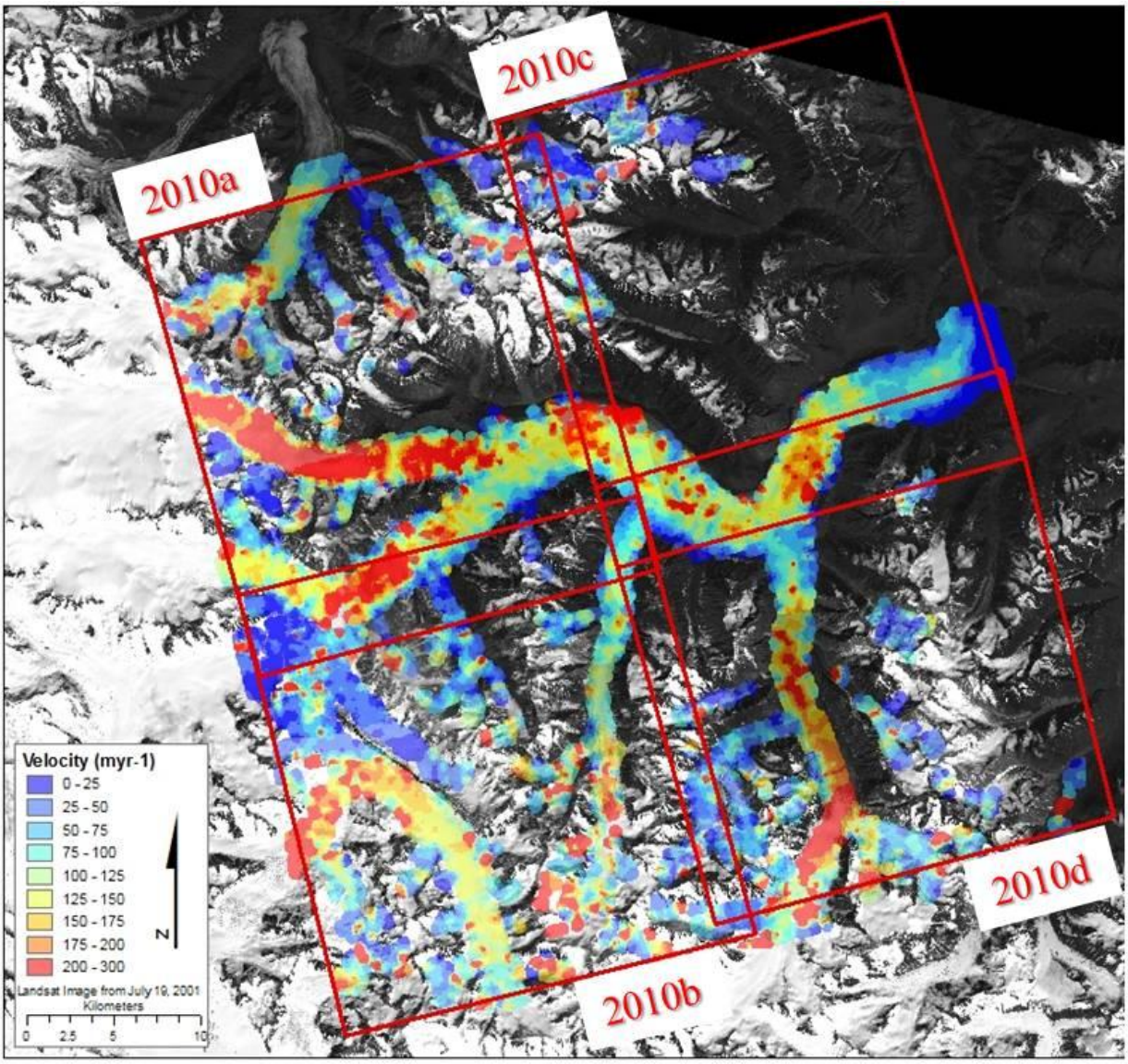

Figure 4.6 Velocity map produced by speckle tracking using fine beam imagery from pair 2010e (Jan 18 – Feb 11).

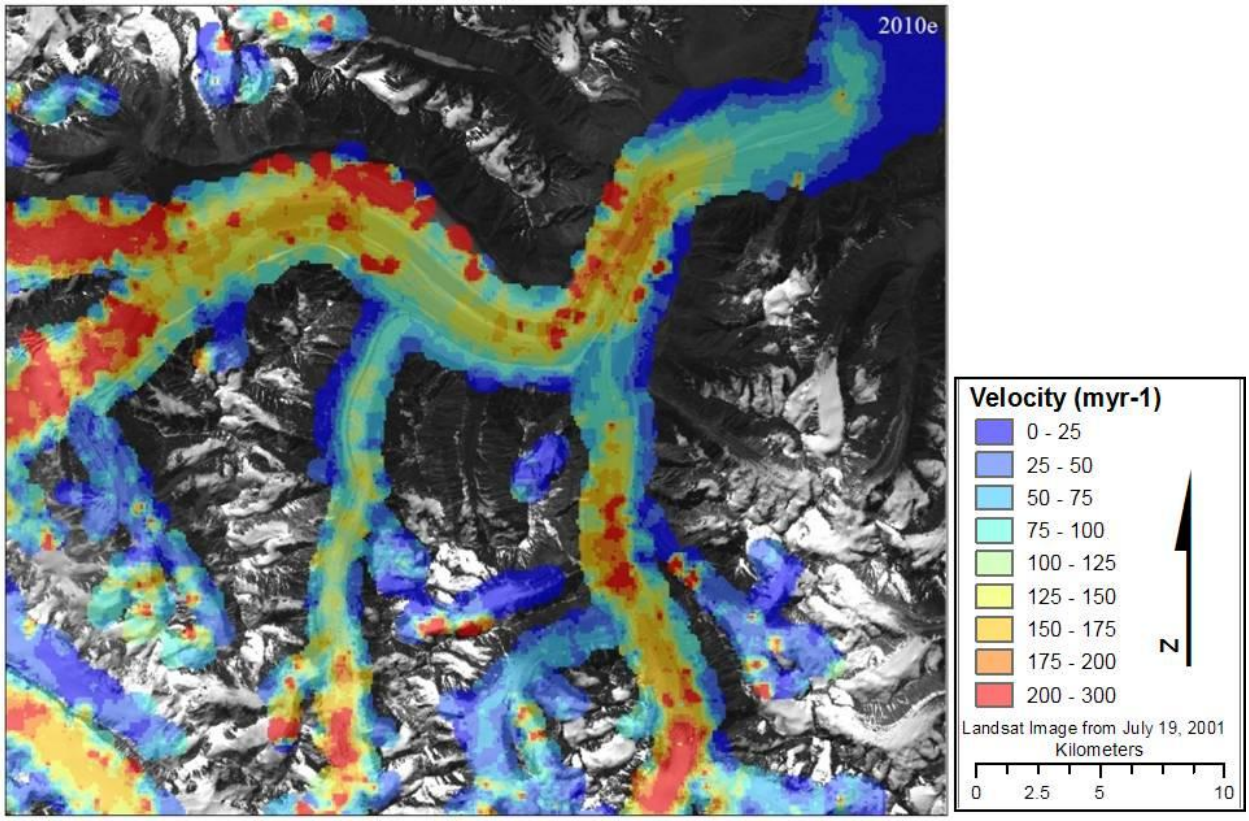

Figure 4.7 Velocity maps produced from Radarsat-2 fine beam imagery for the 2011 Winter Regime (JD 265 – JD 3): a) 2011a, b) 2011b, c) 2011c, d) 2011d, e) 2011e, f) 2011f.

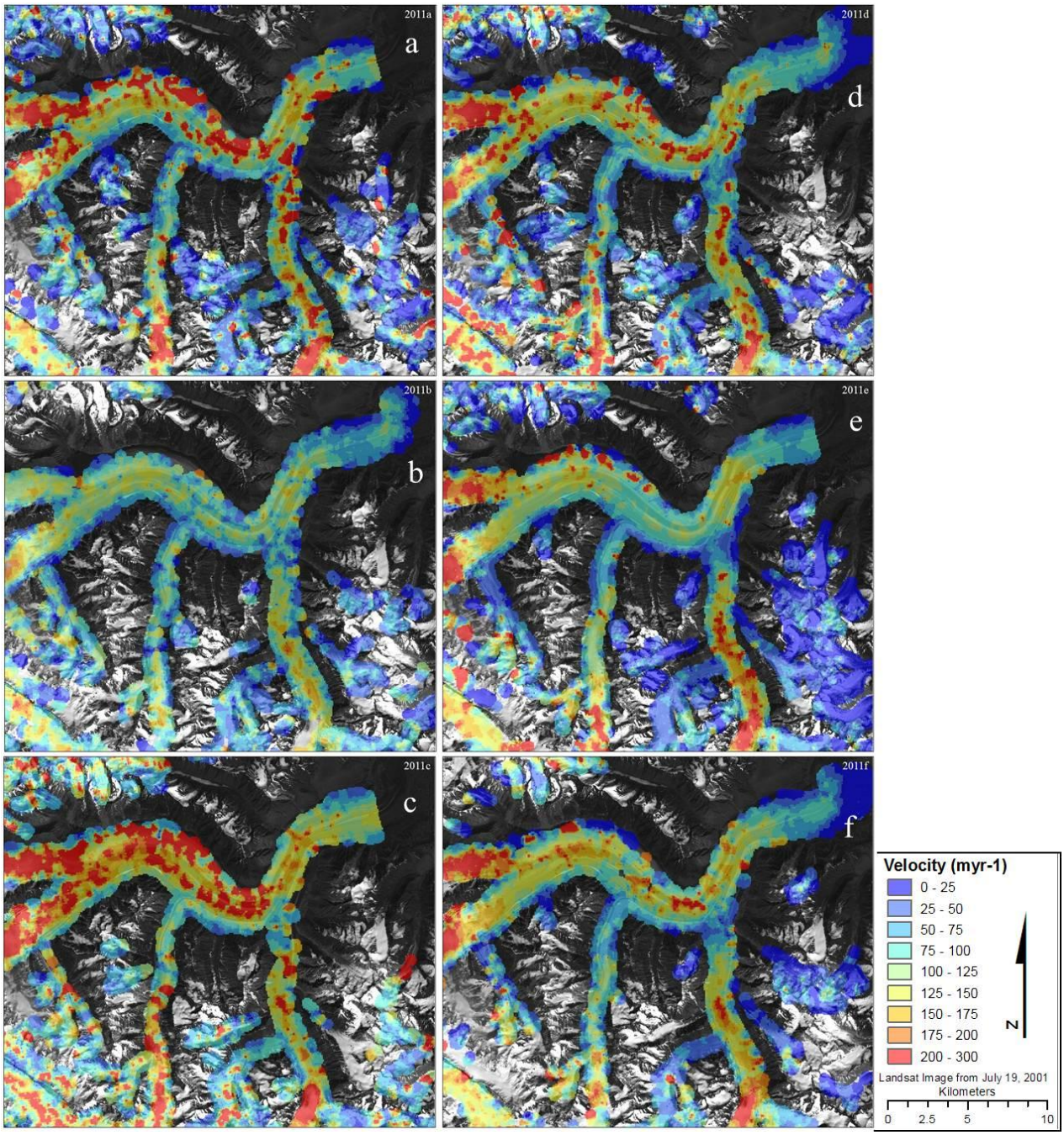

Figure 4.8 Velocity maps produced using Radarsat-2 fine beam imagery for the 2011 Spring Regime (JD3 – JD 146) for images: a) 2011g, b) 2011h, c) 2011i, d) 2011j.

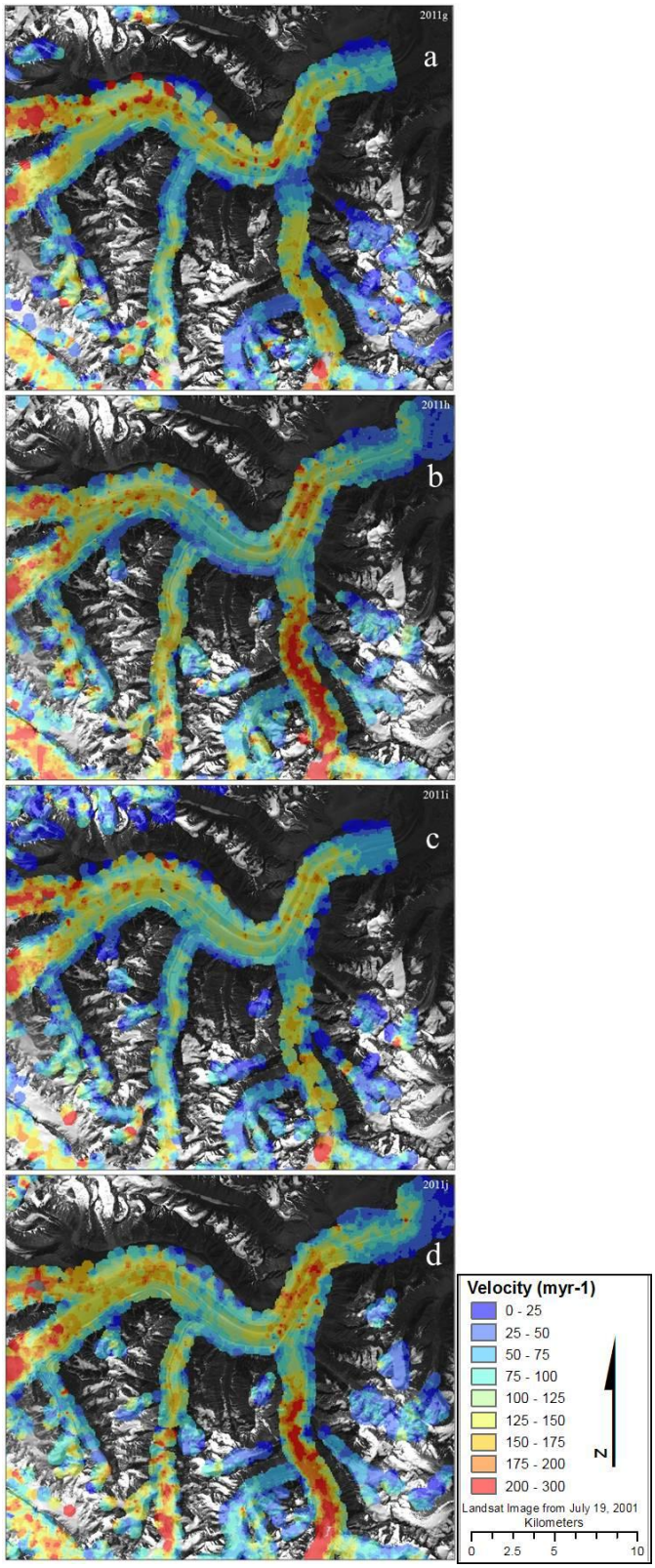

Figure 4.9 For 2010-2011, a comparison of: (a) changes in surface height (distance between sensor and glacier surface) at the Upper and South Arm stations; (b) temperature data from the Lower, Middle and Upper stations and the GSC automated weather station; (c) dGPS data from all stations.

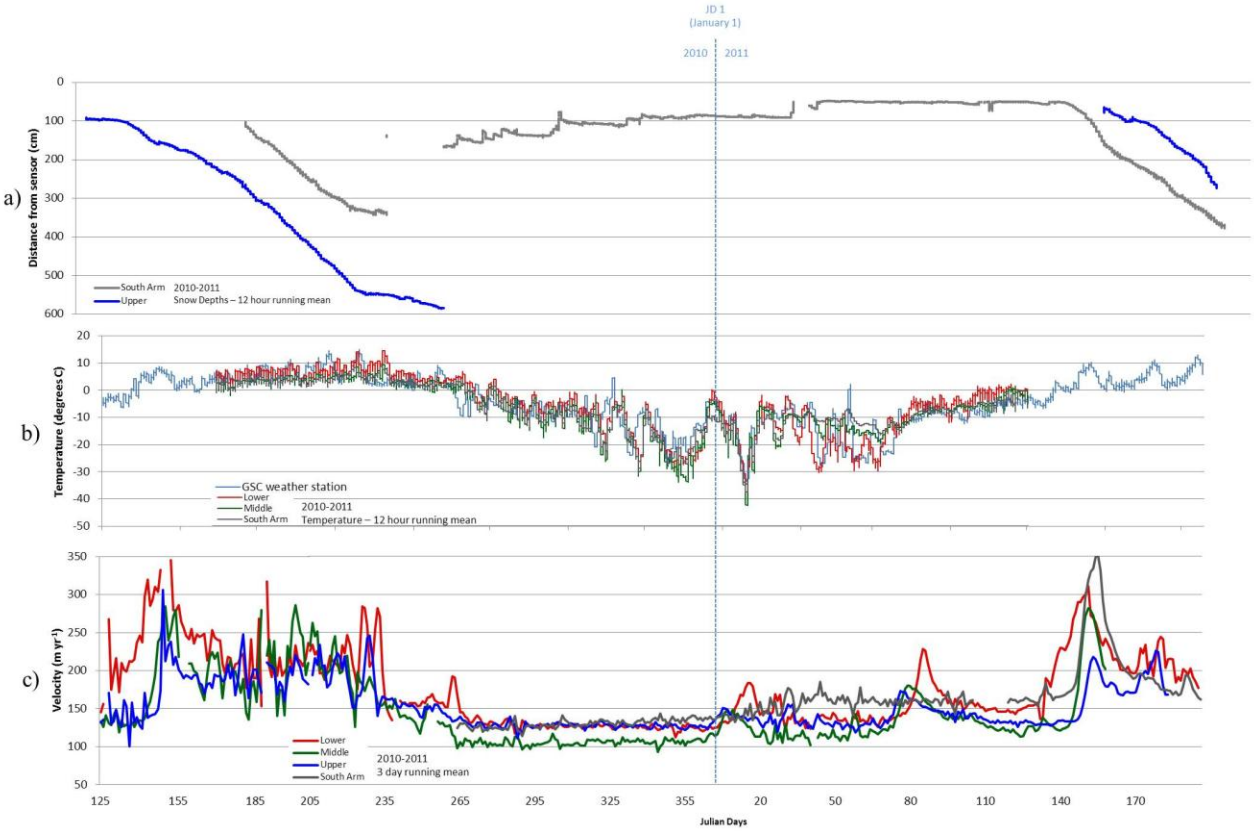

Table 4.1 Seasonal horizontal velocity averages calculated from dGPS data collected at three stations along the centerline of the Kaskawulsh Glacier and one on the South Arm tributary. Dates are reported in Julian Days (JD) and velocities in m a^{-1}.

Season	Start (JD)	End (JD)	Station velocity			
			Lower	Middle	Upper	South Arm
			60°46.140'N 138°45.957'W	**60°45.127'N 138°57.938'W**	**60°43.619'N 138°07.986'W**	**60°30.031'N 138°48.029'W**
Year 1 2009-2010 (JD 205-205)						
Summer	205	267	182.5	166.3	171.2	-
Fall	269	330	134.9	110.7	134.8	-
Winter	331	115	143.7	123.1	137.8	-
Spring	116	205	223.6	181.4	176.4	-
Annual mean			**171.2**	**145.4**	**155.0**	
Year 2 2010-2011 (JD 205-196)						
Summer	205	264	195.0	170.9	172.3	164.1
Fall	265	359	128.3	105.3	127.7	129.8
Winter	360	120	148.4	129.0	138.4	155.2
Spring	121	196	209.2*	162.6**	164.7***	198.8
Annual mean			**170.2**	**142.0**	**150.8**	**162.0**

*The Lower Station dataset runs from JD 121-195, 2011
**The Middle Station dataset runs from JD 121-157, 2011
***The Upper Station dataset runs from JD 121-182, 2011

Table 4.2 Velocities for winter speed-up events measured by dGPS (m a^{-1}) and identified in Figures 4.2.

Winter Peaks	**Lower Station**		**Middle Station**			**Upper Station**		
2009-2010 Year 1 (JD 205-205)	Peak JD	Peak velocity (m a^{-1})	Peak JD	Peak velocity (m a-1)	Speed of propagation from Middle to Lower (m day^{-1})	Peak JD	Peak velocity (m a^{-1})	Speed of propagation from Upper to Middle (m day^{-1})
	53	179.4	52	144.5	16380	51	180.3	10690
	94	178.7	87	154.6	2340	85	158.0	5345
Annual mean	**171.2**		**145.4**			**155.0**		
2010-2011 Year 2 (JD 205- 156)	17	188.0	11	160.7	2730	6	162.1	2138
	86	242.2	79	185.2	2340	77	180.4	5345
Annual mean	**170.2**		**142.0**			**150.8**		

Table 4.3 Comparison between horizontal velocities derived from speckle tracking of Radarsat-2 imagery and simultaneous dGPS measurements for all image pairs used in this study. The four closest speckle-tracking values to the dGPS station locations, within one pixel of the site, were used to provide the speckle tracking velocities. Where no value was within this proximity, no value was calculated. All velocities in m a^{-1}.

	Master Image	Slave Image	Speckle tracking Lower	dGPS Lower	% difference	Speckle tracking Middle	dGPS Middle	% difference	Speckle tracking Upper	dGPS Upper	% difference	Speckle tracking S. Arm	dGPS South Arm	% difference
Ultra Fine Beam														
2010a	Jan 26, 2010	Feb 19, 2010	-	-	-	124.0	131.9	6.0	102.8	123.6	16.8	-	-	-
2010b	Jan 26, 2010	Feb 19, 2010	-	-	-	122.2	131.9	7.3	101.2	123.6	18.1	-	-	-
2010c	Feb 2, 2010	Feb 26, 2010	141.7	140.4	-0.8	99.0	123.5	19.8	-	-	-	-	-	-
2010d	Feb 2, 2010	Feb 26, 2010	147.3	140.4	-4.9	116.2	123.5	5.8	-	-	-	-	-	-
Average Velocity			**144.5**	**135.2**	**-2.9**	**115.4**	**127.7**	**10.7**	**102.0**	**123.6**	**17.5**	**-**	**-**	**-**
Fine Beam														
2010e	Jan 18, 2010	Feb 11. 2010	167.8	182.2	0.7	136.4	136.4	0	132.2	172.3	23.2	-	-	-
2011a	Oct 20, 2010	Nov 13, 2010	150.1	128.0	-15.3	119.2	96.8	-23.1	200.4	128.0	-56.6	246.7	125.5	-96.6
2011b	Nov 2, 2010	Nov 26, 2010	110.1	130.1	14.5	85.6	112.9	24.2	109.5	130.2	15.9	-	132.7	-
2011c	Nov 13, 2010	Dec 7, 2010	163.8	127.9	-28.0	150.3	102.9	-2.3	151.4	126.2	-20.0	349.7	128.0	-173.3
2011d	Nov 26, 2010	Dec 20, 2010	192.0	130.1	-47.6	135.7	121.8	-11.4	166.4	120.8	-37.7	222.1	124.5	-78.4
2011e	Dec 7, 2010	Dec 31, 2010	124.9	123.0	-1.5	107.1	107.2	0.0	125.2	119.1	-5.1	134.4	135.0	0.4
2011f	Dec 20, 2010	Jan 13, 2011	130.5	145.9	10.6	150.5	135.7	-10.9	127.6	126.0	-1.2	118.4	141.6	16.4
2011g	Dec 31, 2010	Jan 24, 2010	161.1	134.7	-19.6	121.6	107.6	-13.0	125.9	122.6	-2.7	126.8	141.7	11.2
2011h	Jan 13, 2011	Feb 6, 2011	92.3	168.6	45.2	107.1	147.0	27.1	155.4	139.0	-11.8	189.6	154.1	-0.8
2011i	Jan 24, 2011	Feb 17, 2011	123.2	136.8	9.9	100.8	108.8	7.4	147.3	126.4	-16.6	151.5	151.6	33.5
2011j	Feb 6, 2011	Mar 2, 2011	177.7	158.3	-12.3	131.0	106.7	-22.7	147.2	132.9	-10.7	187.2	159.8	-17.2
Average Velocity			**144.9**	**142.4**	**-1.7**	**118.2**	**116.7**	**1.3**	**144.4**	**131.2**	**10.0**	**182.3**	**139.4**	**30.7**
Average % difference			**8.2**											

Table 4.4 A comparison of orientations calculated by speckle tracking and those recorded by dGPS over simultaneous periods. The four closest speckle-tracking values to the dGPS station locations, within one pixel of the site, were averaged to provide the shown value. Where no value was within this proximity, no value was calculated. All orientations are presented in degrees.

	Master Image	Slave Image	Speckle Tracking Lower	dGPS Lower	Difference between dGPS and ST	Speckle Tracking Middle	dGPS Middle	Difference between dGPS and ST	Speckle Tracking Upper	dGPS Upper	Difference between dGPS and ST	Speckle Tracking South Arm	dGPS South Arm	Difference between dGPS and ST
Ultra Fine Beam														
2010a	Jan 26, 2010	Feb 19, 2010	-	42.6	-	124.4	147.6	23.2	48.9	45.5	-3.4	-	-	-
2010b	Jan 26, 2010	Feb 19, 2010	-	42.6	-	125.7	147.6	21.9	41.5	45.5	4.1	-	-	-
2010c	Feb 2, 2010	Feb 26, 2010	40.6	41.3	0.7	134.4	120.0	-14.4	-	44.8	-	-	-	-
2010d	Feb 2, 2010	Feb 26, 2010	46.8	41.3	-5.5	131.1	120.0	-11.1	-	44.8	-	-	-	-
Average speckle tracking orientation			**42.9**	**42.0**	**-1.7**	**128.9**	**133.8**	**4.9**	**45.2**	**45.2**	**-0.0**	-	-	-
Fine Beam														
2010e	Jan 18, 2010	Feb 11. 2010	43.6	50.3	6.7	149.6	147.1	-2.5	46.6	50.4	3.8	-	-	-
2011a	Oct 20, 2010	Nov 13, 2010	42.8	52.8	10.0	125.7	124.0	0.12	42.2	43.1	0.9	24.3	8.4	-15.9
2011b	Nov 2, 2010	Nov 26, 2010	47.9	52.5	4.6	140.4	123.1	-17.3	51.2	46.2	-5.0	-	10.9	-
2011c	Nov 13, 2010	Dec 7, 2010	49.1	52.3	3.2	123.2	123.8	0.13	57.6	42.4	-15.2	-	9.5	-
2011d	Nov 26, 2010	Dec 20, 2010	45.1	54.0	8.9	131.9	124.8	-7.1	51.2	46.6	-4.6	-	8.0	-
2011e	Dec 7, 2010	Dec 31, 2010	40.0	52.1	12.1	124.6	123.5	-1.1	49.6	44.9	-4.7	12.2	8.0	-4.2
2011f	Dec 20, 2010	Jan 13, 2011	52.9	53.7	0.8	130.6	123.4	-7.1	51.5	47.0	-4.5	12.0	11.5	-0.5
2011g	Dec 31, 2010	Jan 24, 2010	42.4	50.5	8.1	125.3	123.3	-1.9	45.0	44.5	-0.5	11.4	9.5	-1.9
2011h	Jan 13, 2011	Feb 6, 2011	45.6	43.2	-2.4	113.4	127.3	13.9	39.4	44.7	5.3	6.8	19.8	13.0
2011i	Jan 24, 2011	Feb 17, 2011	45.8	51.4	5.7	124.5	128.2	3.7	47.5	44.2	-3.3	10.3	8.9	-1.4
2011j	Feb 6, 2011	Mar 2, 2011	42.2	45.8	3.6	114.7	129.7	15.0	44.3	43.4	-0.9	18.8	10.4	-8.4
Average orientation			**45.2**	**50.8**	**5.6**	**127.6**	**127.0**	**-0.6**	**47.8**	**45.2**	**-2.6**	**13.7**	**10.7**	**-2.8**
Total Difference			**-0.1**											

Table 4.5 Speckle-tracking derived velocities for all image pairs over areas of known zero motion. All values are in m a^{-1}.

	Master Image	Slave Image	Site 1 (terminus)	Site 2 (meadow)	Site 3 (corner)	Site 4 (nunatak)	**Average Velocity**
	Ultra Fine Beam						
2010a	Jan 26, 2010	Feb 19, 2010	-	-	-	10.4	**10.4**
2010b	Jan 26, 2010	Feb 19, 2010	-	-	-	7.0	**7.0**
2010c	Feb 2, 2010	Feb 26, 2010	4.2	8.6	13.9	-	**8.9**
2010d	Feb 2, 2010	Feb 26, 2010	11.9	23.1	23.6	-	**19.5**
Average velocity from speckle tracking			**8.1**	**15.9**	**18.75**	**8.7**	
Fine Beam							
2010e	Jan 18, 2010	Feb 11. 2010	6.9	7.4	10.8	10.4	**8.9**
2011a	Oct 20, 2010	Nov 13, 2010	-	15.0	8.6	12.5	**9.0**
2011b	Nov 2, 2010	Nov 26, 2010	21.9	0.0	6.4	27.6	**13.9**
2011c	Nov 13, 2010	Dec 7, 2010	41.7	60.9	50.2	39.4	**48.1**
2011d	Nov 26, 2010	Dec 20, 2010	11.9	36.4	35.1	28.7	**28.0**
2011e	Dec 7, 2010	Dec 31, 2010	10.9	2.6	15.3	4.9	**8.4**
2011f	Dec 20, 2010	Jan 13, 2011	12.4	15.4	14.0	12.5	**13.6**
2011g	Dec 31, 2010	Jan 24, 2010	16.6	8.5	9.3	7.7	**10.5**
2011h	Jan 13, 2011	Feb 6, 2011	28.9	0.0	43.7	34.9	**14.9**
2011i	Jan 24, 2011	Feb 17, 2011	13.2	11.6	6.2	12.9	**10.9**
2011j	Feb 6, 2011	Mar 2, 2011	24.8	0.0	29.4	21.3	**18.8**
Average velocity from speckle tracking			**17.2**	**28.7**	**20.8**	**19.3**	
Average Difference			**15.3**				

Chapter 5 Discussion and conclusions

This chapter outlines the implications of the results presented in Chapter 4. First, there is a discussion of the Radarsat-2 velocity maps as prioritized by validation requirements and how well they represent the different seasonal velocity regimes. Then, a broader look at the dGPS results and their relationship to meteorological data is presented to provide a context for the seasonal velocity variations. Finally, the winter speed-up events are examined more closely. From this examination, conclusions about the state of the subglacial drainage system and effective pressure are placed into the wider context of glacier dynamics through comparison with previous studies from other regions.

Based on the validation requirements outlined in Chapters 3 and 4, a subset of three velocity maps derived from speckle tracking were chosen which minimize potential errors and are therefore believed to best represent the velocity structure of the Kaskawulsh Glacier. Image pairs 2010e (January 18 – February 11, 2010; Figure 5.1), 2011e (December 7 – December 31, 2011; Figure 5.2) and 2011i (January 24 – February 17, 2011; Figure 5.3) best fulfilled these requirements. Image pair 2010e was acquired in the Winter Regime of 2010 and had an average 2.0% difference in horizontal velocity and 6.0º difference in orientation between dGPS and speckle tracking results. Image pair 2011e was acquired in the Fall Regime of 2010 and had an average 1.8% difference in velocity and -1.6º difference in orientation, while image pair 2011i was acquired in the Winter Regime of 2011 and had an average 2.3% difference in velocity and 8.6º difference in orientation. These maps also showed the least error in the areas of known zero motion (Figure 4.4), with average apparent motion in these locations of 12 m a^{-1} for 2010e, 7 m a^{-1} for 2011e and 10 m a^{-1} for 2011i. These maps are also sufficiently dispersed throughout the fall and winter regimes to provide some insight into the transitions between them.

5.1 Flow unit variations

Plots of horizontal motion along the centerline of each flow unit, as identified in Figure 5.4, allow for comparison between the velocity maps (Figure 5.5). A general structure for each flow unit can be identified based on these plots which can be partially attributed to localized factors such as adjacent topography and number and size of tributaries. The North Arm

shows an initial increase of ~100 m a^{-1} within 3.8 km of the terminus, followed by high variability into the upper ablation area. The Central Arm sees an increase to ~100 m a^{-1} in the first 7 km from the terminus, which is maintained for another 28.8 km up-glacier where, in all images, there is another increase to 200 m a^{-1} or more. The Stairway Glacier exhibits consistent velocities around 100 m a^{-1}, until ~9.5 km from its juncture with the Central Arm. From there, velocities fluctuate while still increasing into the accumulation area, where there is also an increase in the number and size of tributaries. The South Arm sees a gradual increase from the terminus until 11.5 km up-glacier, where there is a drop of ~100 m a^{-1} in all images to a low of 78.8 m a^{-1} in 2010e, 58.6 m a^{-1} in 2011e, and 71.6 m a^{-1} in 2011i. This ~3.5 km wide area appears to be an area of relatively slowly moving ice where the South Arm meets the main Kaskawulsh Glacier (here comprised of the North and Central arms and the Stairway Glacier). Upglacier of here velocities remain variable but elevated well into the accumulation area and peak where a large tributary joins 28.2 km from the terminus. Average velocities for each flow unit reveal that overall velocities vary little between images (2010e, 155.9 m a^{-1}; 2011e, 142.6 m a^{-1}; 2011i, 121.7 m a^{-1}). This indicates that the overall velocity patterns are similar from year to year, but there is a lot of variability within each season. The 24-day cycle is too broad of a time period to capture the subtle variations during the Winter Regime (most notably the speed-up events which lasted at most 10 days).

5.2 Seasonal regimes

The seasonal variations in horizontal velocity and vertical position presented in Chapter 4 provide evidence that the Kaskawulsh Glacier undergoes distinct seasonal regimes in motion, similar to those previously described for other temperate glaciers such as Findelengletscher, Switzerland (Iken and Truffer, 1997), Haut Glacier d'Arolla, Switzerland (Harbor et al., 1997; Mair et al., 2002) and the polythermal glacier Storglaciären, Sweden (Hock and Hooke, 1993). These studies have determined that transitions between channelized and distributed subglacial drainage systems, as described in Section 2.2.2, produce variations in water pressure that are manifested as variations in surface elevation (uplift and settling) and horizontal velocity. Using the idea of water pressure as a control on surface velocity, one can infer the annual development of the subglacial drainage system of the Kaskawulsh Glacier

based on the dGPS, speckle tracking and supplemental results presented here. In doing so there are two factors that must be considered for each seasonal velocity regime:

1) The state of the subglacial drainage system (Section 2.2) is the main mechanism that controls the transportation of subglacial water and one of the main controls on basal water pressure (the other being meltwater input). The distributed system drains very inefficiently and there is an increased retention of water because of this, in pockets created by subglacial topography or relic channels that are cut off from the main drainage system. In contrast, the channelized system efficiently evacuates basal water through the interconnection of branching channels that culminate in a proglacial stream.
2) The value of effective pressure N (the difference between ice overburden pressure and water pressure as shown in Equation 2, Section 2.3). Ice overburden pressure P_i is assumed to remain essentially constant over the time periods addressed here because ice thicknesses vary little. Variations in basal water pressure P_w, however, can occur on short timescales and therefore cause rapid variations in effective pressure. This will influence the proportion of motion due to sliding because of the potential for basal ice decoupling from the bed (Paterson, 1994).

5.2.1 Spring regime

The main characteristic of the Spring Regime is the spike in both horizontal velocity and uplift visible in the dGPS data at all stations in both 2010 and 2011 (Figure 4.1). The Spring speed-up occurred at a similar time in both years (JD 145-150 in 2010 vs. JD 150-154 in 2011), and initiated at the Lower Station first, progressing up-glacier over the subsequent 2 – 7 days. Studies of water pressure in boreholes on other glaciers (e.g., Mair et al. 2003; Kamb, 1985) indicate that rapid increases in surface velocity typically reflect a reduction in effective pressure. This occurs as basal water pressure exceeds separation pressure, decoupling the glacier from its bed and increasing the amount of motion due to basal sliding. In rare instances, the effective pressure can even become negative for short periods, meaning that the glacier can essentially float off its bed for short periods.

Melt onset occurs at the Lower Station first on JD 112 (2011), related to day-time temperatures consistently above freezing, likely causing a rapid increase in basal water pressure through the input of surface meltwater through features such as moulins. Later, on JD 126 (2011), melt onset occurs at the Middle Station, which also sees the next peak in velocity, which would indicate the expansion of the subglacial drainage system up-glacier. The snow sensor measurements at the Upper Station show the onset of a lowering of the snowpack by JD 151 (2011), indicating the onset of surface melt there. The presence of a snowpack through the early melt season produces a small lag between surface melt and the introduction of meltwater into the englacial and subglacial drainage systems through percolation. Exposed ice, however, introduces meltwater directly into the englacial and subglacial systems with little-to-no lag time (Hubbard et al., 1995). These conditions, according to Paterson (1994), lead to the dominance of basal sliding in glacier motion. This behaviour is similar to that reported on Storglaciären, Sweden (Hock and Hooke, 1993) whose spring peak occurred around JD 207 in 1989, and Haut Glacier d'Arolla, Switzerland (Mair et al. 2002; Mair et al., 2003), whose spring peak in velocity occurred around JD 182 in 1995, JD 157 in 1998, and JD 181 in 1999, generally corresponding with peaks in proglacial discharge. Nienow et al. (1998) described the progression through the peak melt season on the Haut Glacier d'Arolla based on the measurement of the time needed for rhodamine dye injected into a series of moulins to travel through the subglacial drainage system (Figure 2.3). The up-glacier progression of surface melt was matched with the switch from a distributed subglacial drainage system (which had high basal water pressures, resulting in the initial spring peak in velocity and an extended period of rhodamine detected in the proglacial stream), to the efficient drainage of a channelized system, which was detected due to a very quick spike in rhodamine dye return (inferring lower basal water pressures and a coincident reduction in velocities from their spring peak)

At the Kaskawulsh Glacier the spring velocity peak follows a few days after surface temperatures rising and remaining above 0°C in 2011 (JD 112 at the Lower Station, JD 126 at the Middle Station, and after JD 133 at the South Arm Station) and the reduction of snowpack thickness as shown by the snow depth sounder at the Upper Station (JD 135) and on the South Arm (JD 135). A peak in uplift is most apparent in the Lower Station in both

2010 (JD 149) and 2011 (JD 152), and the Middle Station in 2011 (JD 158). This suggests high subglacial water pressures at this time, which are likely caused by surface meltwater input to the glacier bed that overwhelmed the underdeveloped subglacial distributed system formed during the previous winter. After this peak, there is a substantial drop in both velocity and surface elevation over the course of the next month (42 days at the Lower Station, 6 days at the Middle Station and 10 days at the Upper Station) which suggests that the subglacial drainage system transitions to a channelized system over this period, and effective pressure becomes more positive. Subglacial basal water pressure typically remains lower than separation pressure in a channelized drainage system as the volume of water is within its capacity for drainage. With sufficient water volume in the subglacial system, some support for channel walls is provided and larger tunnels near the terminus can expand through lateral melting, although this appears to have little influence on surface velocity (Paterson, 1994; Benn and Evans, 1998).

These characteristics also speak to the idea of hydraulic jacking as proposed by Iken and Truffer (1997). With hydraulic jacking, increases in basal water pressure cause ice to either: 1) float off its bed, increasing velocities through basal sliding, or 2) in the presence of an irregular bed, pockets of water can produce an extra local increase in basal water pressure, which can cause the separation pressure threshold to be exceeded. This was mainly observed by Iken and Truffer (1997) in the early melt season, as a semi-developed drainage system attempts to compensate for increased inputs. Some of the horizontal events on John Evans Glacier were attributed to the drainage of large supraglacial lakes in large-scale events (Bingham et al., 2006). Results recorded by Anderson et al. (2004) on the Bench Glacier, Alaska, showed a smaller speed-up event occurring prior to the main spring peak. This was attributed to the switch from a distributed system to a channelized system, and saw horizontal velocity increase and surface uplift associated a single smaller pre-spring event.

5.2.2 Summer regime

The Summer Regime sees varied surface horizontal velocities and vertical motion (with speed-ups and slow-downs between ~158 and ~6 m a^{-1} and vertical changes of up to 0.5 m over 1-5 days), with an overall trend towards slower velocities over the entire regime.

Anderton (1973) and Clarke (1969) measured summer velocities of 150 m a^{-1} on the Central Arm, both using theodolite stakes. Hock and Hooke (1993) describe the development of a subglacial drainage system during the 1989 melt season on Storglaciären, Sweden, using rhodamine dye injection and proposed a braided channel system that developed through multiple peaks in subglacial water volume. Each peak in water volume would serve to enlarge the drainage system by overwhelming the previous iteration, producing rhodamine response times that are more pronounced and occur sooner after injection than at other times of the year. This has been seen on both Storglaciären (Hock and Hooke, 1993) and the Haut Glacier d'Arolla (Mair et al., 2002).

An efficient channelized system effectively evacuates subglacial water, reducing basal water pressure and decreasing support for the subglacial tunnels making up the channelized system, indicated by a gradual surface elevation lowering and overall decrease in horizontal velocity. Surface velocity is affected less by meltwater inputs in the summer because subglacial water pressure tends to remain lower than ice overburden pressure through the late melt season. At the Lower Station on the Kaskawulsh Glacier, in particular, the channelized subglacial drainage system first developed in the Spring Regime is likely able to accommodate summer peak volumes in subglacial water flow through the expansion and connection of large subglacial tunnels. This can explain the long-term reduction in horizontal motion observed through the summer regime, superimposed on the short-term velocity events.

The Summer Regime at the Kaskawulsh Glacier is likely highly variable in terms of both surface velocity and surface elevation due to periods of settling interspersed with spikes in water volume and pressure that challenge the system's drainage capacity. These spikes can arise from diurnal and short-term melt events. These kinds of events are especially prominent at the Lower Station, where the highest temperature peaks were found (JD 227, 12.9ºC) along with the highest velocities (JD 189, 317.1 m yr^{-1}). Nienow et al. (1998) identified many of these channelized characteristics later on in the melt season on the Haut Glacier d'Arolla, which coincides here with the Summer Regime. Mair et al. (2002) confirmed on the Haut Glacier d'Arolla that later in the summer season, high water volumes due to surface melt and high air temperatures result in shorter periods (4-5 days) of elevated velocity

5.2.3 Fall regime

The Fall Regime sees a decrease in horizontal velocity along with a lowering of surface elevation. This suggests a decrease in basal water pressure as temperatures drop below 0ºC (JD 265 on the South Arm, JD 266 at the Lower Station and JD 262 at the Middle Station, all for Fall 2010), and surface melting begins to slow (JD 229 on the South Arm and JD 208 at the Upper Station) (Figure 4.9). Throughout the Fall Regime, there is little variation in velocity and a consistent downward trend in surface position at the Lower and Upper stations. Vertical motion can arise from both regular downslope motion of the glacier and changes in subglacial hydrology. To assess which of the causes was dominant in the Fall Regime, the change in vertical elevation due to downslope motion was determined by fitting an annual trend line to a plot of vertical elevation and comparing with a trendline specifically for the Fall Regime. In the cases of the Lower and Upper stations, it is apparent that the observed vertical elevation changes occurred due to downslope motion at these locations. Meanwhile, the Middle Station shows a gradual increase in relative surface elevation during this period, which likely indicates a slight uphill area that forces a gain surface elevation.

Previous measurements made in the fall (e.g. Iken and Truffer, 1997) have indicated that basal water pressures are typically low, because there is insufficient meltwater input to pressurize the large subglacial channels that formed during the summer. If the subglacial channels are not full of water, then the pressures within them can become essentially atmospheric and the large ice overburden pressures caused by thick overlying ice (up to 778 m thick on the Central Arm at the confluence with North Arm; Dewart, 1969; Clarke, 1969) can cause settling of the glacier onto its bed and a collapse of the subglacial tunnel system. Motion is typically dominated by regelation and ice deformation at this time, with little influence from basal sliding (Paterson, 1994). When effective pressure is sufficiently elevated, there is also increased creep closure of the drainage system as the large channels pirate the discharge of smaller channels, reducing the amount of water stored in the lower ablation area (Schoof, 2010). Iken and Truffer (1997) linked the partial obstruction of the former subglacial channelized system of Findelengletscher to the development of areas where subglacial water accumulates and is stored.

5.2.4 Winter regime

The Winter Regime sees speed-up events that are comprised of periods of elevated horizontal velocity and elevated surface position. These winter speed-up events are identified in Figure 4.2 with the following prominent features:

- initiation of the event in the upper ablation area;
- progression of the event down-glacier over the course of hours to days;
- uplift of ice that coincides with the horizontal velocity events, followed by subsidence in surface elevation.

These events are initiated at the Upper Station and progress down-glacier over periods of 1-7 days with propagation speeds from 2138 m day^{-1} to 16,380 m day^{-1}. These values are comparable to other studies such as on the Variegated Glacier, Alaska, where down-glacier propagation speeds of ~9,600 m day^{-1} were observed (Kamb et al., 1985), and on Findelengletscher with speeds of 4320 m day^{-1} (Willis, 1995). Temperatures throughout the Winter Regime, while variable, remain below freezing and the snow sensor measurements consistently point towards accumulation or surface stability. This implies that no new meltwater is being introduced to the subglacial drainage system at this time (i.e., no external forcing), meaning that any changes in basal water pressure must be related to changes in basal water storage and the nature of the subglacial drainage system.

The features of the winter high velocity events observed on the Kaskawulsh Glacier are shared by mini-surges identified on the Variegated Glacier, Alaska (Kamb et al., 1985) and by the winter obstruction of subglacial channels on Findelengletscher, Switzerland (Iken and Truffer, 1997). Kamb et al. (1985) saw the long-term build-up of mass in the accumulation area of Variegated Glacier, commonly associated with the quiescent phase of surge-type glaciers. This increased long-term ice overburden pressure, which acted as a mechanism for the destruction of the subglacial drainage system, thereby causing basal water pressure to approach separation pressure. This leads to the pressurization of stored subglacial water, which is forced down-glacier and results in increased basal sliding as a byproduct of insufficient subglacial storage space and an inability of the distributed drainage system to compensate. While the study of Kamb et al. (1995) refers to a surge-type glacier, a similar

winter build-up of mass in the accumulation area also occurs on temperate glaciers. For example, the snow depth sounder mounted at the Upper Station on the Kaskawulsh recorded 5.0 m of snow accumulated over the course of the Fall and Winter regimes, while the South Arm saw an accumulation of 2.8 m of snow. In the case of a distributed system, small changes in ice overburden pressure, like that due to snow accumulation, could theoretically create significant changes in basal water pressure. However, there are currently no known studies that have been able to determine whether this is a common, or even plausible, phenomena.

In the case of Findelengletscher, Switzerland, Iken and Truffer (1997) attributed short term speed-ups in their winter period to the blockage of subglacial drainage channels near the terminus. This causes water to accumulate up-glacier of the terminus in the relic channels from the previous Summer Regime and the formation of a distributed subglacial drainage system. As the channels close down due to ice creep, the remaining water at the glacier bed has less space to occupy, therefore causing an increase in basal water pressure. As basal water pressure approaches separation pressure, sliding takes on more of a role in ice motion (Paterson, 1994; Iken and Truffer, 1997). The magnitudes of both horizontal velocity and uplift are most prominent at the Lower Station of the Kaskawulsh during these events. This is likely because ice thickness in this area is thinner than up-glacier, meaning less overburden pressure and a greater influence of basal water pressure on effective pressure. There is also a period of vertical subsidence after each winter event, especially at the Lower Station. This would indicate a decrease in subglacial water pressure and some re-settling of the glacier onto its bed before the next event.

In the case of the Kaskawulsh Glacier, there has been some discussion of its status of a surge-type or non-surge type glacier (Foy et al., 2011; Barrand and Sharp, 2010). It would appear that the winter velocity events observed on the Kaskawulsh Glacier in 2010 and 2011 take a similar form to the mini-surges described for the Variegated Glacier. However, they may not produce a full surge because of the large velocity spring event that occurs on the Kaskawulsh, where the subglacial drainage system likely becomes fully channelized every year. The annual spring event is initiated at the terminus and progresses up-glacier over much

longer periods than the events observed through the Winter Regime (weeks instead of days). This spring event sees velocities increase by up to 200 m a^{-1} each year, far exceeding those velocity increases seen during the Winter Regime, which are at most 75 m a^{-1}. This implies that the volume of surface meltwater flowing into the subglacial drainage system each spring is either sufficient to fully restructure the winter distributed drainage system, or there is sufficient restructuring with each spring speed-up event to prevent the build-up of subglacial water pressure necessary to establish a full surge. However, the Variegated Glacier experienced four of these mini-surges, which ranged from 146 m a^{-1} to 1095 m a^{-1}, early in the summers of 1979, 1980, and 1981, while background velocities during the quiescent phase of this glacier were between 146 m a^{-1} and 365 m a^{-1} in the upper glacier and between 36.5 m a^{-1} and 73 m a^{-1} in the lower glacier. These conditions culminated in a major surge event in January 1982 with velocities between 5475 m a^{-1} and 18,250 m a^{-1} (Kamb et al., 1985). It is possible, in other words, that the Kaskawulsh is exhibiting normal quiescent behaviour of a surge-type glacier.

5.3 Conclusions

This study provides a first assessment of the seasonal variations in velocity of the Kaskawulsh Glacier from both ground and remote sensing perspectives, and provides a solid baseline for future work in this region. Speckle tracking results show that glacier-wide velocity patterns have a similar structure between years. However, the 24-day cycle of Radarsat-2 acquisitions is too long of a timescale to capture short term variations, and is a limitation when trying to understand events that occur with greater frequency. The dGPS results presented here provide a detailed picture of velocity variations on the Kaskawulsh Glacier over a complete two year period. The annual Spring speed-up event occurs around the same time every year, coinciding with the time when air temperatures rise and remain above freezing and meltwater production begins. There is a distinct progression from peak velocities caused by high melt water volumes and high basal water pressure during the Summer Regime to low velocities and low basal water pressure during the Fall Regime. It is likely that the constant reorganization of the subglacial drainage system during the Winter Regime, when there is limited meltwater input, causes variations in effective pressure manifested as short-term speed up events that last for up to 10 days. Evidence for the

connection between the state of the subglacial drainage system, effective pressure and ice motion is strengthened by periods of vertical uplift that coincide with these horizontal velocity events. Periods of vertical uplift provide an indicator of increased basal water pressure, which in turn has a direct influence on basal sliding rates. Understanding the mechanisms that affect dynamic thinning will be essential when assessing future glacier changes in the St Elias Region and the regional contribution to sea level rise.

5.3.1 Future work

The dGPS network has now been in place for three consecutive years with minimal data gaps, and continues to be maintained by the Laboratory for Cryospheric Research. The speckle tracking results presented here are the beginning of a regional glacier velocity mapping project in conjunction with Parks Canada. Building upon this and other previous studies (e.g. Foy et al., 2011) could include a further exploration of the subglacial drainage system at various times of year, using techniques such as dye injection, a borehole network, and hydrological stations on both the Kaskawulsh and Slims rivers. The extension of the dGPS measurements into the future should capture longer-term variations in velocity. Velocity and ice flux measurements on the Kaskawulsh Glacier, used as a representative glacier in numerous mass balance studies (e.g. Arendt et al., 2002), could be upscaled to region-wide estimates for the St Elias region, including the amount of glacier mass available for melt. This would improve regional assessments of the volume of ice and meltwater available for sea level rise.

Figure 5.1 Velocity map produced from image pair 2010e (January 18 – February 11, 2010), one of three velocity maps determined to be most accurate based on the validation criteria described in Chapters 3 and 4.

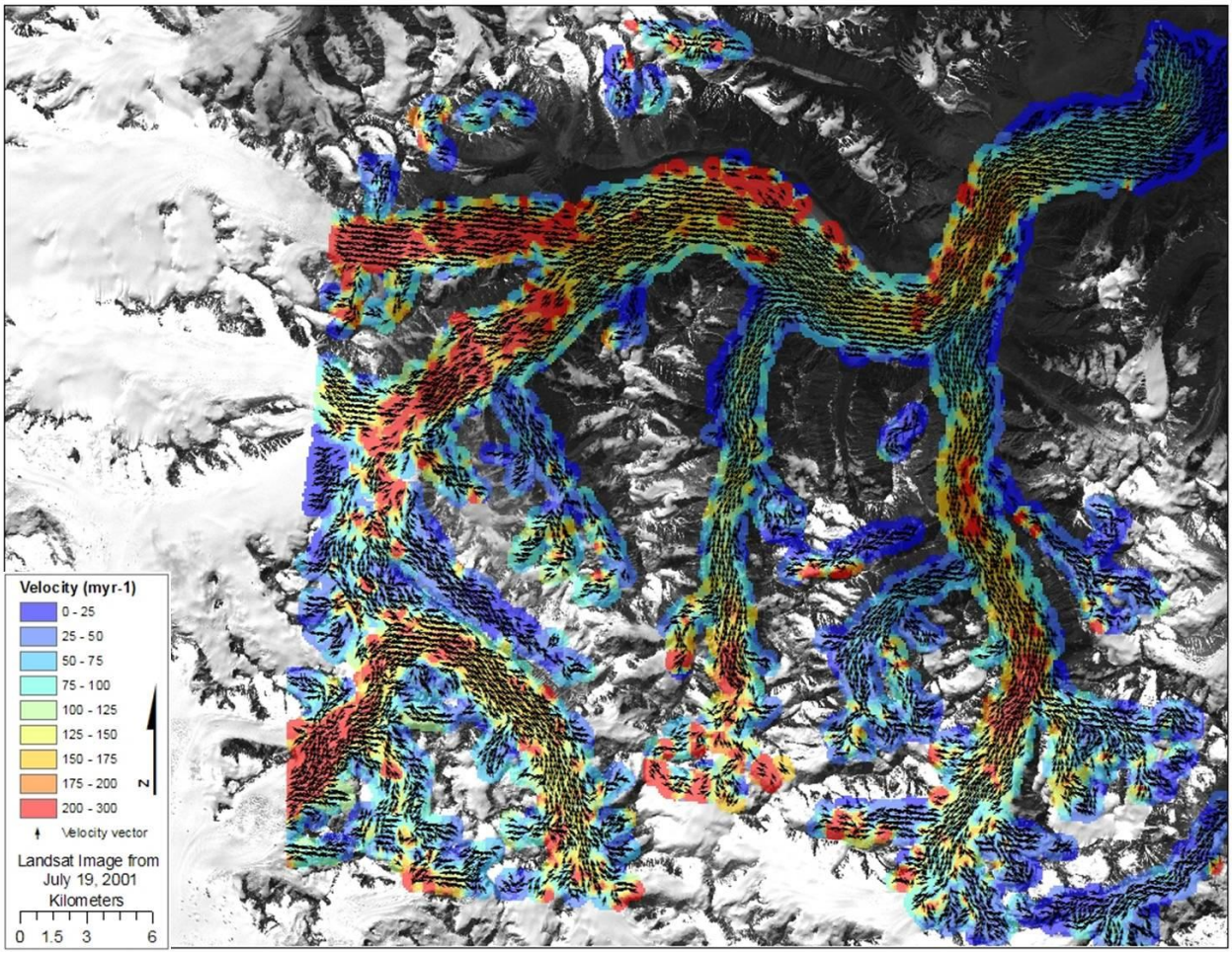

Figure 5.2 Velocity map produced from image pair 2011e (December 7 – December 31, 2010), one of three velocity maps determined to be most accurate based on the validation criteria described in Chapters 3 and 4.

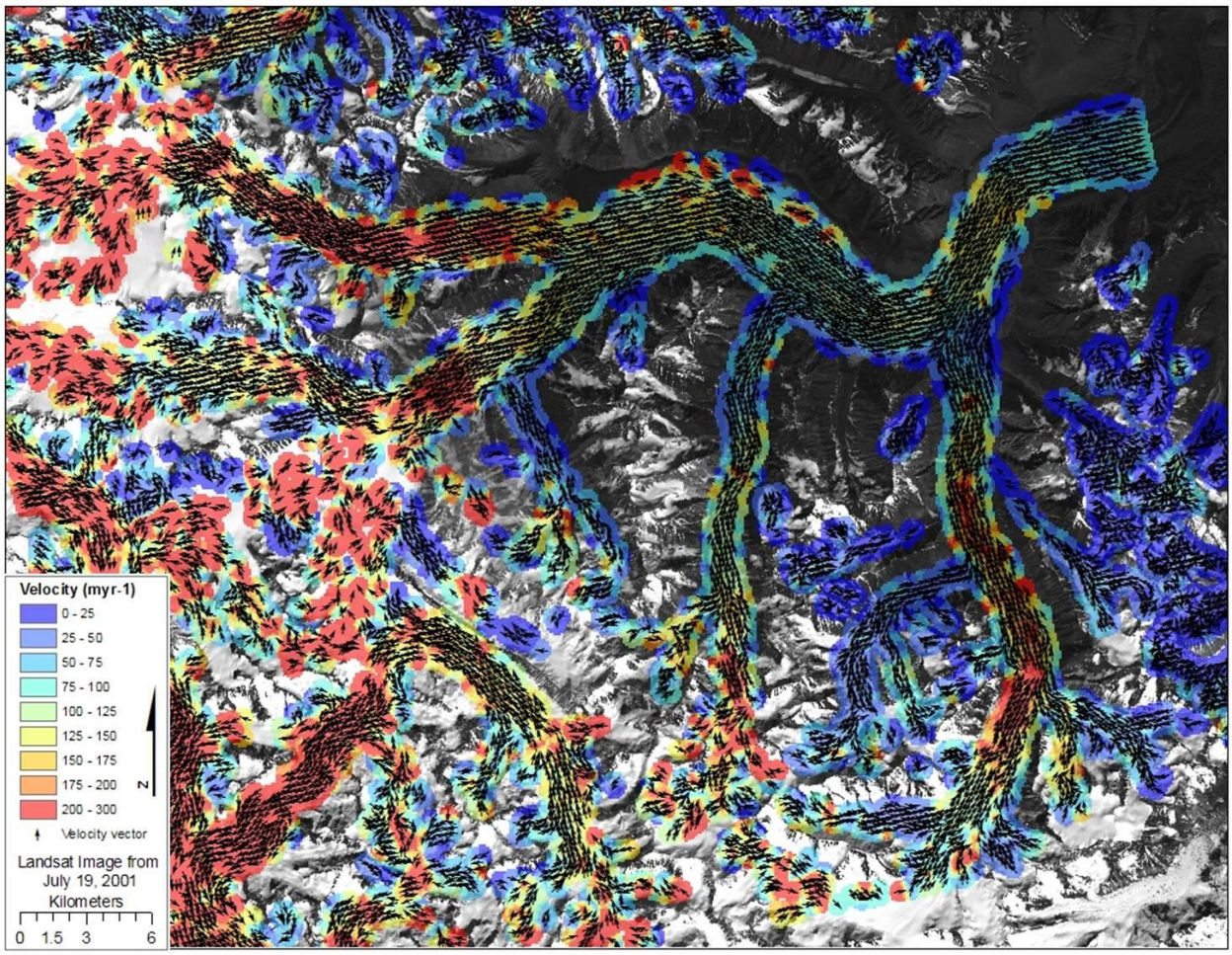

Figure 5.3 Velocity map produced from image pair 2011i (January 24 – February 17, 2011), one of three velocity maps determined to be most accurate based on the validation criteria described in Chapters 3 and 4.

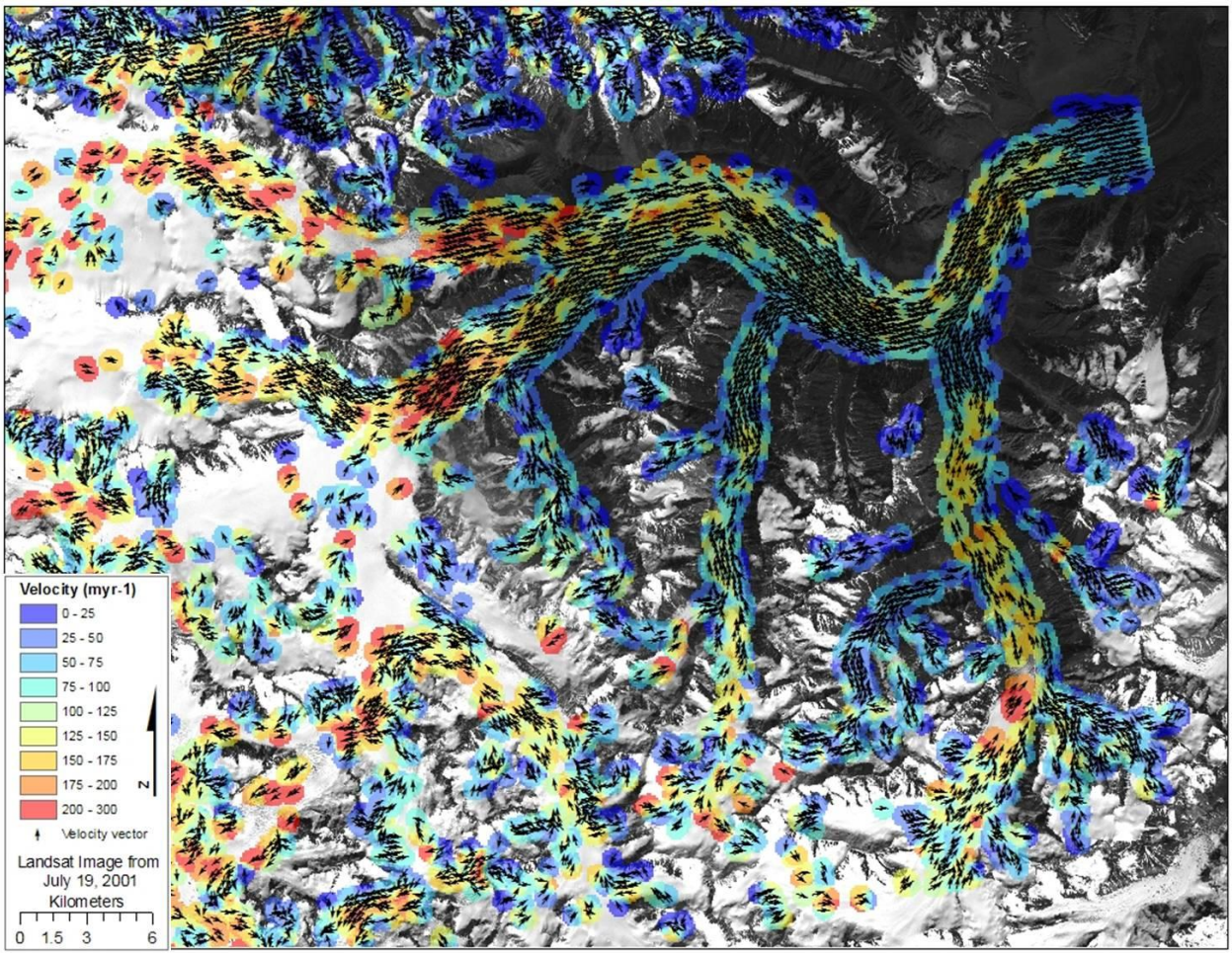

Figure 5.4 Locations of centrelines extracted from each validated velocity map: A) North Arm, B) Central Arm, C) Stairway Glacier, and D) South Arm.

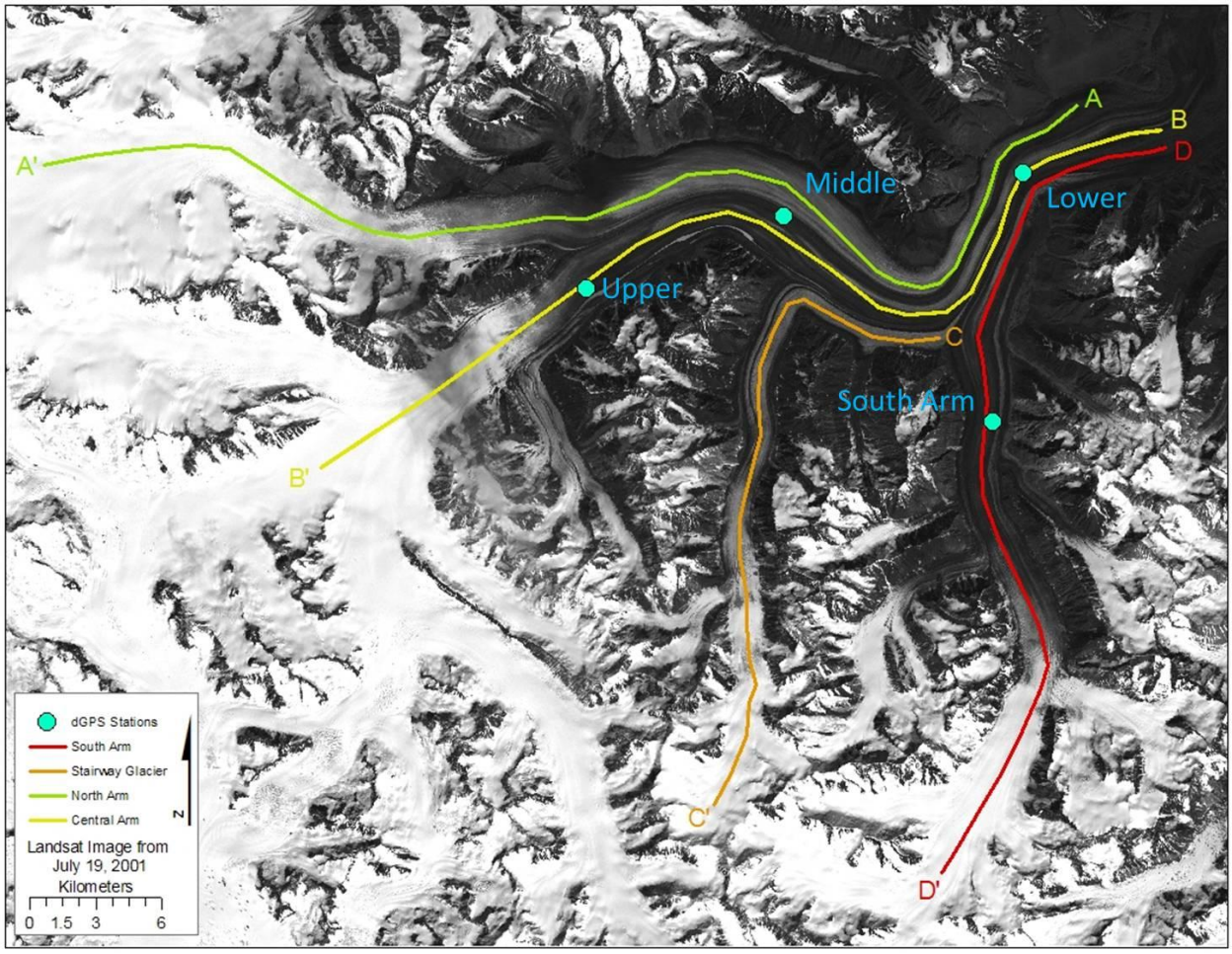

Figure 5.5 Centreline horizontal velocities extracted from corresponding image pairs (2010e. 2011e, and 2011i), originating at the terminus (e.g. A) and proceeding up-glacier into the accumulation area of each flow unit (e.g. A'). All vertical axes are in m a^{-1}. These lines were extracted at 10 m intervals for standardization, based on the IDW interpolations shown in Figures 5.1 to 5.3. Grey dotted lines refer to the position of dGPS stations, accompanied by the velocity value at the station for that time period.

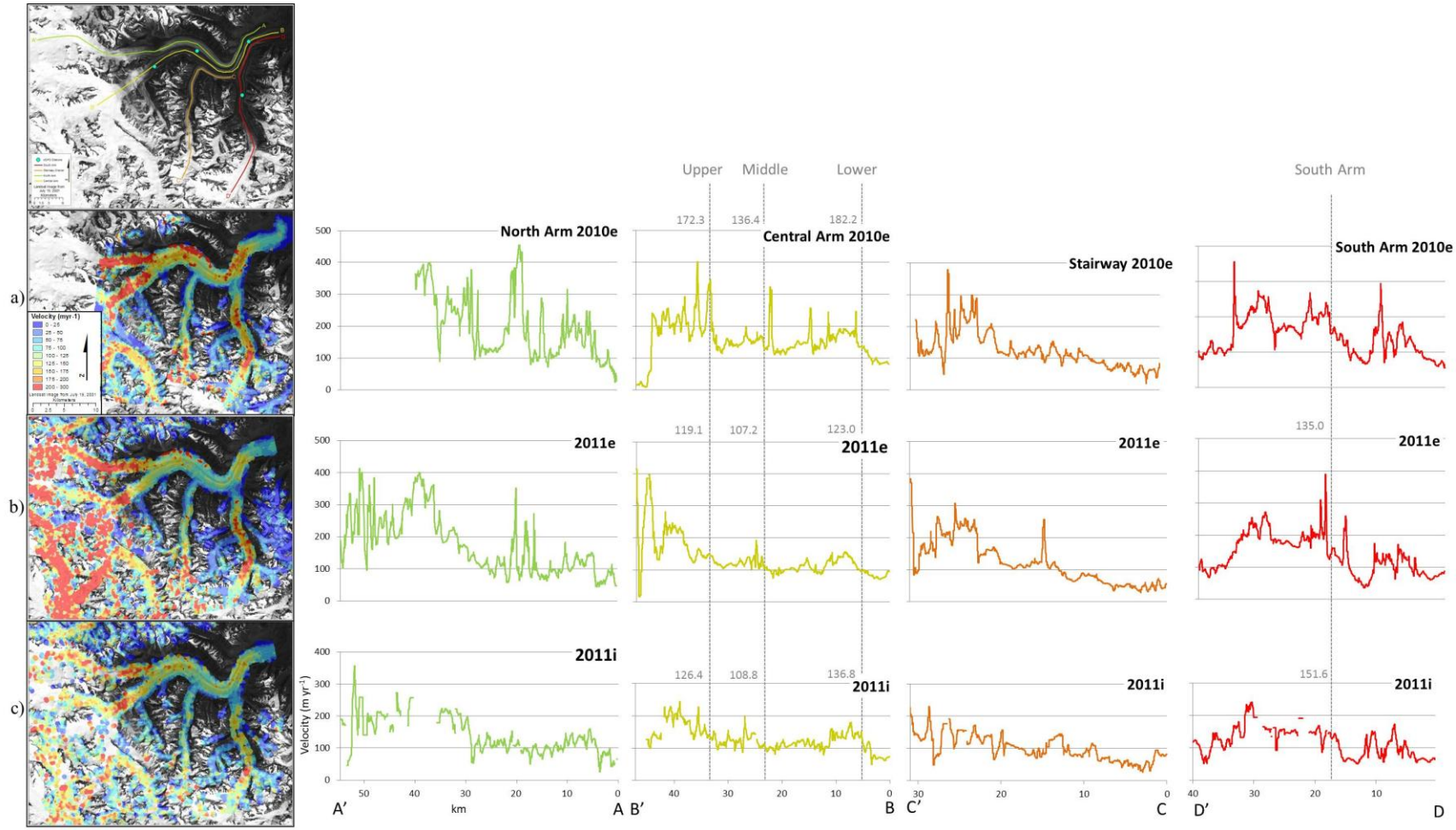

References

Alley, R.B., Dupont, T.K., Parizek, B.R., Anadakrishnan, S. (2005) Access of surface meltwater to beds of sub-freezing glaciers: preliminary insights. Annals of Glaciology. 40(1), 8-14.

Anderson, R.S., Anderson, S.P., MacGregor, K.R., Waddington, E.D., O'Neel, S., Riihimaki, C.A., and Loso, M.G. (2004) Strong feedbacks between hydrology and sliding of a small alpine glacier. Journal of Geophysical Research, 109, F03005, doi: 10.1029/2004JF000120.

Anderton, P. (1973) Structural glaciology of a glacier confluence, Kaskawulsh Glacier, Yukon Territory, Canada. Institute of Polar Studies Report No. 26, Research Foundation and the Institute of Polar Studies, The Ohio State University, 109 pp.

Arendt, A., Echelmeyer, K.A., Harrison, W.D., Lingle, C.S., and Valentine, V.B. (2002) Rapid wastage of Alaska glaciers and their contribution to rising sea level. Science, 297 (5580), 382-387.

Arendt, A., Echelmeyer, K., Harrison, W., Lingle, C., Zirnheld, S., Valentine, V., Ritchie, B., and Druckenmiller, M. (2006) Updated estimates of glacier volume changes in the western Chugach Mountains, Alaska, and a comparison of regional extrapolation methods. Journal of Geophysical Research, 111, F03019, doi:10.1029/2005JF00436.

Barrand, N. and Sharp, M. (2010) Sustained rapid shrinkage of Yukon glaciers since the 1957-1958 International Geophysical Year. Geophysical Research Letters, 37, 1-5, doi:10.1029/2009GL042030.

Bartholomew, I., P. Nienow, D. Mair, A. Hubbard, M.A. King and A. Sole. (2010) Seasonal evolution of subglacial drainage and acceleration in a Greenland outlet glacier. Nature Geoscience, 3(6), 408–411.

Barnett, A. (1974) Hydrological studies of the Slims River, Yukon, June-August, 1970. In V.C. Bushnell and R.H. Ragle (Eds.) Icefield Ranges Research Project Scientific Results (v.4), pp. 143-150, Montreal: Arctic Institute of North America.

Benn, D., & Evans, D. (1998) Glaciers and Glaciation (1st Edition, p. 734). London: Arnold.

Berthier, E., and Toutin, T. (2008) SPOT5-HRS digital elevation models and the monitoring of glacier elevation changes in North-West Canada and
of Environment, doi:10.1016/j.rse.2007.11.004.

Berthier, E., Schiefer, E., Clarke, G.K.C., Menounos, B., and Rémy, F. (2010) Contribution of Alaskan glaciers to sea-level rise derived from satellite imagery. Nature Geoscience, online, 92-95, doi: 10.1038/NGEO737.

Bingham, R., Nienow, P., and Sharp, M. (2003) Intra-annual and intra-seasonal flow dynamics of a High Arctic polythermal valley glacier. Annals of Glaciology, 37, 181-188.

Bingham, R. G., Nienow, P. W., Sharp, M. J., & Boon, S. (2005) Subglacial drainage processes at a High Arctic polythermal valley glacier. Journal of Glaciology, 51(172), 15-24.

Bingham, R. G., Nienow, P. W., Sharp, M. J., & Copland, L. (2006) Hydrology and dynamics of a polythermal (mostly cold) High Arctic glacier. Earth Surface Processes and Landforms, 31(12), 1463-1479.

Boon, S., Sharp, M.J., Nienow, P. (2003) Impact of an extreme melt event on the runoff and hydrology of a High Arctic Glacier. Hydrological Processes, (17):1051-1072.

Borns, H.W. and Goldthwait, R.P. (1966) Late-pleistocene fluctuations of Kaskawulsh Glacier, SW Yukon Territory, Canada. American Journal of Science, 264, 600-619.

Bostock, H.S. (1969) Kluane Lake: Its drainage and allied problems. In V.C. Bushnell and R.H. Ragle (Eds.) Icefield Ranges Research Project Scientific Results (v.1), pp. 149-160, Montreal: Arctic Institute of North America.

Boulton, G.S., Dobbie, K.E., and Zarsepin, S. (2001) Sediment deformation beneath glaciers and its coupling to the subglacial hydraulic system. Quaternary International, 86, 3-28.

Brahney, J., Clague, J.J., Menounos, B., Edwards, T.W.D. (2008) Timing and cause of water level fluctuations in Kluane Lake, Yukon Territory, over the past 5000 years. Quaternary Research, 70, 213-227.

Brecher, H.H. (1969) Surface Velocity measurements on the Kaskawulsh Glacier. In V.C. Bushnell & R.H. Ragle (Eds.), Icefield ranges research project; scientific results (v. 1) (pp. 127-143). Montreal: Arctic Institute of North America.

Bryan, M.L. (1972) Variations in quality and quantity of Slims river water, Yukon Territory. Canadian Journal of Earth Sciences, 9, 1469- 1478.

Chen, J., Wilson, C., Blankenship, D., and Tapley, B. (2009) Accelerated Antarctic ice loss from satellite gravity measurements. Nature Geoscience, 2, 859-862.

Clague, J.J., Luckman, B.H., Van Dorp, R.D., Gilbert, R., Froese, D., Jensen, B.J.L., and Reyes, A.V. (2006) Rapid changes in the level of Kluane Lake in Yukon Territory over the last millennium. Quaternary Research, 66, 342-355.

Clarke, G.K.C. (1969) Geophysical measurements on the Kaskawulsh and Hubbard Glaciers. In V.C. Bushnell & R.H. Ragle (Eds.), Icefield ranges research project; scientific results (v. 1) (pp. 89-106). Montreal: Arctic Institute of North America.

Clarke, G.K.C. (2005) Subglacial processes. Annual Review of Earth and Planetary Sciences, 33, 247-276. doi:10.1146/annurev.earth.33.092203.122621

Copland, L., and Sharp, M. (2001). Mapping thermal and hydrological conditions beneath a polythermal glacier with radio-echo sounding. Journal of Glaciology, 47(157), 232-242.

Copland, L., Sharp, M. and Nienow, P. (2003a) Links between short-term velocity variations and the subglacial hydrology of a predominantly cold polythermal glacier. Journal of Glaciology, 49(166), 337-348.

Copland, L., Sharp, M. and Dowdeswell, J. (2003b) The distribution and flow characteristics of surge-type glaciers in the Canadian High Arctic. Annals of Glaciology, 36, 73-81.

Copland, L., Sharp, M., Nienow, P. and Bingham, R. (2003c) The distribution of basal motion beneath a High Arctic polythermal glacier. Journal of Glaciology, 49(166), 407-414.

Copland, L., Pope, S., Bishop, M. P., Shroder, J. F., Clendon, P., and Bush, A. (2009) Glacier velocities across the central Karakoram. Annals of Glaciology, 50(1), 1-9.

Craymer, M.R. (1998) Integration of local surveys into the Canadian Spatial Reference System. Presented at the Public Works and Government Services Canada (PWGSC) Survey Contracting and CACS Seminar, Edmonton, Alberta, pp. 1-6.

Crookshanks, S., and Gilbert, R. (2008) Continuous, diurnally fluctuating turbidity currents in Kluane Lake, Yukon Territory. Canadian Journal of Earth Sciences, 45, 1123-1138, doi:10.1029/2009GL039035.

Denton, G.H. and Stuiver, M. (1969) Neoglacial chronology, northeastern St. Elias Mountains, Canada. In V.C. Bushnell & R.H. Ragle (Eds.), Icefield ranges research project; scientific results (v. 1) (pp. 109-125). Montreal: Arctic Institute of North America.

Dewart, G. (1969) Seismic investigation of ice properties and bedrock topography at the confluence of the north and central arms of the Kaskawulsh Glacier. In V.C. Bushnell & R.H. Ragle (Eds.), Icefield ranges research project; scientific results (v. 2) (pp. 77-102) Montreal: Arctic Institute of North America.

Dyurgerov, M., and McCabe, G.J. (2006) Associations between accelerated glacier mass wastage and increased summer temperature in coastal regions. Arctic, Antarctic, and Alpine Research, 38 (2), 190-197.

Dyurgerov, M., and M.F. Meier. (2005) Glaciers and the Changing Earth System: A 2004 Snapshot. Occasional Paper 58, Institute of Arctic and Alpine Research, University of Colorado, Boulder, CO, 118 pp.

European Space Agency (ESA) (2012) Section 5.2 RADAR and SAR glossary. In: The Advanced Synthetic Aperture Radar (ASAR) Product Handbook: www.envisat.esa.int/handbooks/asar/

Fahnestock, R.K. (1969) Morphology of the Slims River. In V.C. Bushnell & R.H. Ragle (Eds.), Icefield ranges research project; scientific results (v. 1) (pp. 161-172) Montreal: Arctic Institute of North America.

Fleming, S. (2005) Comparative analysis of glacial and nival streamflow regimes with implications for lotic habitat quantity and fish species richness. River Research and Applications, 21, 363-379.

Fountain, A.G. and Walder, J.S. (1998) Water flow through temperate glaciers. Reviews of Geophysics, 36, 299-328.

Foy, N., Copland, L., Zdanowicz, C., Demuth, M. and Hopkinson, C. (2011) Recent volume and area changes of Kaskawulsh Glacier, Yukon, Canada. Journal of Glaciology, 57(203), 1-11.

Giles, A.B., Massom, R.A., and Warner, R.C. (2009) A method for sub-pixel scale feature-tracking using Radarsat images applied to the Mertz Glacier Tongue, East Antarctica. Remote Sensing of Environment, 113, 1691-1699.

Gray, A.L., Mattar, K., and Sofko, G. (2000) Influence of Ionospheric Electron Density Fluctuations on Satellite Radar Interferometry. Geophysical Research Letters, 27 (10), 1451-1454.

Gray, L. (2011) Using multiple RADARSAT InSAR pairs to estimate a full three-dimensional solution for glacial ice movement. Geophysical Research Letters, 38, L05502.

Harbor, J., Sharp, M, Copland, L., Hubbard, B., Nienow, P., and Mair, D. (1997) Influence of subglacial drainage conditions on the velocity distribution within a glacier cross section. Geology, 25(8), 739-742.

Harper, J., Humphrey, N., and Pfeffer, W. (1998) Three-dimensional deformation measured in an Alaskan Glacier. Science, 281, 1340. DOI: 10.1126/science.281.5381.1340

Hock, R. and Hooke, R. (1993) Evolution of the internal drainage system in the lower part of the ablation area of Storglaciaren, Sweden. GSA Bull., 105, 537-546.

Howat, I.M., Joughin, I., Scambos, T.A. (2007) Rapid changes in ice discharge from Greenland outlet glaciers. Science, 325(5818), 1559-1561.

Howat, I., Joughin, I., Fahnestock, M., Smith, B. E., & Scambos, T. A. (2008) Synchronous retreat and acceleration of southeast Greenland outlet glaciers 2000–06: ice dynamics and coupling to climate. Journal of Glaciology, 54(187), 646-660.

Hubbard, B.P., Hubbard, A., Mader, H., Tison, J-L., Grust, K., and Nienow, P. (1995) Borehole water-level variations and the structure of the subglacial hydrological system of Haut Glacier d'Arolla, Valais, Switzerland. Journal of Glaciology, 41(139), 572-583.

Iken, A, Flotron, A., and Haeberli, W. (1983) The uplift of Unteraargletscher at the beginning of the melt season – a consequence of water storage at the bed? Journal of Glaciology, 29(101), 28-47.

Iken, A., and Truffer, M. (1997) The relationship between subglacial water pressure and velocity of Findelengletscher, Switzerland, during its advance and retreat. Journal of Glaciology, 13 (144), 328-338.

James, M. (2010) Historic change in permafrost distribution to Northern British Columbia and Southern Yukon Territory, Canada. Master's thesis submitted to the University of Ottawa, Canada, 223pp.

Joughin, I. (2002) Ice-sheet velocity mapping: a combined interferometric and speckle-tracking approach. Annals of Glaciology, 34(1), 195-201.

Joughin, I., Das., S., King, M., Smith, B., Howat, I., and Moon, T. (2008) Seasonal speedup along the western flank of the Greenland Ice Sheet. Science, 320(5877), 781-783.

Kääb, A. (2005) Remote sensing of glacier- and permafrost-related hazards in high mountains: an overview. Natural Hazards and Earth System Sciences, 5, 527-554.

Kamb, B., Raymond, C.F., Harrison, W., Engelhardt, H., Echelmeyer, K., Humphrey, N., Brugman, M., and Pfeffer, T. (1985) Glacier surge mechanism: 1982-1983 surge of Variegated Glacier, Alaska. Science, 227(4686), 469-479.

Kaser, G., Cogley, J.G., Dyurgerov, M.B., Meier, M.F., and Ohmura, A. (2006) Mass balance of glaciers and ice caps: Consensus estimates for 1961-2004. Geophysical Research Letters, 33, L19501, doi: 10.1029/2006GL027511.

Kerr, R.A. (2009) Both of the world's ice sheets may be shrinking faster and faster. Science, 326, 217.

King, M., Edward., S., and Clarke, P. (2002) Precise Point Positioning: Breaking the Monopoly of Relative GPS Processing. GPS Techniques, Engineering Surveying Showcase.

King, M. (2004) Instruments and methods: rigorous GPS data-processing strategies for glaciological applications. Journal of Glaciology, 50(171), 601-607.

Kwok, R., and Rothrock, D. (2009) Decline in Arctic sea ice thickness from submarine and ICESat records: 1958-2008. Geophysical Research Letters, 36, 1-5, doi:10.1029/2009GL039035.

Lappegard, G., and Kohler, J. (2006) Determination of basal hydraulic systems based on subglacial high-pressure pump experiments. Annals of Glaciology, 40(1), 37-42.

Larsen, C.F., Motyka, R.J., Arendt, A.A., Echelmeyer, K.A., and Geissler, P.E. (2007) Glacier changes in southeast Alaska and northwest British Columbia and contribution to sea level rise. Journal of Geophysical Research, 112, doi:10:1029/2006JF00586.

Lemke, P., J. Ren, R.B. Alley, I. Allison, J. Carrasco, G. Flato, Y. Fujii, G. Kaser, P. Mote, R.H. Thomas and T. Zhang (2007) Observations: Changes in Snow, Ice and Frozen Ground. In: Climate Change 2007: The Physical Science Basis. Contribution of Working Group I to the Fourth Assessment Report of the Intergovernmental Panel on Climate Change [Solomon, S., D. Qin, M. Manning, Z. Chen, M. Marquis, K.B. Averyt, M. Tignor and H.L. Miller (eds.)]. Cambridge University Press, Cambridge, United Kingdom and New York, NY, USA.

Lliboutry, L. (1959) Une théorie du frottement du glacier sur son lit. Annals Geophysiques, 15(2), 250–265.

Luthcke, S., Zwally, H., Abdalati, D., Rowlands, D., Ray, R., Nerem, R., Lemoine, F., McCarthy, J., and Chinn, D. (2006) Recent Greenland ice mass loss by drainage system from satellite gravity observations. Science, 314, 1286-1289.

Macpherson, D.S., and Krouse, H.R. (1969) O18/O16 Ratios in Snow and Ice of the Hubbard and Kaskawulsh Glaciers. In V.C. Bushnell and R.H.Ragle (Eds.) Icefield Ranges Research Project Scientific Results (v.1), 63-73, Montreal: Arctic Institute of North America.

Mair, D., Nienow, P., Sharp, M., Wohlleben, T., and Willis, I. (2002) Influence of subglacial drainage system evolution on glacier surface motion: Haut Glacier d'Arolla, Switzerland. Journal of Geophysical Research, 107(B8), 2175, doi: 10.1029/2001JB000514.

Mair, D., Willis, I., Fischer, U.H., Hubbard, B., Nienow, P., and Hubbard, A. (2003) Hydrological controls on patterns of surface, internal and basal motion during three "spring events": Haut Glacier d'Arolla, Switzerland. Journal of Glaciology, 49, 555-567.

Marcus, M.G. (1974) Investigations in Alpine Climatology: The St Elias Mountains, 1963-1971. In V.C. Bushnell and R.H.Ragle (Eds.) Icefield Ranges Research Project Scientific Results (v.4), 13-26, Montreal: Arctic Institute of North America.

Meier, M.F., and Dyurgerov, M.B. (2002) How Alaska affects the world. Science, 297 (5580), 350-351.

Meier, M.F., Dyurgerov, M.B., Rick, U.K., O'Neel, S., Pfeffer, T.W., Anderson, R.S., Nderson, S.P., Glazovsky, A.F. (2007) Glaciers dominate eustatic sea-level rise in the 21st century. Science, 317, 1064-1067.

Molnia, B.F. (2007) Late nineteenth to early twenty-first century behaviour of Alaskan glaciers as indicators of changing regional climate, Global and Planetary Change, 56, 23-56.

Mote, T. (2007) Greenland surface melt trends 1973–2007: Evidence of a large increase in 2007. Geophysical Research Letters, 34, 1-5.

Murray, T., Strozzi, T, Luckman, A., Jiskoot, H., and Christakos, P. (2003) Is there a single surge mechanism? Contrasts in dynamics between glacier surges in Svalbard and other regions. Journal of Geophysical Research B: Solid Earth, 108 (5), 3-15.

Natural Resources Canada, Geodetic Survey Division. (2004) On-Line Precise Point Positioning Project-How To Use Document.
http://www.geod.nrcan.gc.ca/userguide/pdf/howtouse.pdf

Natural Resources Canada. (2007) CSRS-PPP Accuracy.
http://www.geod.nrcan.gc.ca/products- produits/ppp_acc_e.php

Nienow, P., Sharp, M., and Willis, I. (1998) Seasonal changes in the morphology of the subglacial drainage system, Haut Glacier D'Arolla, Switzerland. Earth Surface Processes and Landforms, 23, 825-843.

Orgiazzi, D., Tavella, P., and Lahaye, F. (2005) Experimental Assessment of the Time Transfer Capability of Precise Point Positioning. Natural Resources Canada, online: http://www.geod.nrcan.gc.ca/publications/papers/abs36_e.php

Paterson, W. (1994) The Physics of Glaciers (3rd edition) 480pp. Pergamon/Elsevier Science Ltd: Tarrytown, New York.

Pope, S., Copland, L., and Mueller, D. (2012) Loss of multiyear landfast sea ice from Yelverton Bay, Ellesmere Island, Nunavut, Canada. Arctic, Antarctic and Alpine Research, 44 (2), 210-221.

Pritchard, H.D., Arthern, R., Vaughan, D., and Edwards, L. (2009) Extensive dynamic thinning on the margins of the Greenland and Antarctic ice sheets. Nature, 461, 971-975 doi:10.1038/nature08471

Quincey, D.J., Copland, L., Mayer, C., Bishop, M., Lackman, and Belo, M. (2009) Ice Velocity and climate variations for Baltoro Glacier, Pakistan. Journal of Glaciology, 55(194), 1061-1671.

Reyes, A.V., Luckman, B.H., Smith, D.J., Clague, J.J., and Van Dorp, R.D. (2006) Tree-ring dates for the maximum Little Ice Age advance of Kaskawulsh Glacier, St. Elias Mountains, Canada. Arctic, 59 (1), 14-20.

Rignot, E., Bamber, J., Van Dan Broeke, M., Davis, C., Yonghong, L., Van De Berg, W., and Van Meijgaard, E. (2008a) Recent Antarctic ice mass loss from radar interferometry and regional climate modeling. Nature, 1, 106-110 doi:10.1038/ngeo102.

Rignot, E., Box, J.E., Burgess, E., and Hanna, E. (2008b) Mass balance of the Greenland ice sheet from 1958 to 2007. Geophysical Research Letters, 35, doi:10.1029/2008GL035417

Rignot, E., and Kanagaratnam, P. (2006) Changes in the velocity structure of the Greenland Ice Sheet. Science, 311(5763), 986-990.

Sapiano, J.J., Harrison, W.D., and Echelmeyer.K.A. (1998) Elevation, volume and terminus changes of nine glaciers in North America. Journal of Glaciology, 44(146), 119-135.

Sauber, J., Molnia, B., Carabajal, C., Luthcke, S., and Muskett, R. (2005) Ice elevations and surface change on the Malaspina Glacier, Alaska. Geophysical Research Letters, 32, doi:10.1029/2005GL023943.

Scambos, T.A., M.J. Dutkiewicz, J.C. Wilson and R.A. Bindschadler. (1992) Application of image cross- correlation to the measurement of glacier velocity using satellite image data. Remote Sensing of Environment, 42(3), 177–186.

Schoof, C. (2010) Ice-sheet acceleration driven by melt supply variability. Nature, 468, 803-806, doi:10.1038/nature09618.

Short, N. H., and Gray, A. L. (2004) Potential for RADARSAT-2 interferometry: glacier monitoring using speckle tracking. Canadian Journal for Remote Sensing, 30(3), 504-509.

Short, N. H., and Gray, A. L. (2005) Glacier dynamics in the Canadian High Arctic from RADARSAT-1 speckle tracking. Canadian Journal for Remote Sensing, 31(3), 225-239.

Smith, S., Romanovsky, V., Lewkowicz, A., Burn, C., Allard, M., Clow, G., Yoshikawa, K., and Throop, J. (2010) Thermal state of permafrost in North America: a contribution to the International Polar Year. Permafrost and Periglacial Processes, 21, 117-135.

Stenborg, T. (1973) Some viewpoints on the internal drainage of glaciers. Hydrology of Glaciers, IASH Publ., 95, 117–129.

Stroeve, J., Serreze, M., Drobot S., Gearheard, S., Holland, M., Maslanik, J., Meier, W., and Scambos, T. (2008) Arctic sea ice extent plummets in 2007. EOS, 89 (2), 13-14.

Strozzi, T., Kouraev, A., Wiesmann, A., Wegmuller, U., Sharov, A., and Werner, C. (2008) Estimation of Arctic glacier motion with satellite L-band SAR data. Remote Sensing of Environment, 112, 636-645.

Sundal, A.V., Sheperd, A., Nienow, P., Hanna, E., Palmer, S., and Huybrechts, P. (2011) Melt-induced speed-up of Greenland ice sheet offset by efficient subglacial drainage. Nature, 469, 521-524, doi:10.1038/nature09740.

Thomas, R., Frederick, E., Krabill, W., Manizade, S., & Martin, C. (2006) Progressive increase in ice loss from Greenland. Geophysical Research Letters, 33(10), 2-5.

Van de Wal, R.S.W., Boot, W., Van den Broeke, M.R., Smeets, C.J., Reijmer, C.H., Donker, J.J., and Oerlemans, J. (2008) Large and rapid melt induced velocity changes in the ablation zone of the Greenland Ice Sheet. Science, 321(5885), 111–113.

VanWychen, W., Copland, L., Gray, L., Burgess, D., Danielson, B., and Sharp, M. (2012) Spatial and temporal variation of ice motion and ice flux from Devon Ice Cap, Nunavut, Canada. Journal of Glaciology, 58 (210), 657-664.

Velicogna, I. (2009) Increasing rates of ice mass loss from the Greenland and Antarctic ice sheets revealed by GRACE. Geophysical Research Letters, 36, L19503, doi: 10.1029/2009GL040222.

Weertman, J. (1954) On the sliding of glaciers. Journal of Glaciology, 3(21), 33-38.

Willis, I. (1995) Intra-annual variations in glacier motion: a review. Progress in Physical Geography, 19(1), 61-106.

Yukon Territorial Government Geomatics Department (1997)
http://www.geomaticsyukon.ca/data

Zhang, X., and Andersen, O. (2006) Surface ice flow velocity and tide retrieval of the Amery ice shelf using precise point positioning. Journal of Geodesy, 80, 171-176.

Zumberge, J. F., Heftin, M. B., Jefferson, D. C., & Watkins, M. M. (1997) Precise point positioning for the efficient and robust analysis of GPS data from large networks. Journal of Geophysical Research, 102(B3), 5005-5017.

Zwally, J., Abdalati, W., Herring, T., Larson, K., Saba, J., Steffen, K. (2002) Surface melt-induced acceleration of Greenland ice-sheet flow. Science, 297(5579), 218-222.

Zwally, J.H., Brenner, A.C., Beckley, M., Cornejo, H.G., DiMarzio, J., Giovinetto, M.B., Neumann, T.A., Robbins, J., Saba, J.L., Yi, D., and Wang, W. (2011) Greenland ice sheet mass balance: distribution of increased mass loss with climate warming; 2003–07 versus 1992–2002. Journal of Glaciology, 57 (201), 88-102.